AD-A136 296 THE EFFECTS OF CYLINDRICAL SURFACE MODIFICATIONS ON TURBULENT BOUNDARY LA..(U) LEHIGH UNIV BETHLEHEM PA DEPT OF MECHANICAL ENGINEERING AND M.. 1/2

UNCLASSIFIED J B JOHANSEN ET AL. APR 83 AFOSR-TR-83-1217 F/G 20/4 NL

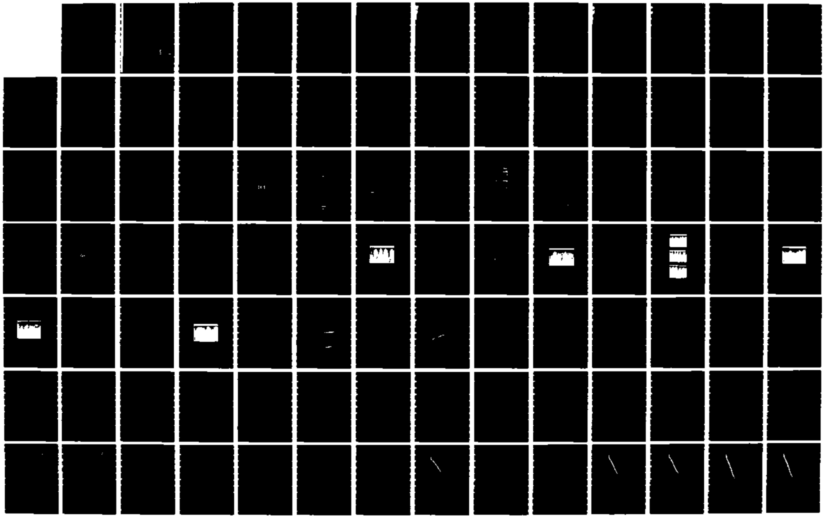

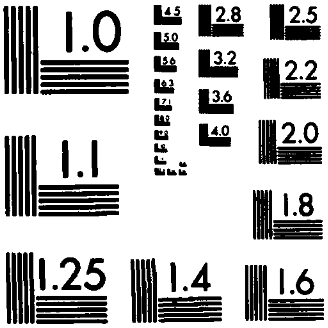
1.0
4.5
5.0
5.6
6.3
7.1
2.8
3.2
3.6
4.0
2.5
2.2
2.0
1.1
1.8
1.25
1.4
1.6

AFOSR-TR- 83-1217

②

Lehigh University

THE EFFECTS OF CYLINDRICAL SURFACE MODIFICATIONS ON TURBULENT BOUNDARY LAYERS

by

J.B. Johansen and C.R. Smith

Report FM-3

April 1983

Prepared under Financial Support of
U.S. Air Force Office of Scientific Research
Contract F49620-78-C-0071

Department of Mechanical Engineering & Mechanics
Lehigh University, Bethlehem, PA 18015

REPORT DOCUMENTATION PAGE

READ INSTRUCTIONS
BEFORE COMPLETING FORM

1. REPORT NUMBER
AFOSR-TR- 83-1217

2. GOVT ACCESSION NO.
AD-A136 996

3. RECIPIENT'S CATALOG NUMBER

4. TITLE (and Subtitle)
THE EFFECTS OF CYLINDRICAL SURFACE MODIFICATIONS ON TURBULENT BOUNDARY LAYERS

5. TYPE OF REPORT & PERIOD COVERED
INTERIM

6. PERFORMING ORG. REPORT NUMBER

7. AUTHOR(s)
J B JOHANSEN
C R SMITH

8. CONTRACT OR GRANT NUMBER(s)
F49620-78-C-0071

9. PERFORMING ORGANIZATION NAME AND ADDRESS
LEHIGH UNIVERSITY
DEPT OF MECHANICAL ENGINEERING & MECHANICS
BETHLEHEM, PA 18015

10. PROGRAM ELEMENT, PROJECT, TASK AREA & WORK UNIT NUMBERS
61102F
2307/A2

11. CONTROLLING OFFICE NAME AND ADDRESS
AIR FORCE OFFICE OF SCIENTIFIC RESEARCH/NA
BOLLING AFB, DC 20332

12. REPORT DATE
April 1983

13. NUMBER OF PAGES
142

14. MONITORING AGENCY NAME & ADDRESS (if different from Controlling Office)

15. SECURITY CLASS. (of this report)
Unclassified

15a. DECLASSIFICATION/DOWNGRADING SCHEDULE

16. DISTRIBUTION STATEMENT (of this Report)

Approved for Public Release; Distribution Unlimited.

17. DISTRIBUTION STATEMENT (of the abstract entered in Block 20, if different from Report)

18. SUPPLEMENTARY NOTES

19. KEY WORDS (Continue on reverse side if necessary and identify by block number)

FLUID MECHANICS
TURBULENCE
TURBULENT BOUNDARY LAYERS
BOUNDARY LAYER CONTROL
TURBULENCE CONTROL
SURFACE MODIFICATIONS

20. ABSTRACT (Continue on reverse side if necessary and identify by block number)

A study employing a combination of hydrogen bubble-wire flow visualization and hot-film anemometry measurements has been conducted to determine the effects of sublayer scale streamwise surface modifications on the structure and flow characteristics of turbulent boundary layers. The surface modifications were created using very fine monofilament fishing line of an approximate non-dimensional height of $h^+ = 4$. Spanwise line spacings of $60 < s^+ < 160$ were examined for a Reynolds number range $800 < RE_\theta < 1650$. The hydrogen bubble-wire studies indicate that the lines appear to act as nucleation sites for low-speed streaks, but the influence of the lines on streak stabilization rapidly diminishes for $y^+ > 10$. Streak spacing distributions and statistics were developed from the visualization data for both modified and unmodified surfaces. These results clearly indicate that the surface modifications did affect the streak spacing characteristics, with the greatest effect of the lines on mean streak spacing distributions and statistics occurring for $s^+ < 100$. However, the visualizations indicate that for $y^+ > 10$ the determined streak spacing distributions and statistics, for all modified surface line spacings, relax back to those characteristic of an unmodified surface. Mean velocity and turbulence intensity profiles determined for several of the modified surfaces indicate essential similarity with those of conventional turbulent boundary layers with variations occurring only near the modifying lines. Momentum integral techniques were used to calculate total surface drag from the measured velocity profiles, and indicate that the modifications cause a 3% to 8% increase in total surface drag in comparison to an unmodified flat plate. The degree of drag increase shows an apparent correspondence with the narrowing of the line spacing. A hypothesis correlating the increase in drag with the modification of low-speed streak structure by the surface modifications is proposed.

THE EFFECTS OF CYLINDRICAL SURFACE MODIFICATIONS ON TURBULENT BOUNDARY LAYERS

by

J.B. Johansen and C.R. Smith

Prepared under Financial Support of
U.S. Air Force Office of Scientific Research
Contract F49620-78-C-0071

Report FM -3

Department of Mechanical Engineering & Mechanics
Lehigh University
Bethlehem, PA. 18015

April 1983

ACKNOWLEDGEMENTS

We wish to acknowledge the assistance of Mr. A.W. Cerra and Mr. T. Wei with the visual studies. A special thanks to J. Bunderla, Mr. R. Towne, and Mr. F. Wehden for their fabrication of the test plates. Finally, we wish to thank Mrs. Joan Decker for her efforts in the preparation of the typed manuscript.

This work was supported by the Air Force Office of Scientific Research and performed under AFOSR Contract Number F 49620-78-C-0071. We gratefully acknowledge the continuing support of our research by AFOSR.

TABLE OF CONTENTS

Page

LIST OF TABLES

LIST OF FIGURES

NOMENCLATURE

AL	hot-film probe located above a line
BL	hot-film probe located between two lines
C_f	skin friction coefficient, $\equiv \frac{U_\tau^2}{1/2\ U^2}$
DM	hot-film probe located downstream of modifications
FP	hot-film probe located above the flat plate
F_λ	flatness moment of probability density distribution of λ
f	streak bursting frequency
f_b	hydrogen bubble time-line generation frequency
H	boundary layer shape factor, $\equiv \frac{\delta_d}{\Theta}$
h^+	nondimensional height of modifications, $\equiv \frac{hU_\tau}{\nu}$
i	data sample index
k	height of flow trip roughness elements
n	total number of data samples
$P(\lambda)$	probability density function of λ
Re_k	Reynolds number based on flow trip roughness element height, $\equiv \frac{kU}{\nu}$
Re_y	Reynolds number based on normal coordinate, $\equiv \frac{yU}{\nu}$
Re_Θ	Reynolds number based on momentum thickness, $\equiv \frac{\Theta U}{\nu}$
S_λ	skewness moment of probability density distribution of λ
s^+	nondimensional spanwise spacing of modifications, $\equiv \frac{sU_\tau}{\nu}$
T_B	streak bursting time period

t^+	nondimensional time, $\equiv \frac{tU_\tau^2}{\nu}$
U	free stream velocity outside boundary layer
u	time-averaged, local streamwise velocity
U_k	velocity in the height of flow trip roughness elements
UM	hot-film probe located upstream of modifications
U_1	maximum hot-film calibration velocity
U_2	hot-film calibration velocity, $\equiv \frac{1}{2}U_1$
$\sqrt{\overline{U'^2}}$	root mean square of streamwise velocity fluctuations
U_τ	friction or shear velocity
U^+	nondimensional streamwise velocity, $\equiv \frac{u}{U_\tau}$
x^+	nondimensional streamwise coordinate, $\equiv \frac{xU_\tau}{\nu}$
y^+	nondimensional coordinate normal to plate, $\equiv \frac{yU_\tau}{\nu}$
y^+_{wire}	nondimensional distance of bubble-wire above plate, $\equiv \frac{y_{wire}\ U_\tau}{\nu}$
z^+	nondimensional spanwise coordinate, $\equiv \frac{zU_\tau}{\nu}$

Greek

$\alpha(\lambda)$	lognormal cumulative probability of λ
δ	boundary layer thickness (where $u = 0.99\ U$)
δ_d	displacement thickness

Θ	momentum thickness
λ	spanwise spacing between low-speed streaks
λ_o	mean value λ for lognormal probability density distribution
λ_{mp}	most probable value for probability density distribution
$\overline{\lambda}$	mean value of λ
λ^+	nondimensional streak spacing, $\equiv \frac{\lambda U_\tau}{\nu}$
ν	kinematic viscosity
$\frac{\nu}{U_\tau}$	viscous length
ω	vorticity
σ_λ	standard deviation of probability density distribution of λ
τ_o	wall shear stress
ψ_λ	coefficient of variation of probability density distribution of λ
ψ_o	standard deviation of lognormal probability distribution ($\ln \lambda$)

ABSTRACT

A study employing a combination of hydrogen bubble-wire flow visualization and hot-film anemometry measurements has been conducted to determine the effects of sublayer scale streamwise surface modifications on the structure and flow characteristics of turbulent boundary layers. The surface modifications were created using very fine monofilament fishing line of an approximate non-dimensional height of $h^{+} = 4$. Spanwise line spacings of $60 < s^{+} < 160$ were examined for a Reynolds number range $800 < Re_{\theta} < 1650$. Re sub theta

The hydrogen bubble-wire studies indicate that the lines appear to act as nucleation sites for low-speed streaks, but the influence of the lines on streak stabilization rapidly diminishes for $y^{+} > 10$. Streak spacing distributions and statistics were developed from the visualization data for both modified and unmodified surfaces. These results clearly indicate that the surface modifications did affect the streak spacing characteristics, with the greatest effect of the lines on mean streak spacing distributions and statistics occurring for $s^{+} < 100$. However, the visualizations indicate that for $y^{+} > 10$ the determined streak spacing distributions and statistics, for all modified surface line spacings, relax back to those characteristic of an unmodified surface.

Mean velocity and turbulence intensity profiles determined for several of the modified surfaces indicate essential similarity with those of conventional turbulent boundary layers with variations occurring only near the modifying lines. Momentum integral techniques were used to calculate total surface drag from the measured velocity profiles, and indicate that the modifications cause a 3% to 8% increase in total surface drag in comparison to an unmodified flat plate. The degree of drag increase shows an apparent

correspondence with the narrowing of the line spacing. A hypothesis correlating the increase in drag with the modification of low-speed streak structure by the surface modifications is proposed.

1 INTRODUCTION

1.1 GENERAL

Energy dissipation through the generation of turbulence is generally a primary factor limiting optimal utilization of the energy contained in a flowing fluid. Since the major portion of turbulence generation is a result of fluid-boundary interactions, investigations of turbulent boundary layers, particularly with regard to the control of turbulence, have been actively pursued for many years. In a series of particularly key studies, Klebanoff (1954) observed that a sharp peak of turbulent energy production occurs just outside the "viscous sublayer", or in that region of the turbulent boundary layer sometimes referred to as the "buffer region." He found that although the wake or outer region of the boundary layer comprises eighty percent of the boundary layer thickness, it only contributes to twenty percent of the turbulent energy production.

Since the major production of turbulent energy occurs in the inner 20% of the turbulent boundary layer, Kline et al. (1967) were prompted to conduct an intensive study, using both visual and quantitative techniques, of the near wall region ($y^+ < 40$). They determined that the viscous sublayer ($y^+ \leq 5$) is not two-dimensional and steady as some models suggest, but consists of three-dimensional unsteady motions all the way to the wall. They also observed that the major production of turbulent energy in the inner region of the boundary layer is the result of violent bursts of low-speed fluid from regions very near the wall. They hypothesized that these bursts were the result of an instability mechanism, and that they are the primary means by which turbulent kinetic energy is transported to the outer or wake region of the boundary layer.

The bursting process, as described by Kline, begins with the formation of low-speed streaks along the surface of the flat plate. Due to the presence of streamwise vorticity between the streaks, the streaks move outward from the wall as they propagate downstream, with streak oscillation beginning to take place at $y^+ \cong 10$. As the streak continues to lift outward from the surface the oscillation intensifies, and the streak is stretched and deformed until it bursts at $y^+ \leq 30$. Hence, $10 < y^+ \leq 30$ is considered to be the streak "break-up" range. Kim et al. (1971), Grass (1971), Oldaker and Tiederman (1977), Smith (1978), and others, have all observed essentially this same streak-burst process.

Another characteristic of the "streaky structure" is that the structures appear to arrange themselves in such a manner to yield a non-dimensional mean transverse streak spacing of $\overline{\lambda^+} = \lambda U_\tau/\nu = 100 \pm 20$. This characteristic spacing of the streaks has also been confirmed by Kline et al. (1967), Oldaker and Tiederman (1977), Metzler (1980), and Nakagawa and Nezu (1981), with the most detailed study being conducted by Smith and Metzler (1983).

Although there have been several studies of the "streaky structure", most explanations of the origins of the low-speed streaks, the bursting process, and why it contributes approximately 80% of the turbulent kinetic energy produced in a turbulent boundary layer, are only hypotheses. Present research efforts are directed toward both understanding and controlling the phenomenon of streaks and streak bursting. One area of investigation is the potential for controlling streak spacing and bursting by means of streamwise surface modifications. A viable drag reduction mechanism may exist if streamwise surface modifications can force streak spacing to increase, thus causing burst intensity (bursts per unit area) to decrease. This would be speculated to decrease momentum transfer, which would yield to a lower wall shear stress, and thus a reduction in drag. On the other hand, if streak spacing is forced to decrease or burst intensity should increase due to streamwise surface modifications, surface drag should increase as a result of increased momentum transfer.

1.2 STREAMWISE SURFACE MODIFICATIONS

Studies of the behavior of a turbulent boundary layer passing over streamwise roughness elements were first conducted by Liu et al. (1967). The roughness elements they examined were rectangular strips of non-dimensional thickness $k^+ = 22.3$ and streamwise length $x^+ = 6986$. Non-dimensional heights (h^+) of 11, 45, 69, and 111 were tested at non-dimensional transverse spacings of $62 \leq s^+ \leq 502$. The study employed both dye and hydrogen bubble techniques to observe the low-speed streaks and determine the bursting rates.

Liu determined that with the exception of $h^+ = 11$, the burst rate with the modifications appeared to decrease from that for an unmodified flat plate as s^+ was decreased. For each h^+, Liu was able to establish a s^+_{min} which minimized the bursting rate. Further reduction of s^+ below this minimum resulted in an increase in the burst rate. The maximum reduction of burst rate appeared to be twenty to twenty-five percent below that for the unmodified plate, which suggests that streamwise surface modifications can influence momentum exchange and turbulent energy production. In addition, the measured momentum thicknesses for the modified surfaces when compared to those for an unmodified flat plate boundary layer, indicated that the modifications could facilitate drag reductions of up to three percent ($h^+ = 45$, $s^+ = 190$ and $h^+ = 69$, $s^+ = 258$), or drag increases of up to fifteen percent ($h^+ = 111$, $s^+ = 373$).

In a similar study to that of Liu et al. (1967), Metzler (1980) conducted water channel studies using thin round brass rods, anchored to the channel bottom with their axes parallel to the streamwise flow. Based upon the viscous length, (ν/U_τ), the non-dimensional height (diameter) of the rods and their streamwise length was $h^+ = 9.5$ and $x^+ = 3600$, respectively. Studies were conducted for non-dimensional rod spacings (s^+) of 60 and 120.

Metzler observed that for $s^+ = 60$ the streak spacing was coincident with the rod spacing for $y^+ = 10$, $(\lambda^+ = 60)$ and for a distance downstream of the trailing ends of the rods of about $\Delta x^+ = 120$, $(\lambda^+ = 75)$. Note that Metzler referenced all y^+ measurements to the flat plate surface (channel bottom). However, studies at $y^+ > 10$ and downstream distances greater than $\Delta x^+ = 120$ showed the "streak structure" appeared to rapidly revert to the larger flat plate streak spacing of $\lambda^+ = 100$.

Metzler noted that for $s^+ = 120$ the streak spacing was forced to coincide with the rod spacing. This effect was more pronounced in both the streamwise and vertical directions than for the rod spacing of $s^+ = 60$. At $y^+ = 16$ above the rods $(s^+ = 120)$ the streak spacing was $\lambda^+ = 120$; for $\Delta x^+ = 120$ downstream of the end of the rods the streak spacing at $y^+ = 10$ was $\lambda^+ = 118$. Metzler observed that the streak spacing once again reverted to $\lambda^+ = 100$ when y^+ and Δx^+ were greater than the above values.

Using visual observations to study the "loop-like" ejections into the outer region of the boundary layer, Metzler deduced that the surface modifications augmented the momentum transfer process by increasing both the bursting frequency and the vertical ejection velocities.

Walsh and Weinstein (1978) conducted an extensive study of drag and heat transfer on surfaces with small longitudinal (streamwise) surface modifications. The study was performed in the Langley, seven inch by eleven inch, Low-Speed Wind Tunnel Research Facility. A wide variety of models were examined including ones incorporating rectangular, triangular, and semi-circular grooved modifications. Emphasis was placed on geometries which they felt would restrict the turbulent bursts to the near-wall region.

The initial Walsh and Weinstein data showed little indication that rectangular ribbed modifications can be used as a drag reduction mechanism. However, small drag reductions of less than four percent were observed for triangular models with $h^+ = 50$ and $s^+ = 25$ to 50. In addition, some of the results with the triangular models indicated that heat transfer efficiencies could be increased by up to ten percent with respect to that for a flat plate. Walsh and Weinstein concluded that further testing of triangular and alternating convex-concave models should be conducted.

In a subsequent study, Walsh (1979) tested symmetrical and unsymmetrical v-groove riblets, riblets with a rounded apex, and riblets with various transverse curvature. The study employed a mechanical displacement mechanism to measure drag directly. For one model, measured momentum thicknesses, turbulence intensities, and Reynolds stress profiles were comparatively examined in relation to the direct drag results.

Walsh's data indicate that a drag reduction was attained for several symmetric triangular riblet surfaces, for which h^+ and s^+ were less than fifty, with all triangular or v-groove riblets displaying drag reduction when $h^+ < 25$. The amount to drag reduction appears to increase with decreasing h^+ and s^+; the maximum drag reduction determined thus far is seven percent.

Non-symmetric v-groove riblets were also tested in an effort to disturb the natural periodic formation of the streaks and bursts. These data indicate no additional drag reduction in comparison with the symmetric v-groove models

Walsh's model 29, a symmetric v-groove model with h = 0.025 cm and s = 0.051 cm, yielded a maximum drag reduction of seven percent at low velocities. Therefore, an intensive study of this model was conducted. With the free stream velocity maintained at 13.7 m/s, ($h^+ = 10$, $s^+ = 21$) the momentum thickness and Reynolds stress were measured at four locations on the model, and compared to those of a flat plate. Walsh observed the largest reduction in momentum thickness to occur in the first 22 cm ($x^+ = 8706$) of model 29. This corresponds to a sixteen percent reduction in skin friction, when the momentum thickness at the beginning of the test section is assumed equivalent to that of a flat plate. The momentum thickness data further downstream suggests that for extended lengths the ribs become less effective in controlling the momentum exchange process, and thus have a limited effect on skin friction. Hotwire measurements of turbulence intensities and Reynolds stress were again performed and compared to flat plate data. The results show that significant decreases in both properties occur during the first 22 cm ($x^+ = 8706$) of model 29, and then regress toward flat plate values.

All data show that rounding of the apex, or transverse curvature, decreases the drag reduction effectiveness of the modification. In addition, the use of convex or concave surfaces were found to generally increase relative drag as well.

Walsh (1982) conducted a further study to 1) improve past direct drag measurements, 2) determine the effect of flow incidence angle, and 3) further examine the effects of rib height, spacing, and geometry on drag reduction.

A deflection sensor was installed on the drag measurement system to improve the accuracy of the direct drag measurements. The new data indicate that riblets with h^+ on the order of the burst range ($y^+ = 30$), and s^+ within the turbulent wall streak range ($\lambda^+ = 100$), can result in net drag reductions of up to six percent.

For moderate flow velocities, Walsh's data indicates that flow incidence angles up to fifteen degrees have little effect on the magnitude and region of drag reduction. However, for velocities above 20 m/s it was observed that increases in flow angle could increase drag by six percent.

Walsh (1982) made several modifications to the symmetric v-groove riblet geometries in an effort to increase the magnitude and velocity range of the drag reduction. New test models included right angle riblets, (one side of the rib is vertical) several different valley curvatures, and ribs with a grooved or flat apex.

Tests using right angle ribs indicate that small ribs yield the same drag reduction magnitude as the identical height and spaced symmetric rib. For a higher right angle rib, with the same spacing as the short right angle rib, the magnitude of drag reduction is no different than that of a symmetrical rib of identical height and spacing. However, Walsh observed that the velocity range of drag reduction is increased slightly for the higher right angle ribs, with respect to identical height and spaced symmetrical v-grooves. Also, it was observed as with symmetric ribs that the drag reduction decreases as rib spacing becomes large.

Tests were performed holding height, spacing, and peak geometry constant to determine what effect various valley curvatures might have on drag reduction. Walsh determined that valley curvature has no apparent effect on drag reduction.

Finally, Walsh observed that grooving the peak does not alter the magnitude of drag reduction, but expands the velocity range over which drag reduction is experienced.

Hence, Walsh has determined that symmetric riblets and right angle riblets, with $h^+ < 25$ and $s^+ < 50$, appear to cause a drag decrease. Rounding of the apex tends to reduce the magnitude of the drag decrease, while valley curvature does not effect the amount of drag reduction. Grooved peaks do not alter the magnitude of drag reduction, but do extend the upper velocity range over which drag reduction occurs. He also determined that non-symmetric spacing of the triangular riblets has no additional effect of drag reduction with respect to the symmetric ribs. Other riblet configurations, such as rectangular ribs, do not appear to be useful as drag reduction mechanisms.

Although Walsh has conducted numerous studies on various geometric configurations, his studies lack the quantitative and qualitative data obtainable from visual and hot-wire studies, which are necessary to physically understand why only certain riblets should reduce drag.

1.3 PRESENT STUDY

Studies of streak formation and bursting have resulted in the hypothesis that such events play an important role in the transport of energy within a turbulent boundary layer. Despite the fact that low-speed streaks are present in the viscous sublayer, only Metzler (1980) attempted to study modifications of approximately the viscous sublayer's scale.

The origin of streaks in the viscous sublayer suggests that the mechanism which causes their formation, and thus the initiation of the turbulent momentum exchange process, must also be present in this region. The authors feels that modifications of the order of the viscous sublayer should have a significant influence on the streak formation mechanism, since they will be influencing the streaks from inception to $y^+ \cong 10$, where the bursting process is initiated.

The results of Metzler (1980) and Walsh (1979 & 1982) indicate the need for a comprehensive visual study of streamwise surface modifications that scale on the order of the viscous sublayer.

However, relying strictly on one method of observation can lead to misinterpretation of the data. Therefore, the present study utilizes both visual data and hot-film data.

The research objectives of this study are:

1) To examine whether artificial streamwise surface modifications can alter the spacing and characteristics of low-speed streaks.
2) To correlate both visualization and hot-film results with observations made by Metzler.
3) To determine the effect of the modifications on surface drag and conventional turbulence parameters.

Subsequent chapters will describe the experimental flow facility, apparatus and techniques, the experimental results and a discussion thereof, and conclusions. A section of appendices contains figures for all test data and discussions of details not pertinent to the scope of the main text.

2 EXPERIMENTAL APPARATUS

2.1 FLOW CHANNEL

The Lehigh University free-surface plexiglass water channel was utilized for the present study. The facility is 0.9 m wide, by 0.35 m deep, by 5.0 m long. Stable channel flow is obtained in the range from 0.02 m/s to 0.6 m/s by means of a feedback control circuit that monitors pump shaft speed. A turbulence intensity of 0.3 percent at 0.3 m/s and a spanwise flow uniformity of ± 2 percent are achievable through the use of a 15 cm thick inlet-maniforld damping sponge and honeycomb flow straightener-screen combination. Figure 2.1 is a schematic representation of the flow system.

In an effort to prevent permanent damage to the channel bottom, two removable flat plates of 2.5 m length were employed as the test surfaces. Monofilament fishing line mounted on these test surfaces was used to create the modified test surfaces.

2.2 TEST PLATES

Plate-1, shown in figure 2.2, was constructed of 6.35 mm thick plexiglass with a 6:1 half-ellipse leading edge. Streamwise ribs were used to stiffen the plate, and nine 15 cm adjustable legs were used to support the plate above the channel floor and out of the floor boundary layer.

As shown in figure 2.3a, the modified test surface was created by attaching the monofilament line to an upstream connection plate, stretching the lines over the leading edge, along the top surface, and under the trailing edge, where the lines were attached to a trailing edge connection plate. By following the contour of the leading edge, abrupt flow obstructions, as were the case in Metzler's study (1980), were avoided.

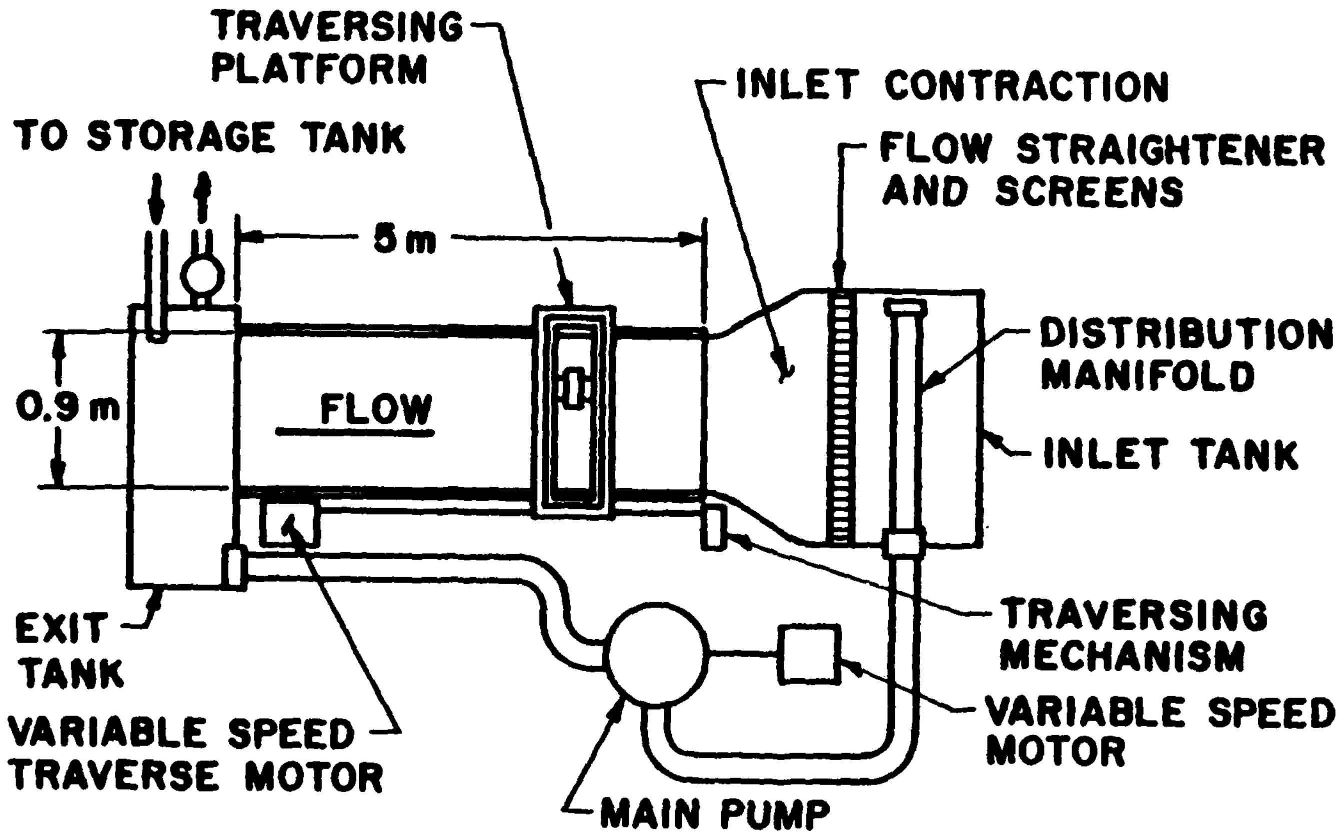

Figure 2.1. Schematic representation of Lehigh University free-surface water channel.

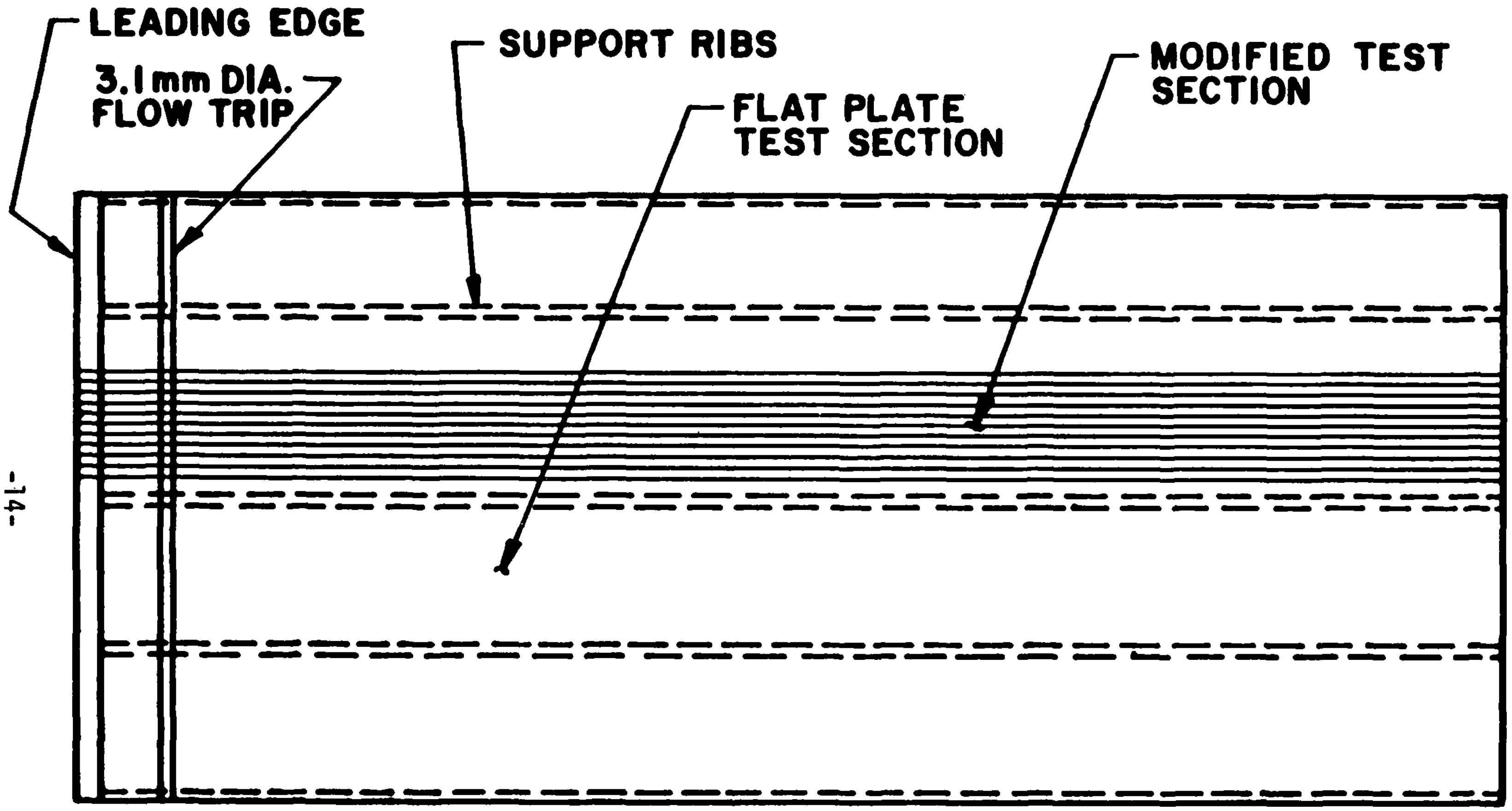

Figure 2.2. Schematic diagram of test plate-1.

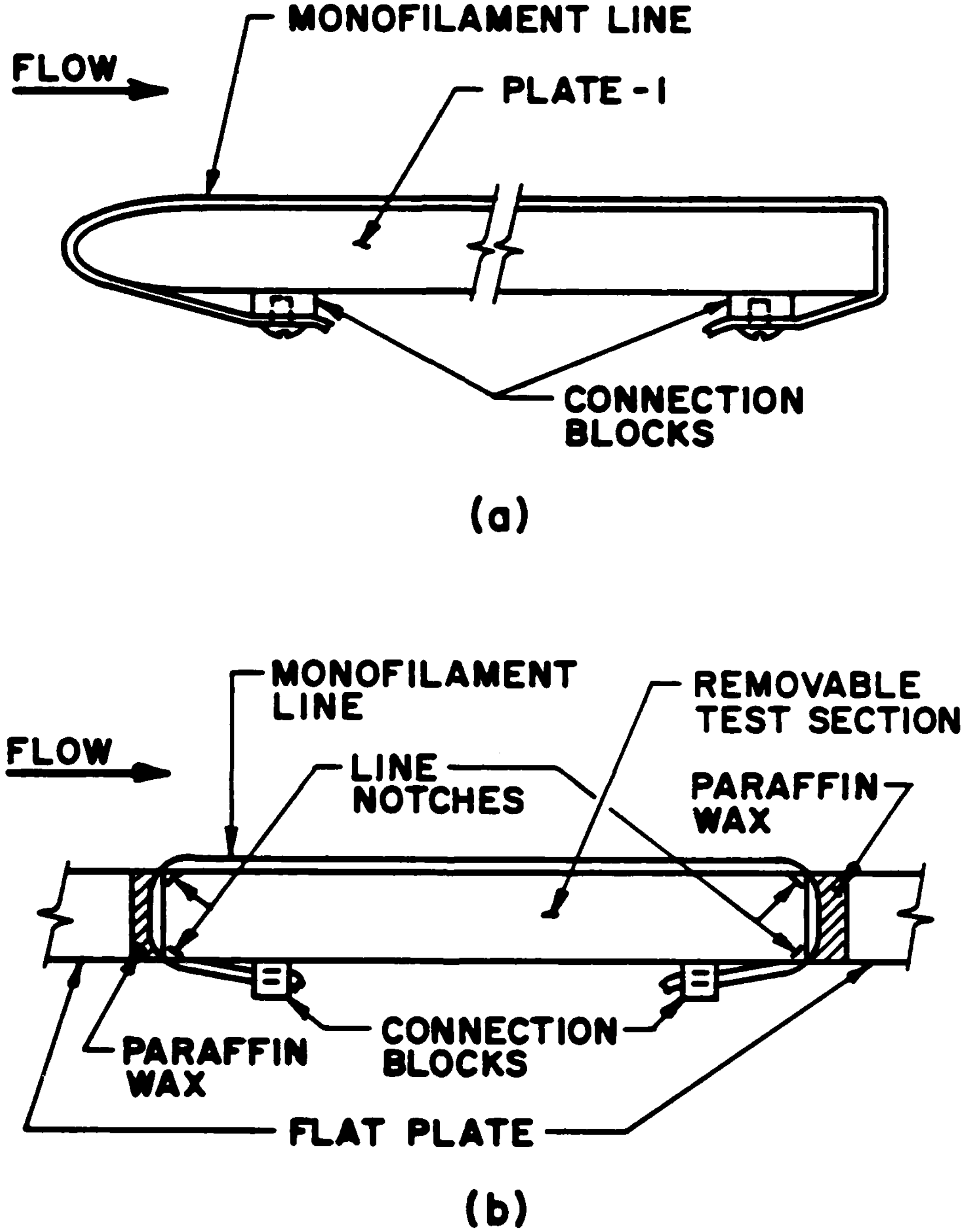

Figure 2.3. (a) Schematic of line attachment to test plate-1; (b) Schematic of line attachment to removable test section, test plate-2.

The two thin plexiglass connection plates were fastened to the underside of plate-1, one 10 cm behind the leading edge and the other 5 cm upstream of the trailing edge. Each connection plate had machine screws positioned 5 mm apart in the transverse direction, thus providing a means of anchoring the monofilament line.

Plate-2, shown in figure 2.4, was constructed of 12.70 mm thick plexiglass. The leading edge was a 5:1 half-ellipse. Seven streamwise ribs and two transverse ribs were used to stiffen the plate, and twenty-four 10 cm adjustable legs were used to elevate the plate above the channel surface.

Unlike plate-1, which had surface modifications located over the entire length of the plate, the surface modifications for plate-2 were located on a removable 0.15 m by 1.22 m test section, beginning 0.91 m behind the leading edge, as shown in figure 2.5. Since an unmodified flat plate surface preceded and followed the removable test section, the streak mechanism could be studied as it impinged and departed the streamwise surface modifications.

Since only 0.305 mm (0.012 in) diameter line was to be tested on plate-2, the connection blocks were slightly different than for plate-1. Holes were bored every 8.89 mm (0.35 in), to accept passage of the 0.305 mm diameter line, which was pulled through and fastened with cyanoacrylate adhesive.

Jewelers files were used to cut fine notches, every 8.89 mm in the transverse direction, in the top and bottom of the leading and trailing edges of the test section. The modifications therefore gradually ascended and descended at the leading and trailing edges of the modified test section, respectively, minimizing bluff body inpingement effects of the line (see figure 2.3b). The joints between the removable test section and the flat plate were filled with paraffin wax and scraped flush to the flat plate surface with a razor blade to eliminate any cavity effects.

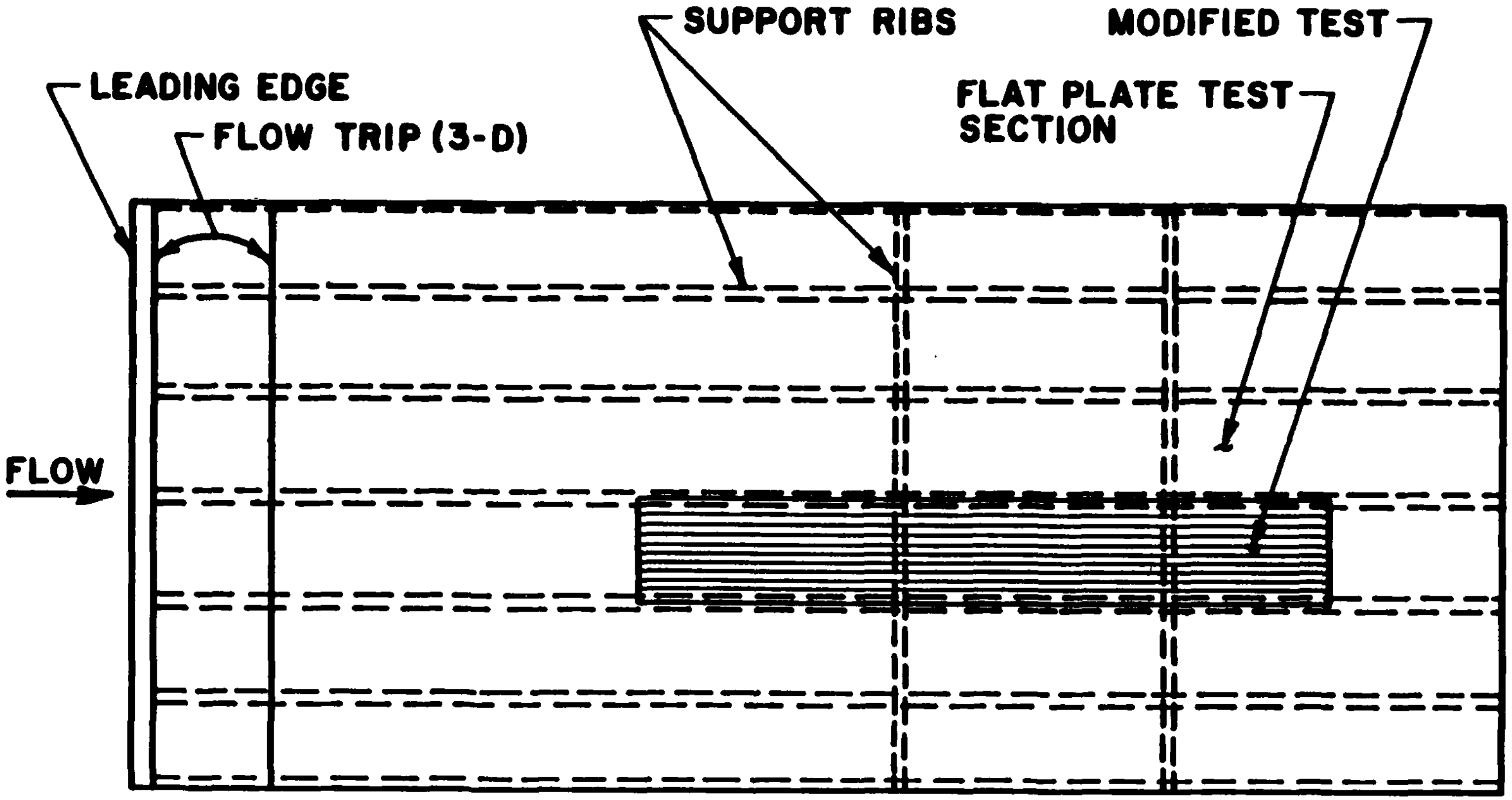

Figure 2.4. Schematic diagram of test plate-2.

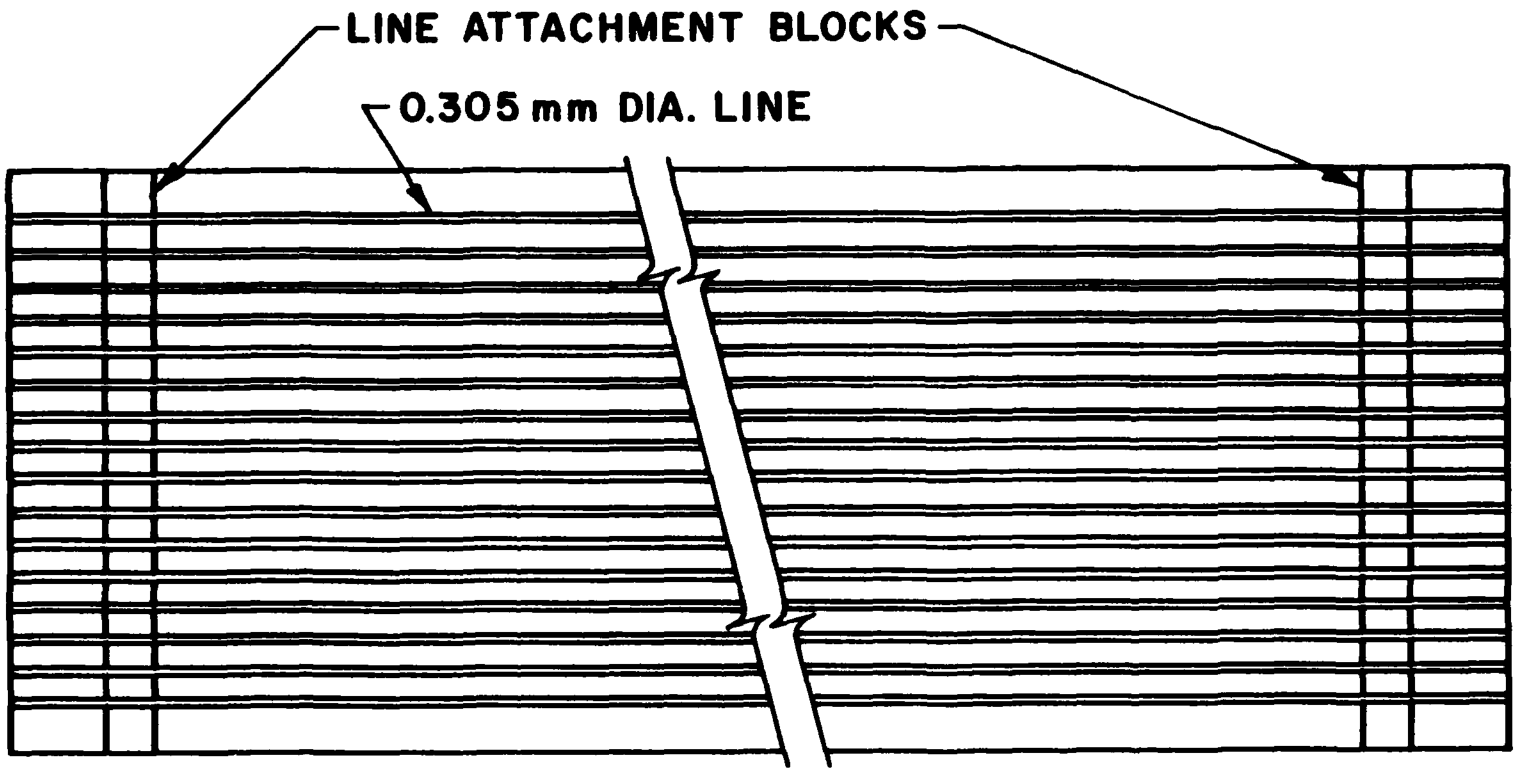

Figure 2.5. Top-view of removable test section, test plate-2.

2.3 FLOW TRIPS

Studies conducted with test plate-1 utilized a 3 mm diameter brass rod, located 15 cm (6 in) downstream from the leading edge, to trip the flow. However, since measurements were to be performed only 0.91 m from the leading edge on plate-2, it was essential that the flow be fully developed by this point. Thus a three-dimensional flow trip was designed to facilitate this rapid development.

Klebanoff et al. (1955) observed the effect of three-dimensional roughness spheres (1/32, 1/16, and 1/8 inch diameter) on transition. The spheres were cemented in single rows to a flat plate, at spacings of 2k, 4k, and 8k, where k is the height of the roughness element. Klebanoff found that for all spacings tested, for transition to occur at the roughness element it is necessary to have a critical roughness Reynolds number, $(U_k\ k/\nu)_{cr} = 500$, where U_k is the velocity at the height of the sphere.

The present 3-D flow trip was designed to incorporate Klebanoff's bead spacing and roughness Reynolds number (Re_k) findings. A schematic representation of the three-dimensional flow trip employed is shown in figure 2.6. The flow trip consisted of eight rows of plastic "quasi" hemispherical roughness beads cemented to a 1.04 mm thick sheet of window plastic that was cemented to plate-2, 38.10 mm behind the leading edge. The beads in the first four rows of the trip were 3.36 mm in diameter and 1.91 mm high, which corresponds to a $Re_k = 490$ at the first row of roughness beads for a free stream velocity of 0.251 m/s. The last three rows consisted of beads 3.86 mm in diameter and 3.12 mm high. Small and large beads were alternated to construct the fifth row as a bead transition row. The transverse bead spacing of the first five rows was 9.53 mm (3/8 in), or roughly 5k, where k is the

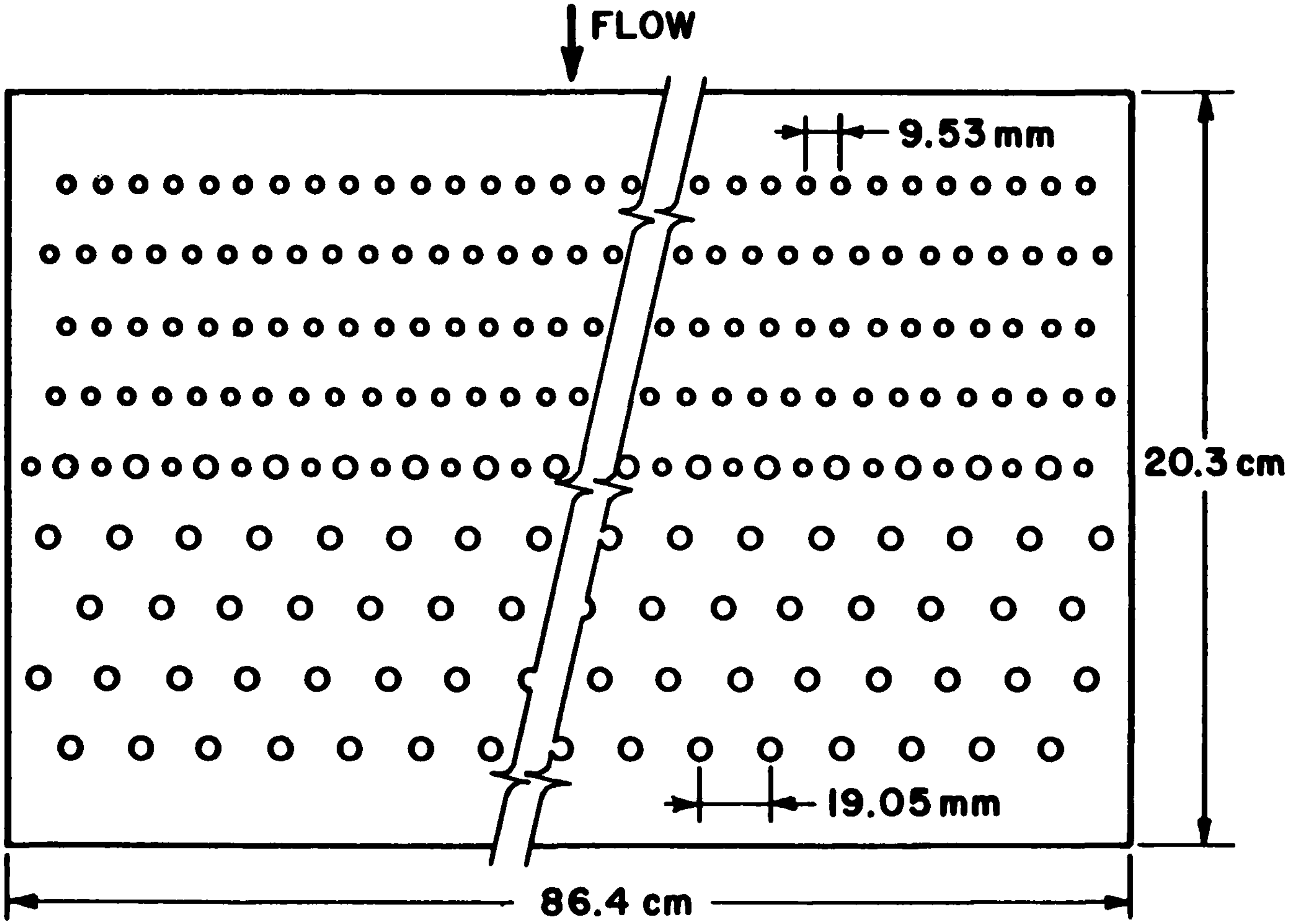

Figure 2.6. Schematic representation of three-dimensional flow trip employed with test plate-2.

height of the roughness beads. The transverse bead spacing of the last three rows was 19.05 mm (0.75 in), or roughly 6k. All rows were spaced 19.05 mm in the streamwise direction. To limit flow distortion strictly to the "quasi" hemispherical beads, the leading and trailing edge of the trip were tapered.

Purtell et al. (1981) suggests that as the flow becomes fully developed the velocity profiles will converge to an asymptotic profile in the outer region of the boundary layer. Mean velocity profiles for three different streamwise locations on the flat plate are shown in figure 2.7, starting at the location of the upstream edge of the removable test section. Since all profiles in figure 2.7 appear to asymptote in the outer region, the flow appears to be essentially developed by the leading edge of the removable test section.

2.4 VISUALIZATION

The hydrogen bubble-wire technique of flow visualization was utilized to study the streak structure above both the flat plate and the modified test sections. This method, the specifics of which are described in further detail in Metzler (1980) and Smith (1978), uses a 25 μm diameter platinum wire as the cathode in an electrolysis process. A 0.6cm diameter graphite rod, located in the flow approximately 20 cm from the bubble-wire, was used as the anode. Time-lines of hydrogen bubbles are produced by a generator unit capable of variable pulse rates from 0.2 to 340 Hz with variable duty cycles. Generally, pulse frequencies of 60 Hz and 120 Hz are used, because these frequencies 1) yield distinct bubble lines of sufficient density to clearly mark the low-speed streak structure for the flow velocities under consideration, and 2) are synchronized with the framing rate of the video

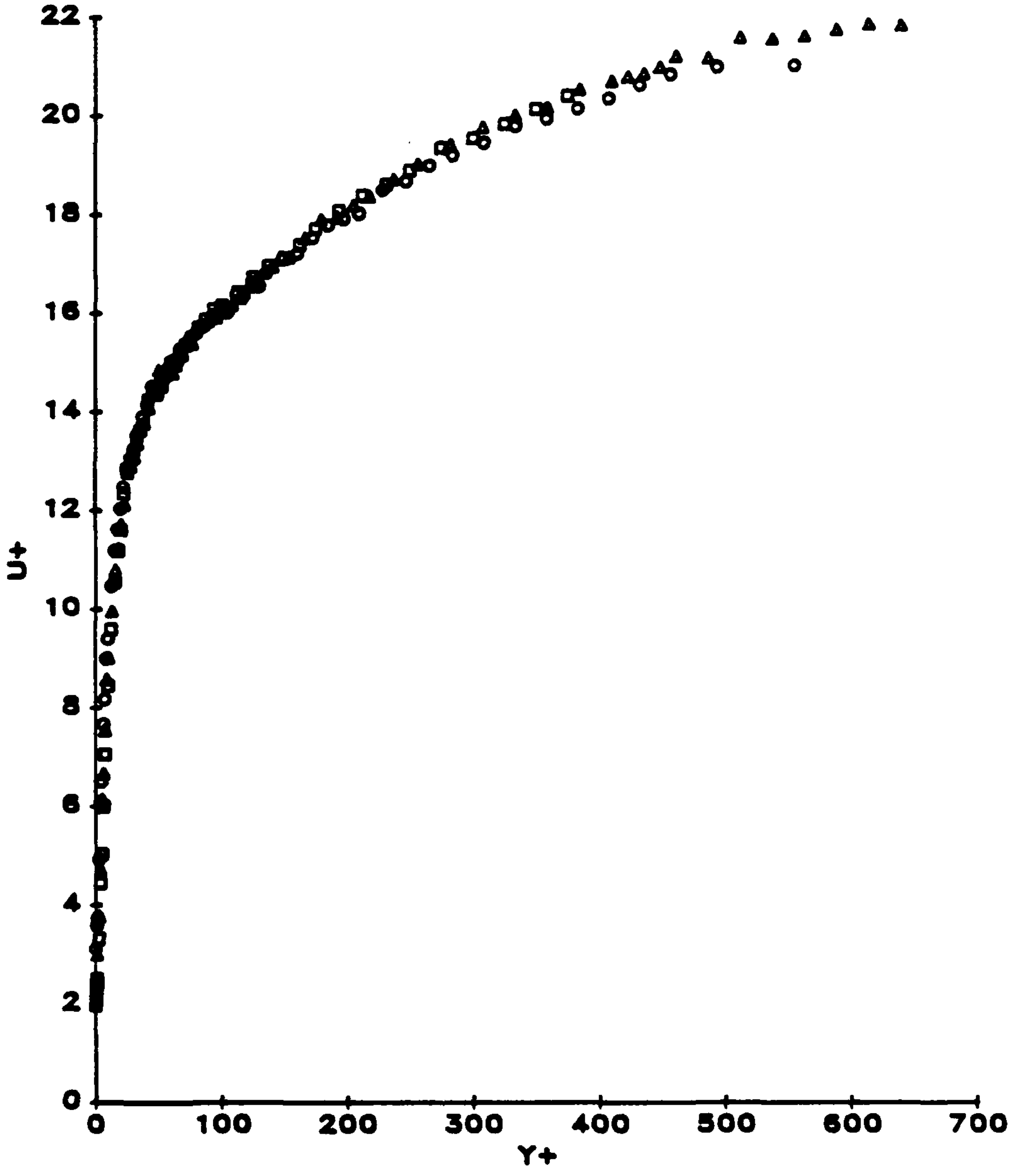

Figure 2.7. Measured velocity profiles for unmodified flat plate test section, test plate-2. Hot-film probe location referenced from the leading edge: □, 0.84m; ○, 1.52m; △, 2.06m.

recording system, which eliminates the jerky motion of the bubble lines when viewed in slow motion.

The video recording system is an INSTAR high-speed, two-camera, magnetic tape system, manufactured by the Video Logic Corporation. When coupled with one or more synchronized strobe lights, the system provides 120 frames/second with an effective frame exposure time of 10 μs. The short exposure time and small fields-of-view obtained with conventional lenses (as small as 6×6 mm at distances of 0.5 m) allow the details of turbulent boundary layer structure to be clearly observed. The pictures are viewed on a high resolution, 250 horizontal line monitor with a horizontal sweep frequency of 25.5 KHz. Playback modes that allow detailed study include real time, 3% to 15% real time, slow-motion backup, and single-frame sequencing.

Hard copy capability is provided by interfacing the system to a videographic printer. The printer is a raster scan device which projects the video signal onto dry silver paper via a special cathode-ray tube. The latent image is then heat processed yielding linear 17 cm × 11 cm single frame pictures of the video output.

2.5 CHANNEL TRANSVERSE PLATFORM

Flow visualization and hot-film studies are aided by a special traversing platform that has supports for the mounting of both plan and side-view video cameras, as well as the hydrogen bubble-wire probes. Removal of the plan-view video camera allows a hot-film probe traversing mechanism to be mounted on the support platform. Details of the hot-film traversing mechanism are presented in appendix A. A lower platform, which is manually operated, is used to mount the strobe lights used to backlight the hydrogen bubbles. Figure 2.8 is a schematic representation of the camera and lighting positions used during the present study.

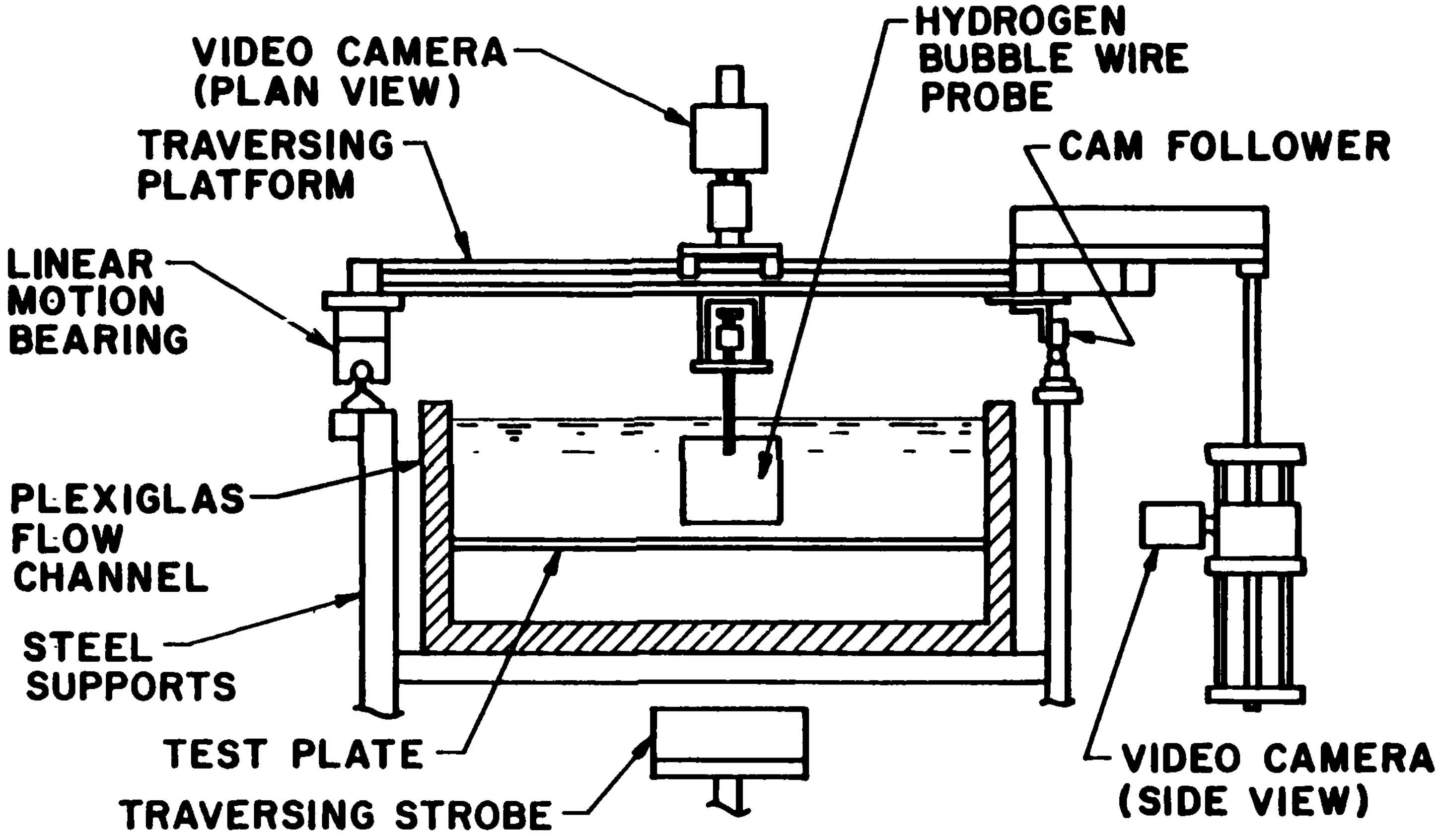

Figure 2.8. Schematic representation of camera and lighting positions as viewed from upstream.

The support platform travels along two 3.8 cm diameter by 4.1 m long hardened steel shafts, supported at 0.3 m intervals by adjustable mounts. Two Thompson linear motion bearings on one shaft and two heavy ball bearing cam followers on the other shaft smoothly and accurately guide the platform along the steel shafts.

A steel cable drive system incorporating a reversible Reliance Electric variable speed drive motor is used to drive the camera and hot-film support platform system. The support platform system, which is capable of uniform velocities of 0 to 0.5 m/s, was used both for locating the cameras and flow probes in the streamwise direction, and for towing hot-film probes for probe calibration.

2.6 ANEMOMETRY

In order to determine the basic parameters of the turbulent boundary layers, and to correlate velocity behavior with visual results, a single-sensor hot-film anemometer system was employed to measure both mean velocities and turbulence intensity data. The system consists of a Disa 55D01 constant temperature anemometer, Disa 55M25 linearizer, either a Disa 55R11 or 55R15 quartz hot-film probe, and a TSI 1076 voltmeter.

To calibrate the hot-film probe prior to a measurement, the hot-film probe traversing mechanism was mounted on the upper moving support platform described earlier in this chapter; the probe was then calibrated by towing it through a quiescent channel over a range of velocities, with the maximum velocity slightly greater than the maximum free-stream velocity to be measured. The details of the linearization process are discussed in appendix B. During the calibration, particular care was taken to assure linearity at the low end of the range since it was speculated that the streamwise modifications might significantly alter the near wall region ($y^+ < 40$) of the boundary layer.

3 EXPERIMENTAL RESULTS

This chapter presents the results of the experimental investigation of streamwise surface modifications and the effect they have on a turbulent boundary layer. The chapter is divided into three main sections. The first section presents the results of the visual studies. The second section focuses on streak spacing and the statistics thereof. Finally, the third section presents the results of a series of hot-film anemometer measurements.

3.1 VISUAL RESULTS

During the present study, both plan-view and side-view video recordings were utilized to observe streak behavior. The plan-view is the most effective view for observation of the lateral position and movement, length, pairing, and merging characteristics of low-speed streaks. The side-view recordings are the most effective method of observing the bursting mechanism and the mixing of the fluid ejected by the bursting process.

Plan-view hydrogen bubble-wires were oriented such that the wire was parallel to the flat plate and perpendicular to the free stream velocity. Since the wire was soldered to the tips of the bubble probe supports, the bubble-wire was indexed to $y^+_{wire} = 0$ by lowering the bubble probe until the tip of the probe support and thus the bubble wire contacted the plate. The initial instant of contact is established when the bubble-wire and its image reflected by the flat plate appeared to touch. Traversing the bubble probe vertically upward from $y^+_{wire} = 0$ allowed plan-view visualization of the low-speed streaks at $y^+_{wire} = 5, 10, 15, \& 20$. Unless specified otherwise, all y^+_{wire} values in this and subsequent chapters will be referenced to the unmodified flat plate test surface.

The orientation of the bubble-wire during side-view visualization was perpendicular to both the flat plate and the free stream velocity. Generally, side-views were conducted with the tip of the bubble-wire located just above the plate surface (in the case of a modifying line, this surface would be the top of the line).

3.1.1 PLAN-VIEW BUBBLE-WIRE AT $y^+_{wire} \leq 10$

This section presents the results of a series of plan-view studies with the hydrogen bubble-wire located at $y^+_{wire} \leq 10$. The characteristics of the streaks above the unmodified flat plate will be discussed first and then compared to streak characteristics above the adjacent modified surface.

3.1.1a UNMODIFIED SURFACE

Figure 3.1.1 is a plan-view polaroid picture of the "typical" streak structure above an unmodified flat plate. The bright horizontal line at the top of the picture is the bubble-wire. The low-speed streaks appear as the bright streamwise concentrations of bubbles. Note that the streaks are quite straight in the stream-wise direction (eg. from the bubble-wire to B on the figure). For descriptional purposes, the region from the bubble-wire to A, as indicated on figure 3.1.1, was defined in the present study as the streak "head" (approximately $\Delta x^+ = 80$ downstream from the bubble-wire). The remainder of the streak was defined as the streak "tail" (A to B on figure 3.1.1).

Lateral movement of the streaks is a characteristic that was observed, but the streaks usually remained straight during this movement. The lateral movement of streaks was generally observed when an adjacent

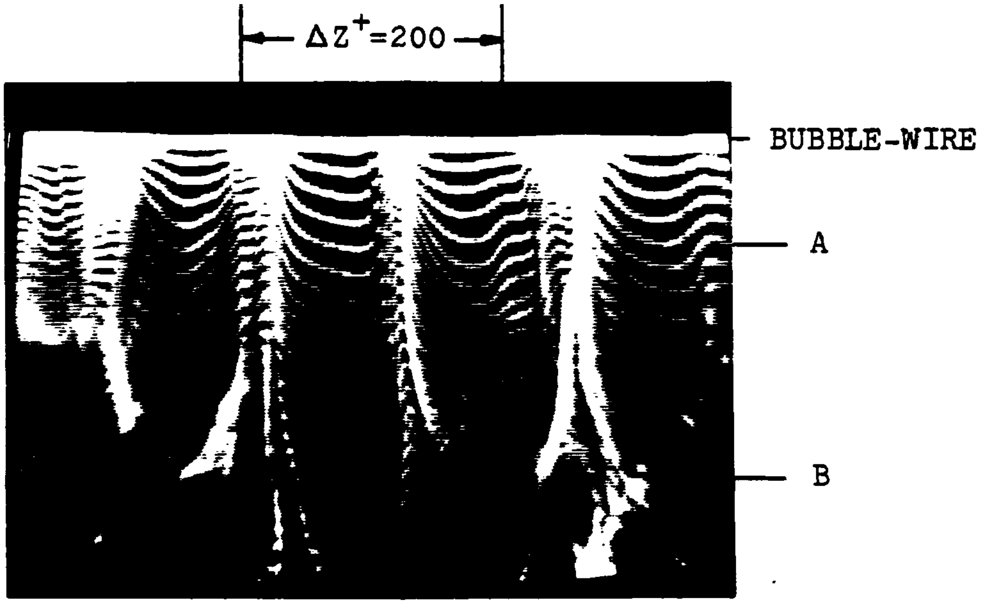

Figure 3.1.1. Plan-view showing streaks above the flat plate. Flow top to bottom. $Re_\Theta \simeq 1400$, $y^+_{wire} = 9.7$, and $f_b = 120$ Hz.

streak was bursting, which resulted in pressure fluctuations which affect the location of the adjacent streaks. Occasionally the head of the streak would remain at a fixed lateral location on the bubble-wire and the streak tail would undergo lateral movement. This is defined as streak waviness and was observed infrequently above the flat plate. Figure 3.1.2 depicts streak waviness.

Streak pairing is often observed above a flat plate. Streak pairing (grouping) occurs when two, three, and once and a while four streaks group themselves with a very small high speed region ($\lambda^+ = 20\text{-}40$) between the adjacent streak(s). Streak pairs have been observed to merge and form one streak. Dual pairs have also been observed to burst simultaneously. However, usually one of the streaks will burst and leave the other streak(s) unchanged except for some lateral motion.

Normally, when a streak above a flat plate bursts most of the streak is ejected downstream and into the outer region of the boundary layer. A complete streak bursting is shown at CB in figure 3.1.3. Note that at CB the bubble lines between the bubble-wire and the bursting streak indicate no velocity deficit, but to either side of the bursting streak head, at N1 and N2, there are two new streaks forming. Usually during complete streak bursting one or two new streaks will form in proximity to the bursting streak head. If two new streaks form, they sometimes move apart and appear as two separate streaks. However, most of the time these new streaks move inward toward each other, taking up the transverse position of the old (burst) streak, and appear as a streak pair which sometimes merges to form a single streak prior to the next burst.

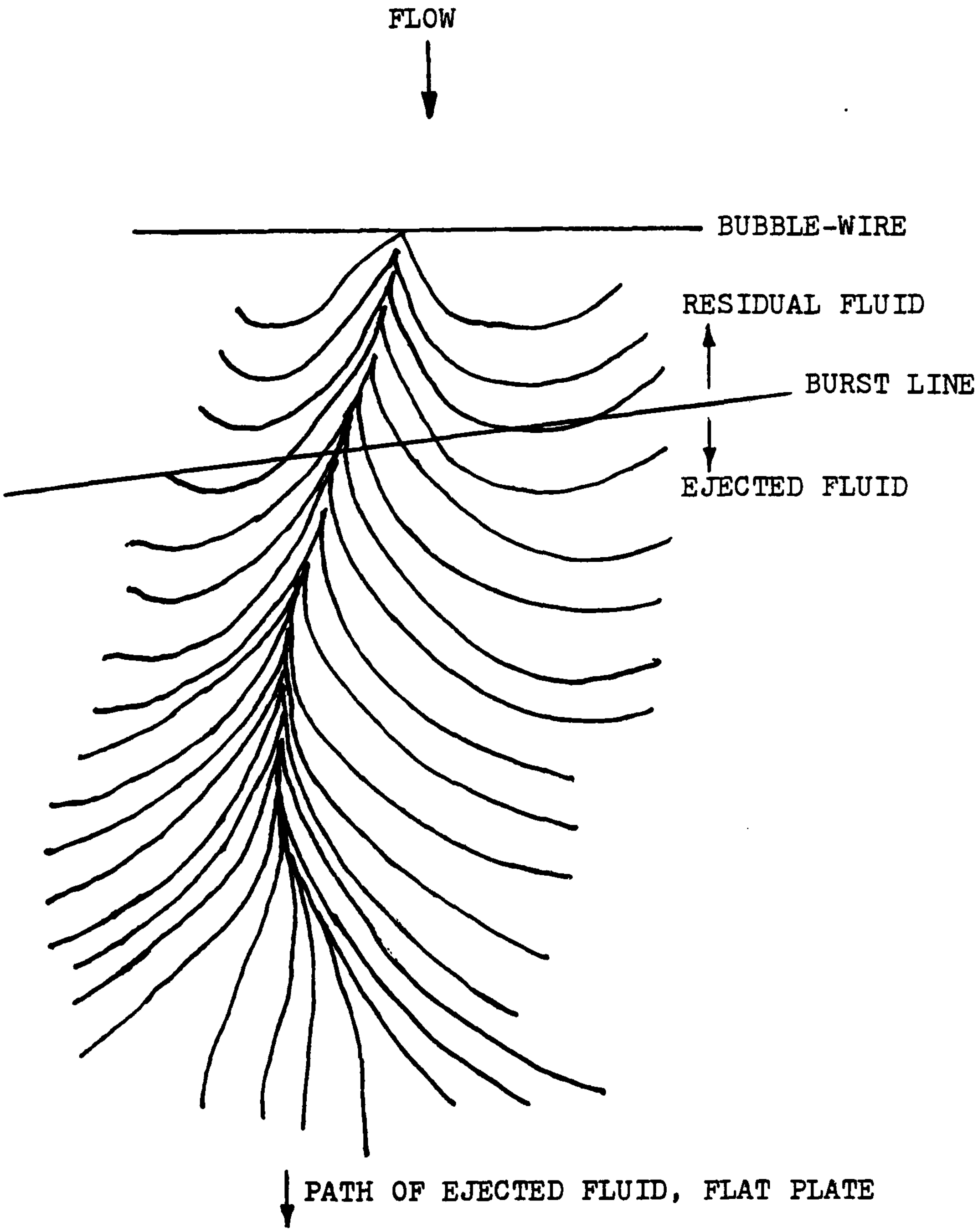

Figure 3.1.2. Schematic representation of streak waviness.

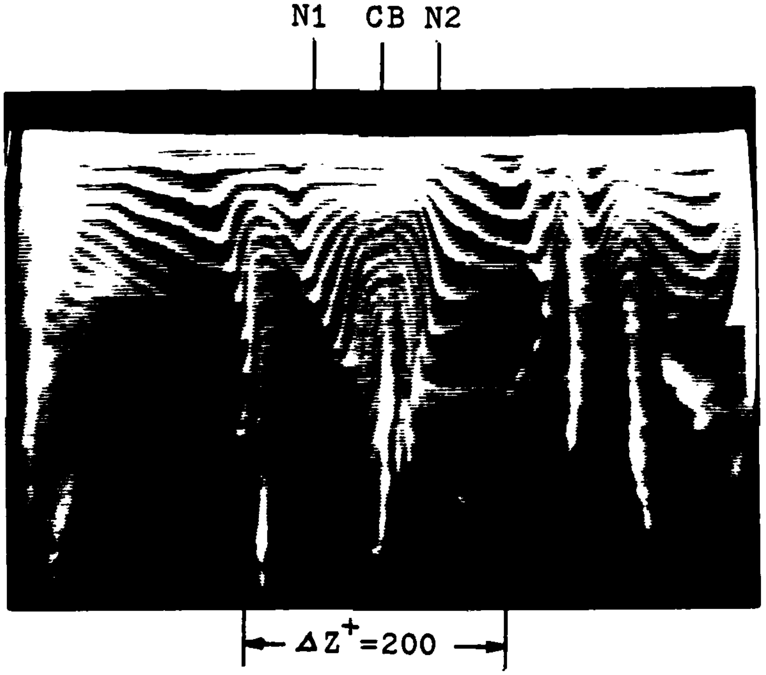

Figure 3.1.3. Plan-view showing complete burst above the flat plate and two new streaks forming at the head of the bursting streak. Flow top to bottom. $Re_\Theta \simeq 1400$, $y^+_{wire} = 5.5$, and $f_b = 60$ Hz.

Generally, streaks do not burst completely. Commonly, when a streak exhibits waviness, the streak will undergo partial bursting. During partial streak bursting only the tail of the streak (the section of the streak downstream of the "burst line" in figure 3.1.2) is ejected. The ejected fluid is observed to travel directly downstream as indicated on figure 3.1.2. All fluid upstream of the "burst line" remains as a residual streak, which either redevelops into a complete streak, or may be ejected shortly after the partial burst.

3.1.1b MODIFIED SURFACES

Discussion of the characterisitics of low-speed streaks forming above the modified test section follows. However, it is to be pointed out that although the flow characteristics above the modified surfaces exhibited some differences from those occurring above a flat plate, the low-speed streaks are still the dominant near-wall flow structure and are essentially the same coherent mechanism in both cases.

Figure 3.1.4 (a,b, & c) is a series of plan-view pictures of the streak structure occurring above the modified test sections with $s^+ = 71$, 111, and 142, respectively. The monofilament line modifications appear as the light vertical lines upstream of the bubble-wire (indicated on the figure). Figure 3.1.4 suggests that the modifications, regardless of s^+, can affect the location and organization of low-speed streaks.

Some streak pairing was observed to occur above the modified surfaces, as is displayed by the weak triple pair centered about point A in figure 3.1.4b. However, streak pairing was observed far less commonly above the modified surfaces than above the flat plate. Most observed streak pairs consisted of two streaks; no multiple pairs were observed above the modified surfaces.

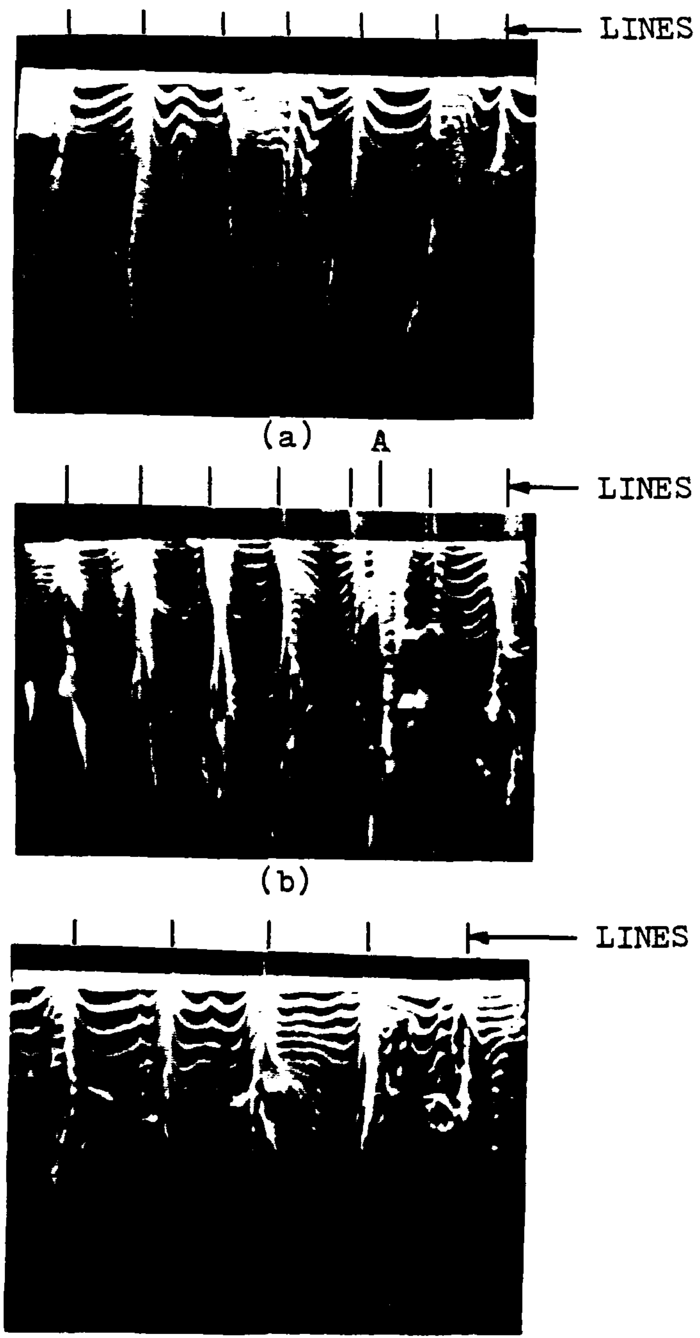

Figure 3.1.4. Plan-view illustrating good streak to line correlation. Flow top to bottom. $Re_\Theta \approx 1400$, $f_b = 60$ Hz. (a) $y^+_{wire} = 4.5$, $h^+ = 4.3$, and $s^+ = 71$, (b) $y^+_{wire} = 4.0$, $h^+ = 3.8$, and $s^+ = 111$, (c) $y^+_{wire} = 9.3$, $h^+ = 4.3$, and $s^+ = 142$.

Streaks above modified surfaces were also observed to move laterally, but to a lesser degree than those above a flat plate. Streaks forming near a line tended to move toward and focus above that line. However, streaks forming above the modified surfaces tended to behave in a more wavy manner than those forming above a conventional flat plate (see figure 3.1.2). Streaks A, B and C indicated in figure 3.1.5 are an example of the streak waviness as it occurs above the lines.

Another streak characteristic which is more prevalent above a modified surface than a flat plate is partial streak bursting. Wavy streaks which undergo partial bursting sometimes behave differently above the modified surfaces than above a flat plate. The ejected fluid from approximately 10-25% of the wavy-streak partial bursts was observed to continue moving laterally as it propagated downstream. Lateral movements of as much as $\Delta z^+ = 150$ were observed as the ejected fluid propagated $\Delta x^+ = 450$ downstream. Also, when the streak location tends to be strongly influenced by the presence of the lines, all the streaks in a major portion of the field-of-view ($\Delta z^+ \cong 300$) will often simultaneously undergo partial bursting. Such an occurrence is shown in figure 3.1.6 where streaks between A and B have all partially burst, as evidenced by the short length and the abrupt termination of the tails of each streak, unlike the streaks at E and F. Also, note the ejected fluid marked by the bright concentration of bubbles at the intersection formed by locations D and C.

Although partial streak bursting was the more frequently observed bursting behavior for the modified surfaces, complete bursting still occurred. The complete streak bursting occurring above the modifications was observed to be essentially identical to that observed above a flat plate.

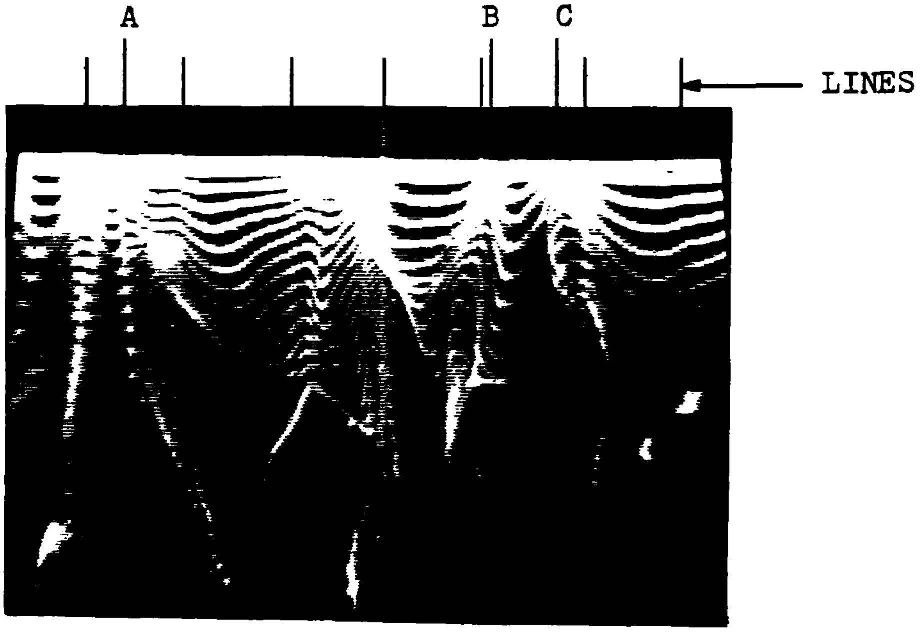

Figure 3.1.5. Plan-view showing streak waviness above modifications. Flow top to bottom. $Re_\Theta \simeq 1400$, $y^+_{wire} = 10$, $f_b = 120$ Hz, $h^+ = 4.3$, and $s^+ = 71$.

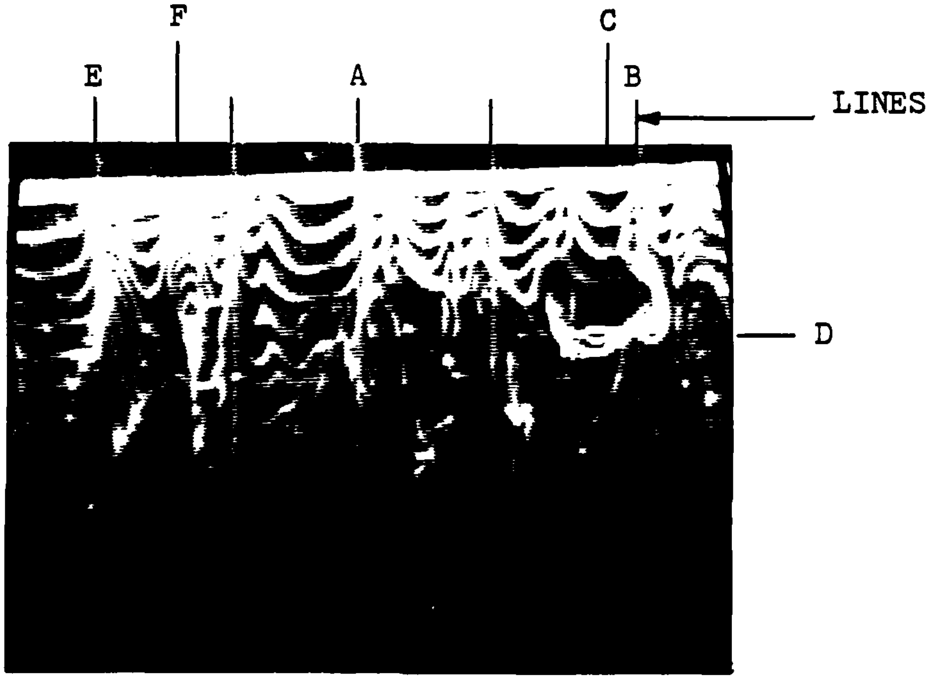

Figure 3.1.6. Plan-view illustrating partial bursting over spanwise range $\Delta z^+ \approx 300$ (A to B). Flow top to bottom. $Re_\Theta \approx 1400$, $y^+_{wire} = 9.3$, $f_b = 60$ Hz, $h^+ = 4.3$, $s^+ = 142$.

In summary, when the flow is visualized with a horizontal bubble-wire located at $y^+ \leq 10$, the modifications are observed to influence the location of the low-speed streaks. The streaks tend to appear more wavy above the modifications than they are above a flat plate. Partial bursting tends to occur more frequently above the modifications than above the flat plate. Lateral movement of ejected fluid occurs for 10-25% of the partial bursts above modified surfaces. Finally, complete bursts occurring above both the modifications and the flat plate tend to spawn one or two new streaks immediately adjacent to and upstream of the head of the bursting streak.

3.1.2 PLAN-VIEW; BUBBLE-WIRE $y^+_{wire} \geq 10$

The reader should acknowledge that the "streak" is the appearance manifested by the visualization method. Obviously, the patterns interpreted as low-speed streaks can be expected to change as y^+_{wire} is increased. In essence, we are visualizing portions of a three-dimensional, low-speed region, thus it should be borne in mind that when we describe the patterns and their behavior at different levels above a flat plate or modified plate, we are describing the change in the perceived behavior of the flow structures at a certain level, not different flow structures. The following are then the streak characteristics which are observed above the flat plate with $y^+_{wire} > 10$.

Generally, streaks are still observed to undergo small lateral movement, as was observed for $y^+_{wire} \leq 10$. However, streak waviness is essentially non-existent. During complete bursting, new streaks do not appear to form immediately adjacent to and upstream of the head of the bursting streak as was observed with $y^+_{wire} = 5.5$. Finally, streak pairing is more prevalent for $y^+_{wire} > 10$, and may be linked to an observed increase in mean streak spacing.

With bubble-wire located at $y^+_{wire} > 10$, the modifications appear to have a reduced effect on streak occurrence. This is illustrated in figure 3.1.7 which indicates that the streaks no longer are observed to directly coincide with each line. Also, the streaks demonstrate much less lateral waviness and are found to relax toward a spanwise spacing which is similar to that determined for streaks occurring above a flat plate.

Streak pairing, examples of which are indicated by P1 and P2 in figure 3.1.7, is observed more frequently for $y^+_{wire} \geq 10$ above the lines. Since streak pairing was rare for $y^+_{wire} \leq 10$, and streak pairing is common above a flat plate, streak pairing for $y^+_{wire} > 10$ further indicates that the stabilizing effect of the lines on streak location rapidly diminishes with distance above the lines. Apparently, an interaction of adjacent streak regions begins a short distance above the plate, which rapidly diminishes the "focusing" effect of the lines. This loss of "focus" can be observed in figure 3.1.7, although the location of streaks A,B, and C still are observed to essentially coincide with the line locations.

With $y^+_{wire} > 10$ above modified test surfaces, streak bursting no longer appears as a mixture of partial and complete bursts, as it did for $y^+_{wire} \leq 10$. Only complete bursting is observed and new streaks do not necessarily form immediately adjacent and upstream of the head of the bursting streak, as was observed for streaks above the flat plate.

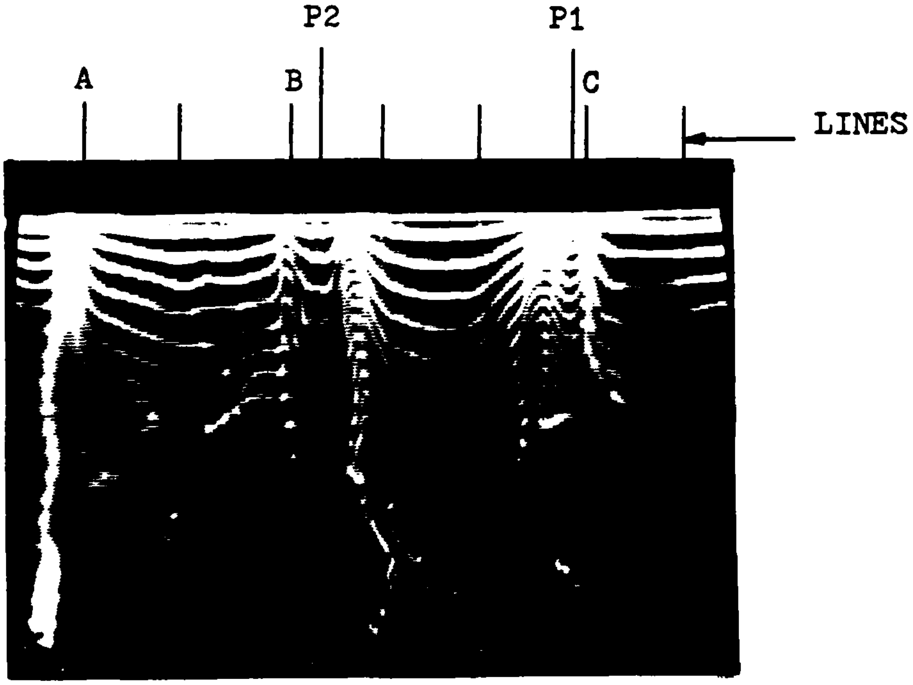

Figure 3.1.7. Plan-view illustrating the diminished effect of the lines on the formation and location of the streaks. Flow top to bottom. $Re_\Theta \approx 1400$, $y^+_{wire} = 15$, $f_b = 120$ Hz, $h^+ = 4.3$, and $s^+ = 71$.

To summarize, the low speed streaks visualized with $y^+_{wire} > 10$ do not appear to rigorously coincide with the modifications. The streaks tend to occur farther apart, with apparent streak pairing observed quite frequently. Observations above the modified surface indicate streak behavior very similar to that above a flat plate. Complete streak bursting occurs above both the flat plate and the modifications, but new streaks do not appear to form immediately adjacent to and upstream of the head of the bursting streak, as was observed above the modifications for $y^+_{wire} \leq 10$. Hence, with the bubble-wire above $y^+_{wire} = 10$ the streaks appear to behave essentially the same for both the modifications and the flat plate.

3.1.3 SIDE-VIEW; VERTICAL BUBBLE-WIRE

Side-view visualizations were employed in an attempt to observe the streak lift-up and bursting phenomenon more completely. Figure 3.1.8 (a,b, and c) is a side-view sequence (with the bubble-wire located above a modification line) illustrating an inflow of fluid followed by the development and lift-up of a streak. Figure 3.1.8 (a, b, and c) are schematics of actual side-view pictures where the bubble lines have been traced to clarify the behavior. The original pictures were very bright at the bottom, due to light reflection by the modifications, yielding poor contrast which would have led to poor reproductions. In figure 3.1.8a ($t^+ = 0$) an inflow of fluid is indicated by the bulge in the bubble lines at the intersection of locations A and B. Offen (1975) has suggested that such inflows interact with a transverse vortex of "relative" backflow along the wall, termed a recirculation cell, to lift a streak from the flat plate (note that reverse

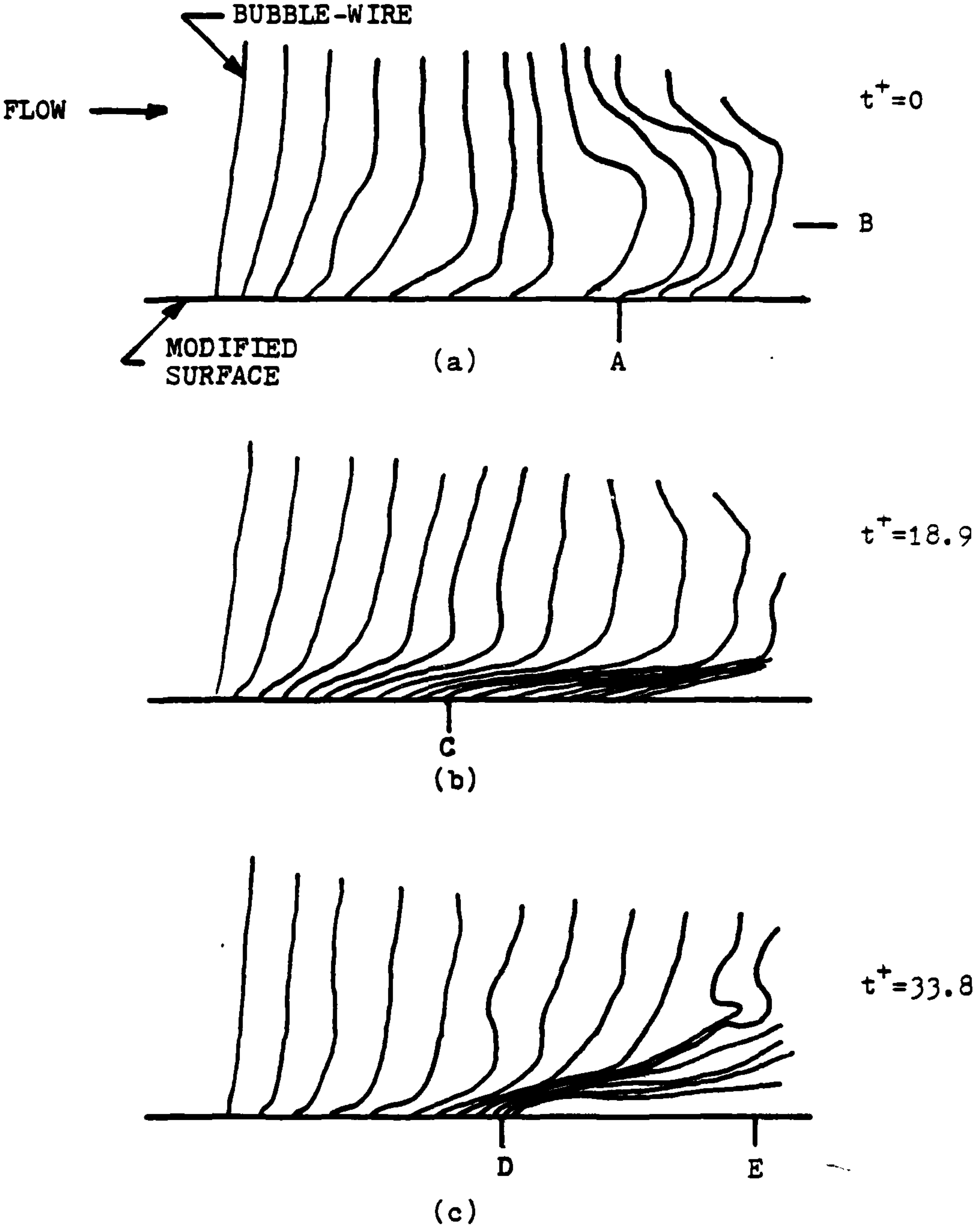

Figure 3.1.8. Schematic of side-view visualization showing inflow and streak development above a modification line. Flow left to right. $Re_{\Theta} \approx 1400$ and $f_b = 120$ Hz. (a) Inflow, (b) New streak formation, (c) Streak lift-up and propagation downstream.

flow is only implied relative to the local mean velocity, and that, reverse flow is not observed during stationary studies). Figures 3.1.8b, which occurs at $t^+ = 18.9$, shows a low speed region (i.e. a streak) forming over the top of a line at location C. Figure 3.1.8c ($t^+ = 33.8$) shows the same low speed streak region beginning to eject away from the surface and propagate downstream at location D. Note also what appears to be the formation of a transverse-like vortex in the outer flow above point E.

In side-views above both a flat plate and the line modifications, streaks were observed to lift out into the boundary layer and eject fluid during both partial or complete bursting. At first the ejected fluid was observed to rise slightly into the boundary layer. Most of the time this outward motion of the ejected fluid would continue, with mixing and dispersion of the fluid occurring. However, occasionally the ejected fluid would be observed to move slowly back toward the plate, after the initial lift-up, and impact the flat plate or the modifications. This action is possibly due to the hair pin loop type vortex interaction as discussed by Smith (1982). Figure 3.1.9 indicates the above bursting process with the two subsequent paths of ejected fluid.

Streamwise vortices, identical to those discussed by Kim et al. (1971), were also observed to lift from both the flat plate and modified surfaces. A streamwise vortex at an outer position in the boundary layer ($y^+ \approx 100$-150) was often observed to move inward and interact with a streamwise vortex associated with the lifting fluid. Since the overall strength (circulation) of the inward moving streamwise vortex was generally in excess of that of the lifting fluid vortex, the resulting influence of

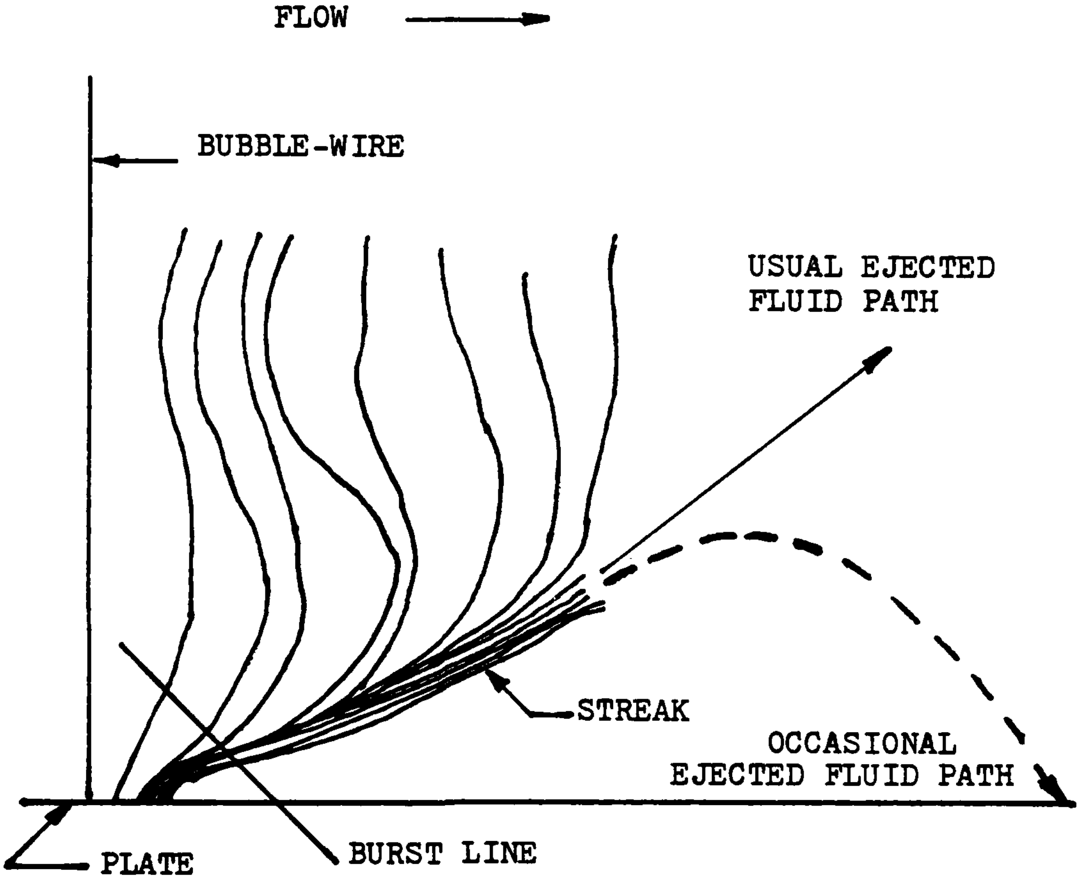

Figure 3.1.9. Schematic of loop-type burst showing ejected fluid paths.

the stronger vortex is often to cause the lifting vortex to move back towards the plate. During this interaction an apparent coalescence was often observed, causing the cumulative diameter of the vortex pair to rapidly expand, apparently conserving circulation. One must realize that the above visual observations result from the rapid three-dimensional distortion of a two-dimensional bubble sheet. Therefore, the true complexity of the pairing process may be overshadowed by the limitations of the visualization process.

In addition to the periods of violent bursting and fluid interaction, extended quiescent periods similar to those discussed by Kim et al. (1971), are observed above both the modifications and the flat plate. Because quiescent periods were observed both between and above the rods, the rods are not a source of continuous bursting behavior, but sustain periods of quiescent "build-up" between bursting events.

Summarizing, the side-views suggest that most of the characteristics observed above the line modifications appear essentially the same as those observed above an unmodified flat plate. Thus, the general characteristics of the boundary layer do not appear to be changed by the presence of the modifications, but perhaps they have become more structured by the presence of the lines.

3.2 STREAK SPACING RESULTS

3.2.1 DATA REDUCTION METHODS

To determine the spacing between streaks, streak counts were performed for each condition examined using a series of approximately sixty plan-view videographic prints. The videographic prints were obtained from plan-view recordings covering a time duration of $t^+ = 9720$. Each print was obtained $\Delta t^+ = 135$ (100 video frames) apart, roughly of the order of the bursting period for the flow conditions of the present study. The sixty print sequences yielded minimum and maximum streak counts of 240 and 700 over the range of conditions examined. At worst this provides a ±5.6% uncertainty in the mean streak spacing ($\overline{\lambda^+}$) with a 95% confidence level. Large fields-of-view ($\Delta z^+ = 550$-900) were employed, with the field-of-view of most data samples being $\Delta z^+ = 800$-900.

For the present study the streak identification procedure of Smith & Metzler (1983) was used, wherein streaks are defined to be regions marked by bright concentrations of bubbles, where the momentum flux of the low-speed region is less than or equal to 50% of the adjacent high-speed region momentum flux; this corresponds to a velocity ratio of $(u_{low}/u_{high}) \leq 70\%$. Generally, the velocity ratio is significantly less than 70%. Using the series of videographic prints, a transparency sheet marked with 60 horizontal spanwise axes offset in time (termed a streak count transparency) was used to locate the position of all streaks appearing in the sequence. To establish the streak locations, the transparency was overlaid on each print (with the corresponding axis aligned with the bubble-wire) and the location of each streak appearing in the print indicated by a tic mark. Applying this streak identification process to each successive print yielded the location of all identified streaks for the series of videographic prints. Note that so long as differentiation of high-speed fluid between close streak pairs could be made the streaks were marked individually.

In previous studies, empirical expressions for streak bursting time (T_B) have been based either upon inner variables ($f^+ = \frac{f\nu}{U_\tau^2}$; $T_B = 1/f$) or outer variables ($U\ T_B/\delta$). Employing conventional relationships from these prior studies, T_B for the present study is calculated as $t^+ = 200$ and $t^+ = 160$, based upon inner and outer variables, respectively. Hence, the sample rate of $\Delta t^+ = 135$ between data scenes is approximately of the order of T_B.

To establish scene magnification, calibration scenes were taken of a white metric scale at the same location as the bubble-wire. Hard copies of the calibration scenes were then used to establish the absolute scale for the streak count data scenes. A non-dimensional scale for measuring streak spacing in increments of $\lambda^+ = 10$ was then scribed; the friction velocity employed for the nondimensionalization was determined from parallel hot-film studies (see section 3.3).

3.2.2 HISTOGRAMS

During the present study, modified surfaces with $3.8 < h^+ < 4.5$ and $60 < s^+ < 160$ were examined. Video recordings were made with $y^+_{wire} = 5$, 10, 15, and 20 above both the modified surfaces and the adjacent flat plate test section. All studies were conducted with $Re_\Theta \cong 1400$. Spanwise low-speed streak distribution histograms were established by measuring the marked streak count transparencies with the scribed non-dimensional scales. Flat plate distribution histograms will be presented and discussed first. Distribution histograms from plate-1 for modification heights of $h^+ = 4.3$ with spacings of $s^+ = 71$ and 142 will then be presented to demonstrate the effects of the narrow and wide line spacing on streak spacing. Finally, distribution histograms from plate -2 will be presented ($h^+ = 3.8$, $s^+ = 111$).

3.2.2a FLAT PLATE HISTOGRAMS

Examples of several flat plate streak distributions with $y^+_{wire} = 5$ are shown in figures 3.2.1*, 3.2.2, and 3.2.3. A reproduction of a part of the streak count transparency used to develop each histogram is shown directly above each histogram. These will be referred to as streak counts for the remainder of this chapter. The horizontal lines on the streak counts represent the spanwise axis for each data scene in the sequence, offset in time by $\Delta t^+ = 135$. The vertical lines mark the location of each identified streak.

The following equations were used to calculate the statistical characteristics, which are listed to the right of each distribution histogram:

$$\sigma_\lambda = \left[\frac{1}{n-1} \sum_{i=1}^{n} (\lambda_i - \bar{\lambda})^2\right]^{1/2} \qquad \text{standard deviation} \qquad (1)$$

$$\psi_\lambda = \sigma_\lambda / \bar{\lambda} \qquad \text{coefficient of variation} \qquad (2)$$

$$S_\lambda = \frac{\frac{1}{n-1} \sum_{i=1}^{n} (\lambda_i - \bar{\lambda})^3}{\sigma_\lambda^3} \qquad \text{skewness} \qquad (3)$$

$$F_\lambda = \frac{\frac{1}{n-1} \sum_{i=1}^{n} (\lambda_i - \bar{\lambda})^4}{\sigma_\lambda^4} \qquad \text{flatness.} \qquad (4)$$

---

*Additional flow parameters not listed in the figure captions can be found by run number in table-1 and table G.1.

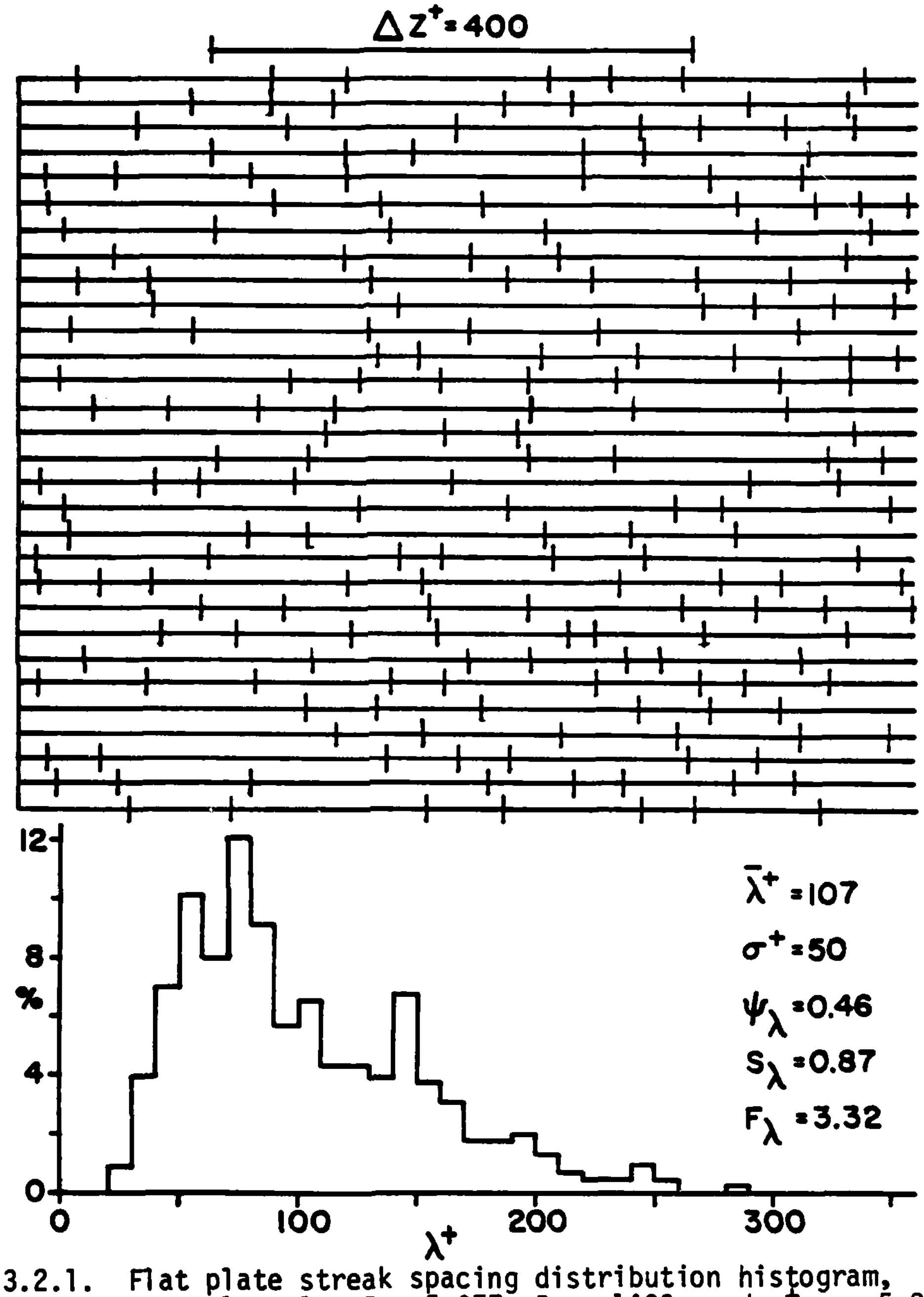

Figure 3.2.1. Flat plate streak spacing distribution histogram, test plate-1. Run 5-077, $Re_\Theta \approx 1400$, and $y^+_{wire} = 5.2$.

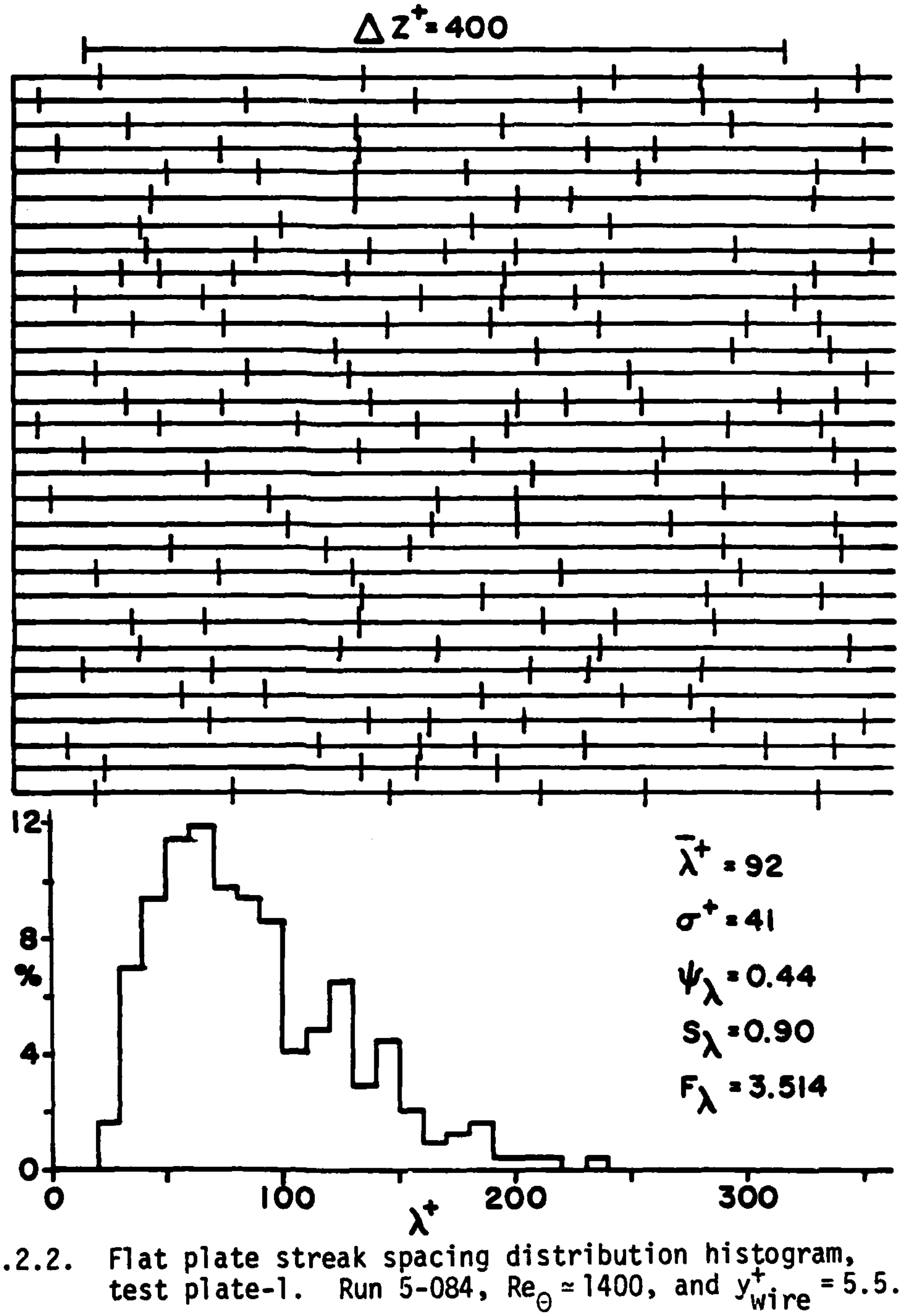

Figure 3.2.2. Flat plate streak spacing distribution histogram, test plate-1. Run 5-084, $Re_\Theta \simeq 1400$, and $y^+_{wire} = 5.5$.

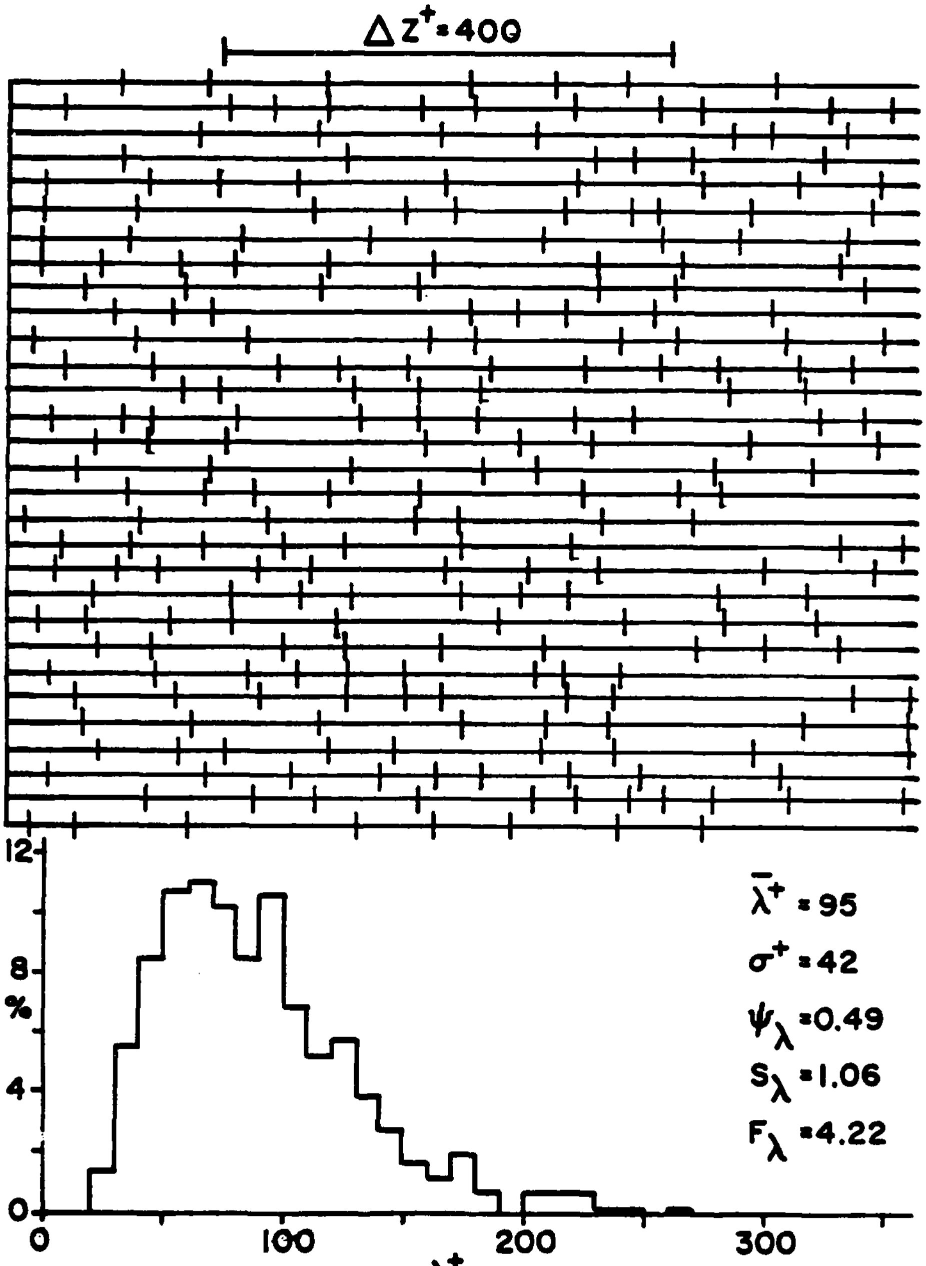

Figure 3.2.3. Flat plate streak spacing distribution histogram, test plate-2. Run 4-077, $Re_\Theta \approx 1500$, and $y^+_{wire} = 5.2$.

The studies that produced the data for figures 3.2.1 and 3.2.2 were conducted with plate-1, while figure 3.2.3 was obtained from a study with plate-2. The three histograms are essentially similar, skewed slightly to the left of mean, with the most probable streak spacing (λ^+_{mp}) approximately 20% less than the mean, as was observed by Smith and Metzler (1983). Note that the flatness is only slightly greater than that of a Gaussian distribution ($F = 3.0$) indicating the distributions are slightly peaked.

3.2.2b MODIFIED SURFACE, PLATE-1 ($s^+ = 71$ and $h^+ = 4.3$)

Figure 3.2.4 shows the most significant effect of the line modifications on streak spacing. The line height and spacing were $h^+ = 4.3$ and $s^+ = 71$ while the bubble-wire was located at $y^+_{wire} = 4.5$. Note that because of the strongly peaked behavior of the distribution the scale of the ordinate in figure 3.2.4 has been compressed relative to the other histograms presented in this section. Compared to figure 3.2.2, figure 3.2.4 demonstrates a radical peak at the mean ($\overline{\lambda^+} = 71$) which is coincident with the line spacing and is reflected by the high flatness value ($F_\lambda = 8.11$). There are very few streak spacings of $\lambda^+ > 150$. The ability of the lines to significantly influence the streak location is further demonstrated by the extreme ordering of the streaks in the streak count. Note also that very few streaks occur between lines. The low coefficient of variation ($\psi_\lambda = 0.32$) relative to comparable flat plate values of 0.46-0.49 further suggests that the lines have a stabilizing influence on the location of the streaks. Thus, it appears for this case that the lines behave as nucleation sites for streak formation.

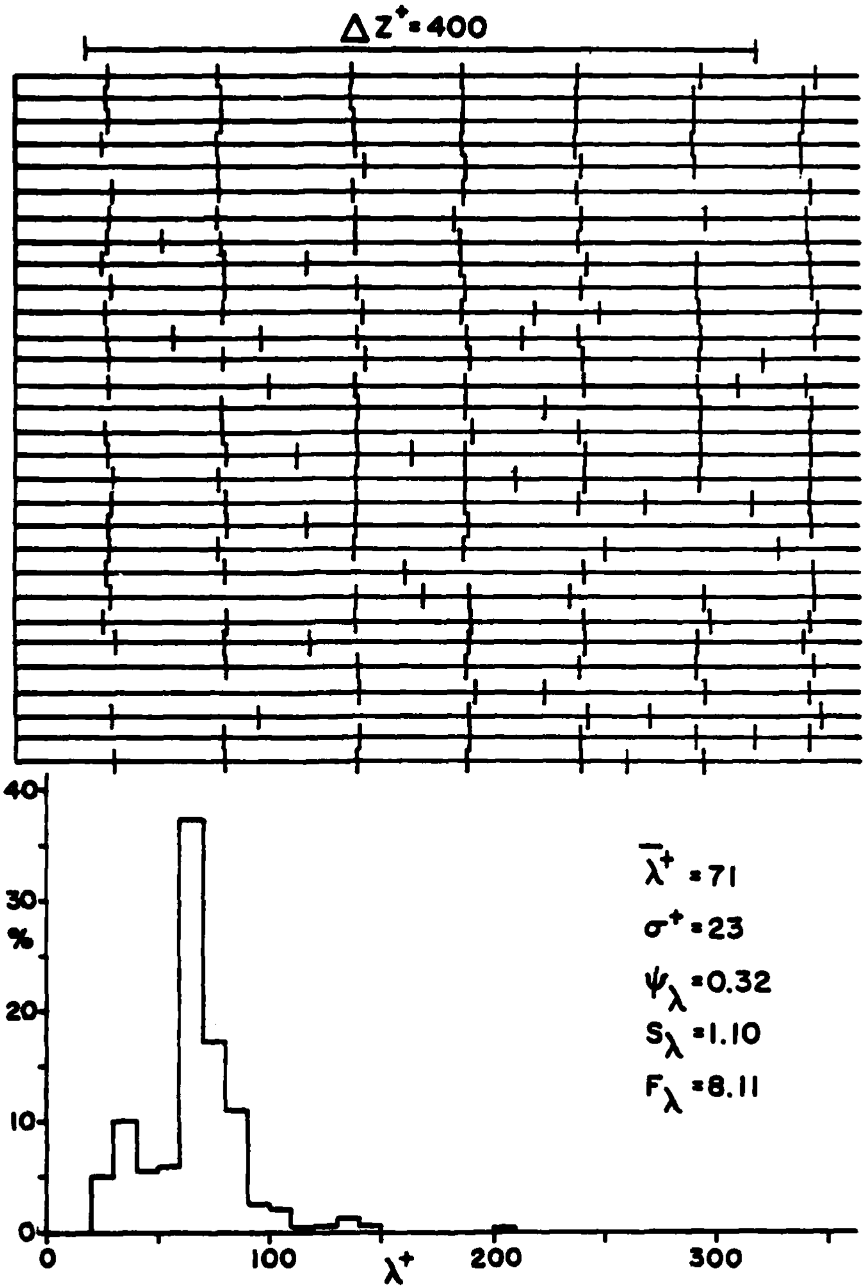

Figure 3.2.4. Modified surface streak spacing distribution histogram, test plate-1. Run 5-079, $Re_\Theta \approx 1400$, $h^+ = 4.3$, $s^+ = 71$, and $y^+_{wire} = 4.5$.

Figure 3.2.5 was compiled from data samples taken for the same conditions as above, ($s^+ = 71$, $h^+ = 4.3$) but with the bubble-wire at $y^+_{wire} = 9.8$. The streak distribution histogram obtained is quite different from that of figure 3.2.4. It is no longer peaked and has a much lower flatness value ($F_\lambda = 3.84$). The mean is higher than the line spacing, with the streak spacings more widely distributed about the mean, ($\overline{\lambda^+} = 85$) as the coefficient of variation ($\psi_\lambda = 0.48$) confirms. Hence, the distribution approaches that of a flat plate and so too do the associated statistics. The streak count indicates only a slight ordering of the streaks by the lines, significantly less ordering than that observed for $y^+_{wire} = 4.5$.

3.2.2c MODIFIED SURFACE, PLATE-1 ($s^+ = 142$ and $h^+ = 4.3$)

Comparison of the streak distribution and mean streak spacing in figure 3.2.6 ($y^+_{wire} = 9.3$, $h^+ = 4.3$, and $s^+ = 142$) with typical flat plate results (eg. figure 3.2.2) suggests that this line spacing also demonstrates a stabilizing effect on the location of the streaks. The streak count in figure 3.2.6 reveals that the lines do appear to create a weak ordering of the streaks; however, the majority of the distribution histogram is skewed toward $\lambda^+ < 100$ because of streaks that form between lines. The skewness and flatness values suggest that the distribution in figure 3.2.6 should be more positively skewed and significantly more peaked than the flat plate distribution in figure 3.2.2. However, figure 3.2.6 appears no more peaked than figure 3.2.2. The explanation for this apparent discrepancy is that the wider line spacings also cause spurious, very large streak spacings. Because of the finite sample size of the streak spacing data, this small increase in larger streak spacings can significantly bias

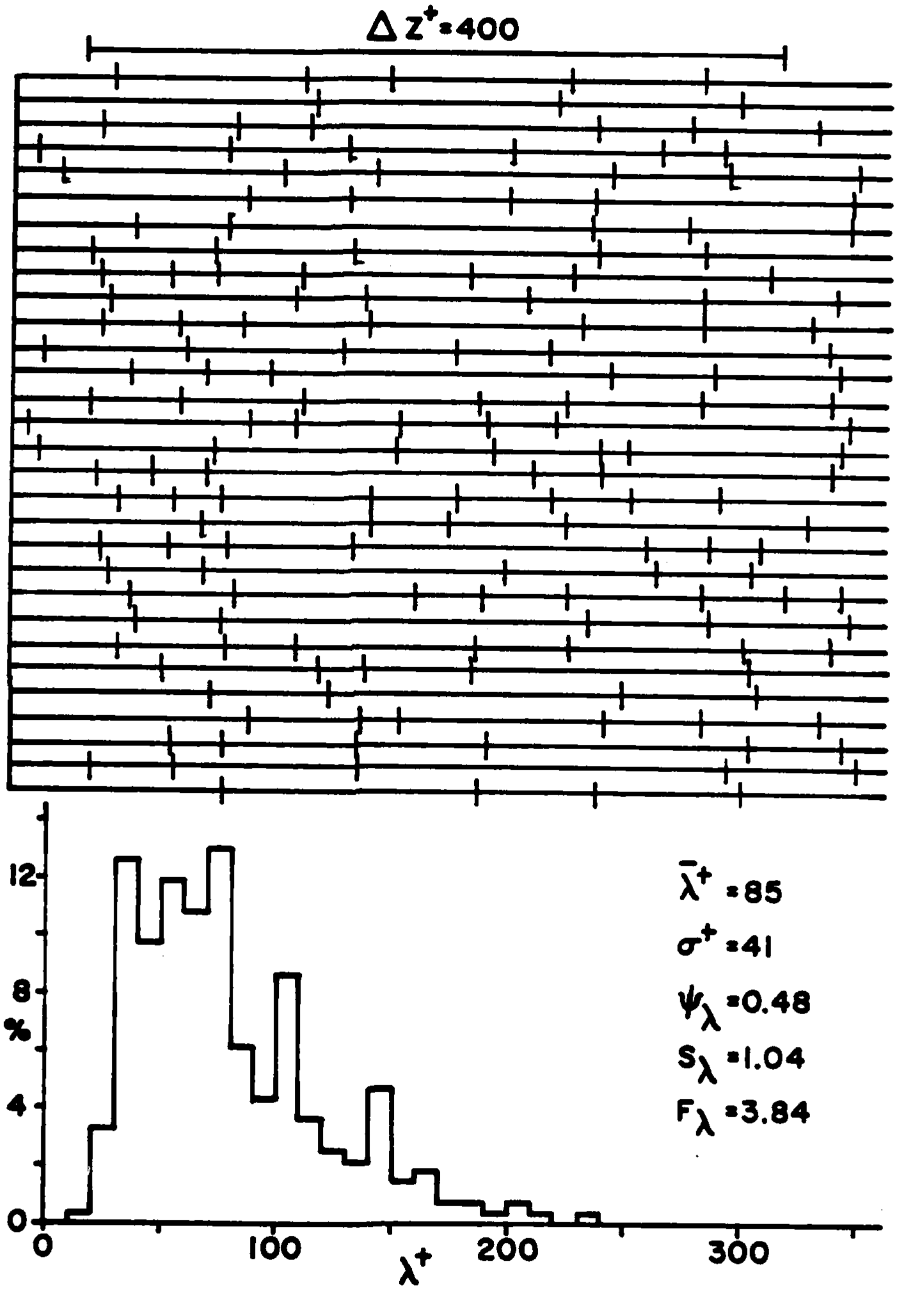

Figure 3.2.5. Modified surface streak spacing distribution histogram, test plate-1. Run 5-080, $Re_\Theta \simeq 1400$, $h^+ = 4.3$, $s^+ = 71$, and $y^+_{wire} = 9.8$.

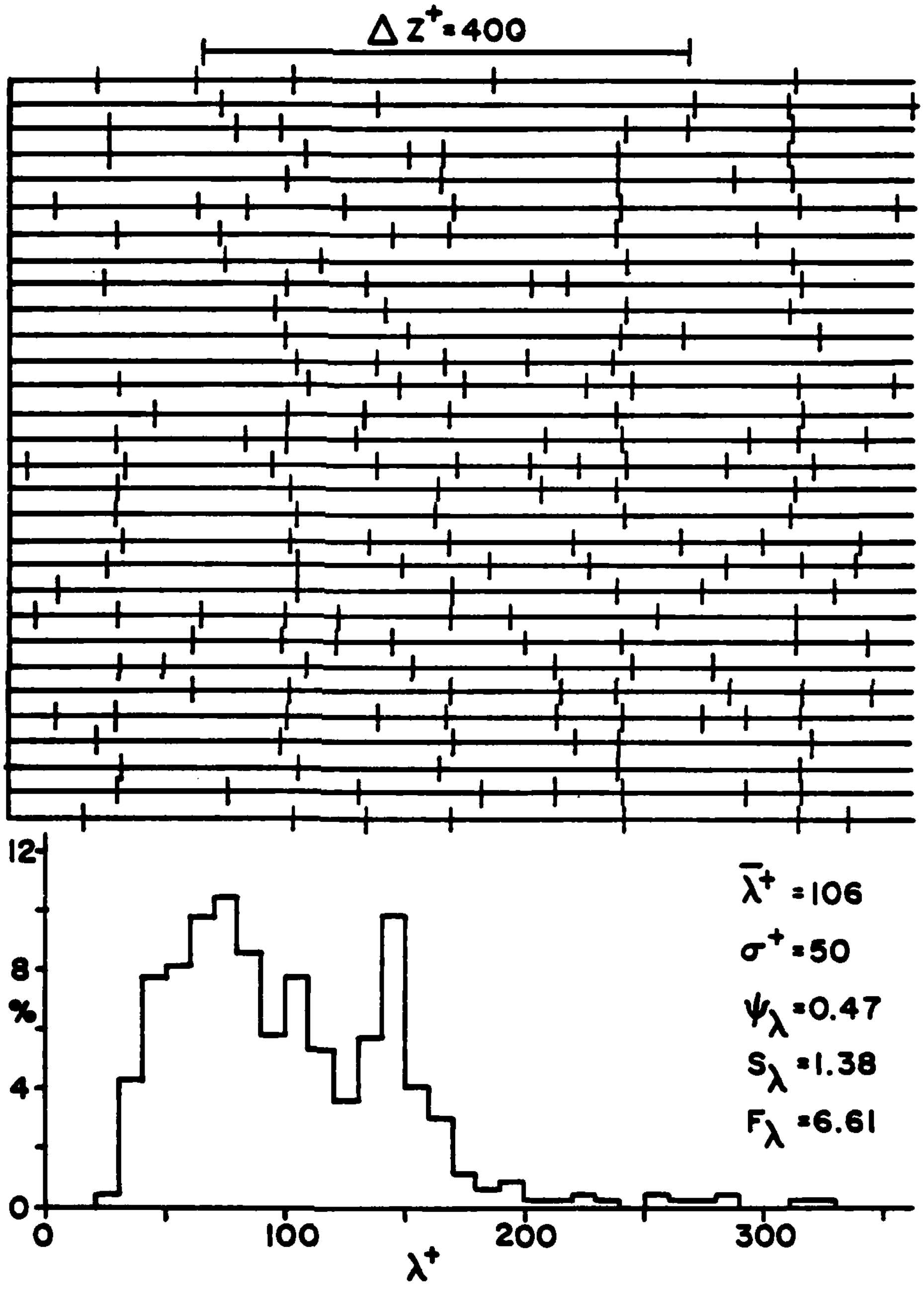

Figure 3.2.6. Modified surface streak spacing distribution histogram, test plate-1. Run 5-074, $Re_\Theta \simeq 1400$, $h^+ = 4.3$, $s^+ = 142$, and $y^+_{wire} = 9.3$.

the third and fourth moments about the mean. This point will be addressed in further detail in section 3.2.4. Finally, comparison of the streak counts of figures 3.2.6 and 3.2.5 suggests that at $y^+_{wire} \cong 9.5$ the line spacing of $s^+ = 142$ may have more influence on streak location than $s^+ = 71$.

3.2.2d MODIFIED SURFACE, PLATE-2 ($s^+ = 111$ and $h^+ = 3.8$)

Figure 3.2.7 was established from results obtained above the modified section of plate-2; the flat plate data presented in figure 3.2.3 reflect the comparable results obtained for the immediately adjacent unmodified flat plate. The bubble-wire was located at $y^+_{wire} = 4.0$ and the line height and spacing were $h^+ = 3.8$ and $s^+ = 111$. Observe that the distribution in figure 3.2.7 is very similar to that of figure 3.2.3. The mean,standard deviation, and coefficient of variation are also similar. However, the skewness and flatness suggest that the distribution histogram (figure 3.2.7) should be more positively skewed and more peaked than for a flat plate. Even though there appears to be a lack of coherence in the streak count of figure 3.2.7, it is believed that the lines have resulted in a slight increase in larger spacings ($\lambda^+ > 200$) which biases the skewness and flatness calculations (see section 3.2.4). The seeming lack of coherence in the streak count of figure 3.2.7 does not correlate with tests performed on plate-1. The reason for this lack of coherence is unclear; it is suggested that the formation of streaks may be history dependent or may possibly be dependent on the conditions at turbulent transition. Further study is definitely warranted.

Correlation with Metzler (1980) for streak spacing at various y^+ values above both 1) the lines, and 2) the flat plate behind the termination of the lines (plate-2) is not feasible because modification diameter,

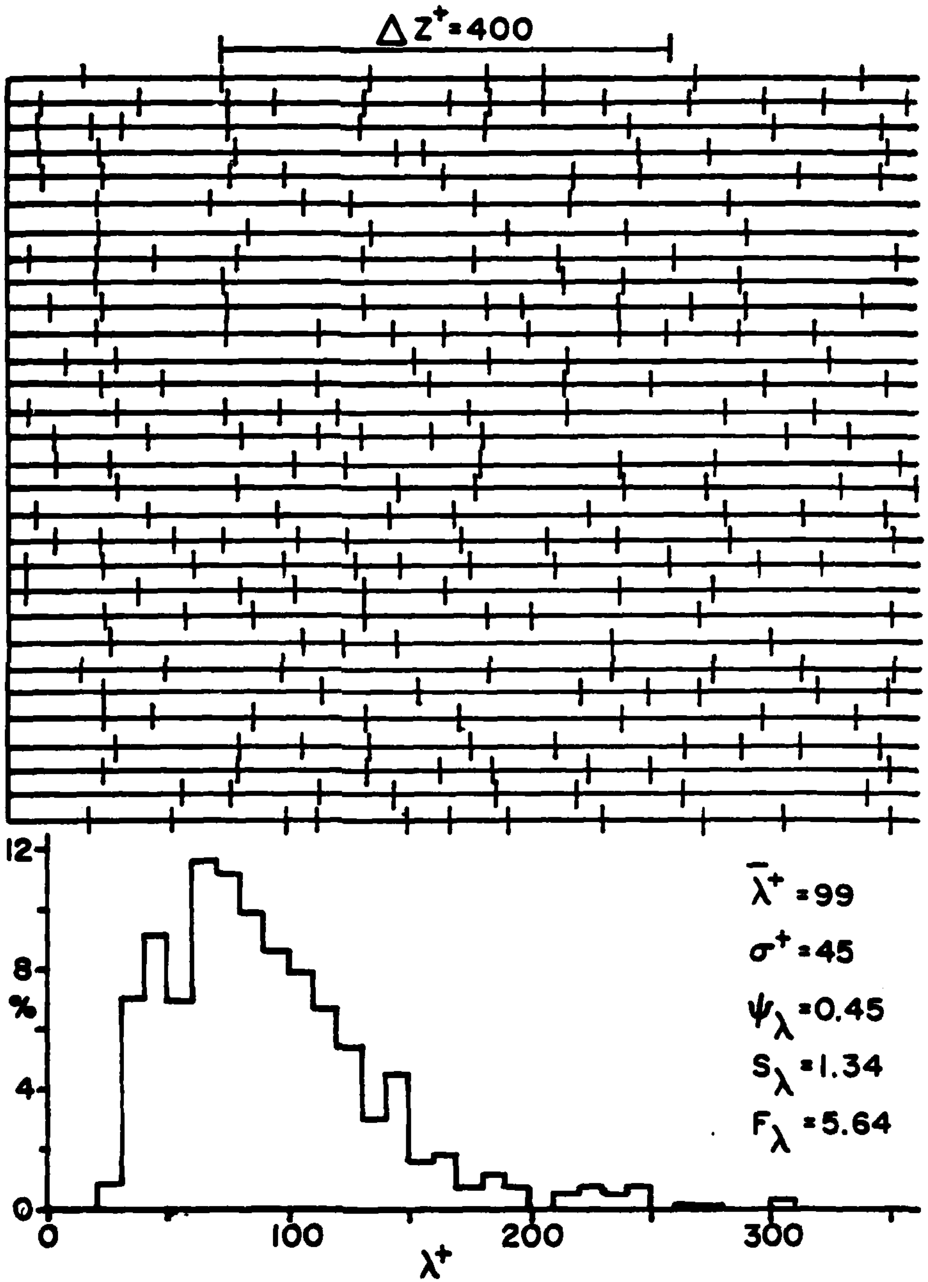

Figure 3.2.7. Modified surface streak spacing distribution histogram, test plate-2. Run 4-087, $Re_\Theta \simeq 1500$, $h^+ = 3.8$, $s^+ = 111$, and $y^+_{wire} = 4.0$.

length, and geometry of the leading-trailing edge of the modifications differed for both Metzler's study and the present study. The length of the lines on test plate-2 were $x^+ = 17{,}040$, which is significantly greater than the rod length of $x^+ = 3600$ employed in Metzler's study. Also, the rod height (h^+) of Metzler's study was twice that of the lines on plate-2. Thus, Metzler's rods extended from the viscous sublayer and introduced viscous wall effects farther out in the boundary layer than the present study. Another difference between the two studies is that the lines on plate-2 were attached to the surface so as to yield a smooth transition from plate to line (see chapter 2), whereas the rods of Metzler's study were blunt at both the leading and trailing edges, creating bluff body effects. These bluff body effects, like the scale of the modifications, may greatly affect the influence of the modifications on streak formation. Therefore, although the same general surface effects may be created by the lines of this sutdy and the rods of Metzler's study, the geometries are sufficiently different such that direct comparisons should be made with caution. Obviously, that streamwise surface modifications can have an effect on streak formation is clear from both studies. How the manifold factors such as modification diameter, length, and origin and end geometry of the lines affect the particulars of the behavior still needs further assessment.

To briefly summarize, modifications that traveled the entire length of the plate (plate-1) were observed to act as sites for low-speed streak development, whereas those that did not travel the length of the plate (plate-2) did not appear to have a noticeable effect on streak formation. The greatest observed influence of the lines on the location of streaks occurred when $s^+ = 71$, $h^+ = 4.3$, and $y^+_{wire} = 4.5$. It appears that at $y^+_{wire} \cong 9.5$ the influence of the lines on streak stabilization is decreased due to some form of streak interaction.

3.2.3 LOGNORMAL DISTRIBUTIONS

Nakagawa and Nezu (1981) were the first to suggest, based upon low Reynolds number ($Re_\Theta < 750$) channel flow studies, that the spanwise spacing of low-speed streaks may be represented by a lognormal probability density function. Smith and Metzler (1983) have subsequently confirmed this suggestion, demonstrating that low-speed streak spacing on a flat plate is lognormally distributed from $Re_\Theta = 710$ up to at least $Re_\Theta = 6000$.

The lognormal probability density function is given by:

$$P(\lambda) = \frac{\exp\left[-\frac{1}{2}\left(\frac{1}{\psi_o}\ln\frac{\lambda}{\lambda_o}\right)^2\right]}{\lambda\,\psi_o\sqrt{2\pi}} \qquad (5)$$

with

$$\lambda_o = \bar{\lambda}(1 + \psi_\lambda^2)^{-\frac{1}{2}} \qquad (6)$$

and

$$\psi_o = [\ln(1 + \psi_\lambda^2)]^{\frac{1}{2}}, \qquad (7)$$

where λ_o is the mean of the lognormal distribution and ψ_o is the standard deviation of log λ. For further details see appendix C, Hastings and Peacock (1975), or Aitchison and Brown (1957).

To examine the conformance of the present results to lognormality, lognormal probability density distributions were determined, using equations (5, 6, & 7) with the appropriate $\overline{\lambda}$ and ψ_λ values, and compared with several of the histograms obtained in the present sutdy (see figures 3.2.8 and 3.2.9).

Figure 3.2.8a, which is a representative flat plate distribution, demonstrates that both the streak spacing distribution and the corresponding lognormal distribution (the superposed curve) compare reasonably well, particularly considering the finite sample size (n = 243) of the histogram (the smallest sample size of the present study). Comparison of the lognormal distribution with the streak spacing distribution for $s^+ = 142$ (figure 3.2.8b) indicates that the lines have caused a modification of the streak spacing distribution, as the streak spacing distribution has been forced away from lognormality, as evidenced by the peak $\lambda^+ = 150$. Figure 3.2.9a ($y^+ = 4.5$, $h^+ = 4.3$, and $s^+ = 71$) indicates that the strong effect of the lines on streak formation very near the surface causes a strong variance of the streak spacing distribution from lognormal distribution. However, figure 3.2.9b ($y^+ = 9.8$, $h^+ = 4.3$, and $s^+ = 71$) indicates that farther above the surface the streak spacing distribution has relaxed back toward lognormality, demonstrating the diminshed influence of the modifications on streak spacing.

To further examine the lognormality of the streak spacing distributions for both flat plate and modified surfaces, the data was replotted on a lognormal probability graph of cumulative probability, $\alpha(\lambda)$, vs. $\log(\lambda/\overline{\lambda})$, where:

$$\alpha(\lambda) = \frac{\int_0^\lambda P(\lambda)d\lambda}{\int_0^\infty P(\lambda)d\lambda} . \qquad (8)$$

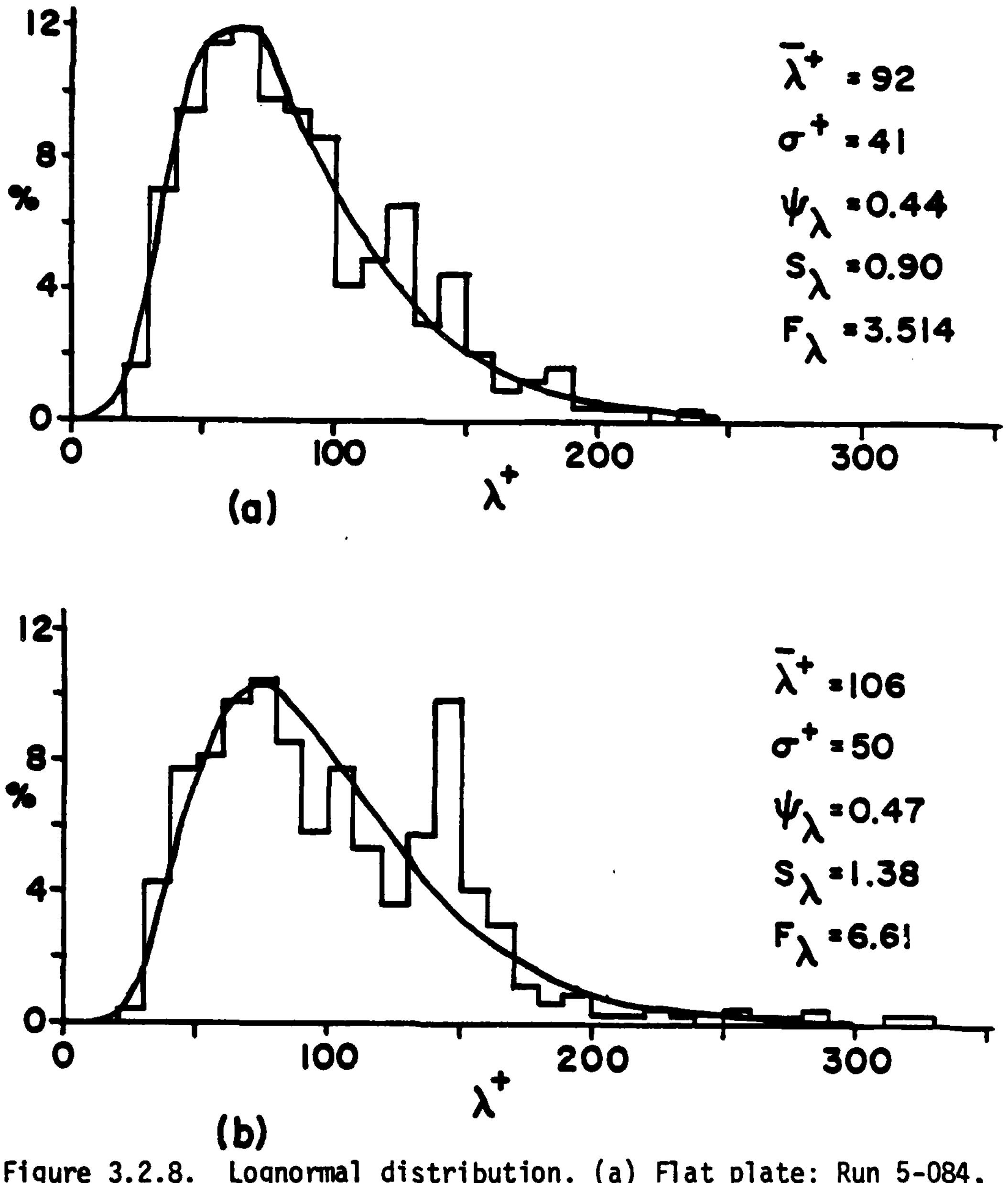

Figure 3.2.8. Lognormal distribution. (a) Flat plate: Run 5-084, $Re_\Theta \approx 1400$, and $y^+_{wire} = 5.5$, (b) Modified surface: Run 5-074, $Re_\Theta \approx 1400$, $h^+ = 4.3$, $s^+ = 142$, and $y^+_{wire} = 9.3$.

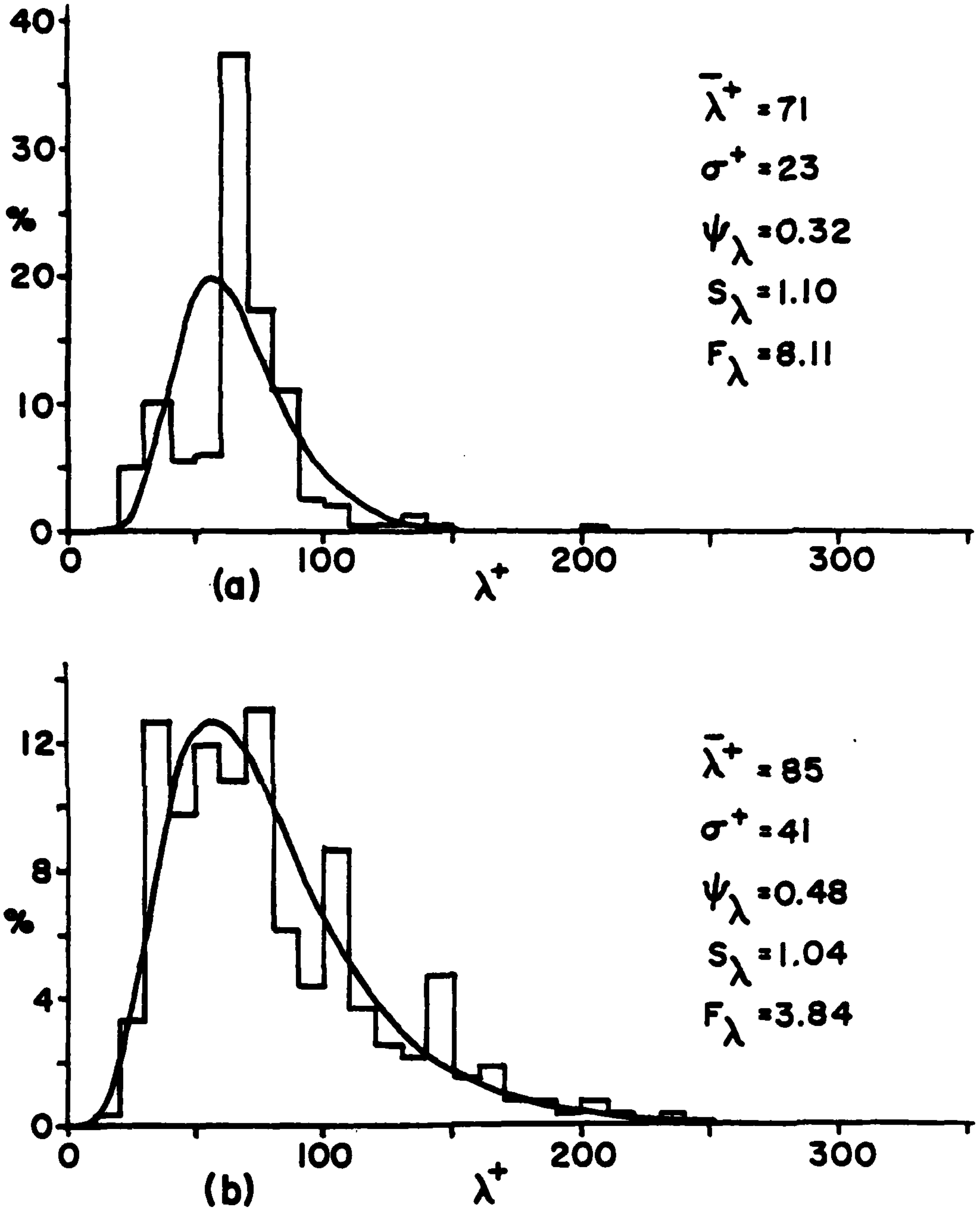

Figure 3.2.9. Lognormal distribution, modified surface. $Re_\Theta \approx 1400$, $h^+ = 4.3$, and $s^+ = 71$. (a) Run 5-079, $y^+_{wire} = 4.5$, (b) Run 5-080, $y^+_{wire} = 9.8$.

Figure 3.2.10 indicates all the flat plate streak spacing distributions of this study to be essentially lognormal (indicated by a straight line of positive slope on the probability graph). A true lognormal distribution for $\psi_\lambda = 0.482$ (the average value for the four flat plate studies) is shown for comparison, indicating reasonably good agreement. Figure 3.2.11 is a lognormal probability graph comparing several modified surface data samples with both a comparable flat plate data sample and true lognormal distributions for $\psi_\lambda = 0.479$ and $\psi_\lambda = 0.317$. The two modified distributions for $y^+ = 10$, $s^+ = 142$ and $y^+ = 10$, $s^+ = 71$, compare favorably with both the flat plate probability distribution and the true lognormal distribution for $\psi_\lambda = 0.479$ (the average value of the three distributions). The lognormal probability plot for $y^+ = 4.5$, $s^+ = 71$, suggests lognormality and weak agreement with the true lognormal distribution for $\psi_\lambda = 0.317$ (the calculated value for the experimentally determined distribution).

The positive skewness of the flat plate streak spacing distributions suggests that the streak formation phenomenon is low-end biased. The development of a lognormal distribution is indicative that the independent influences that affect the distribution about the mean have a multiplicative effect, rather than an additive effect as occurs for processes which are normally distributed. The presence of multiplicative influences causes variations which are proportional to the random variable, forcing the distribution of the variable to be low-end biased. The important point is that the streak distribution histograms for the modified surfaces are still reasonably consistent with a lognormal distribution, as evidenced by figure 3.2.11. Thus, it appears that while the lines improve the

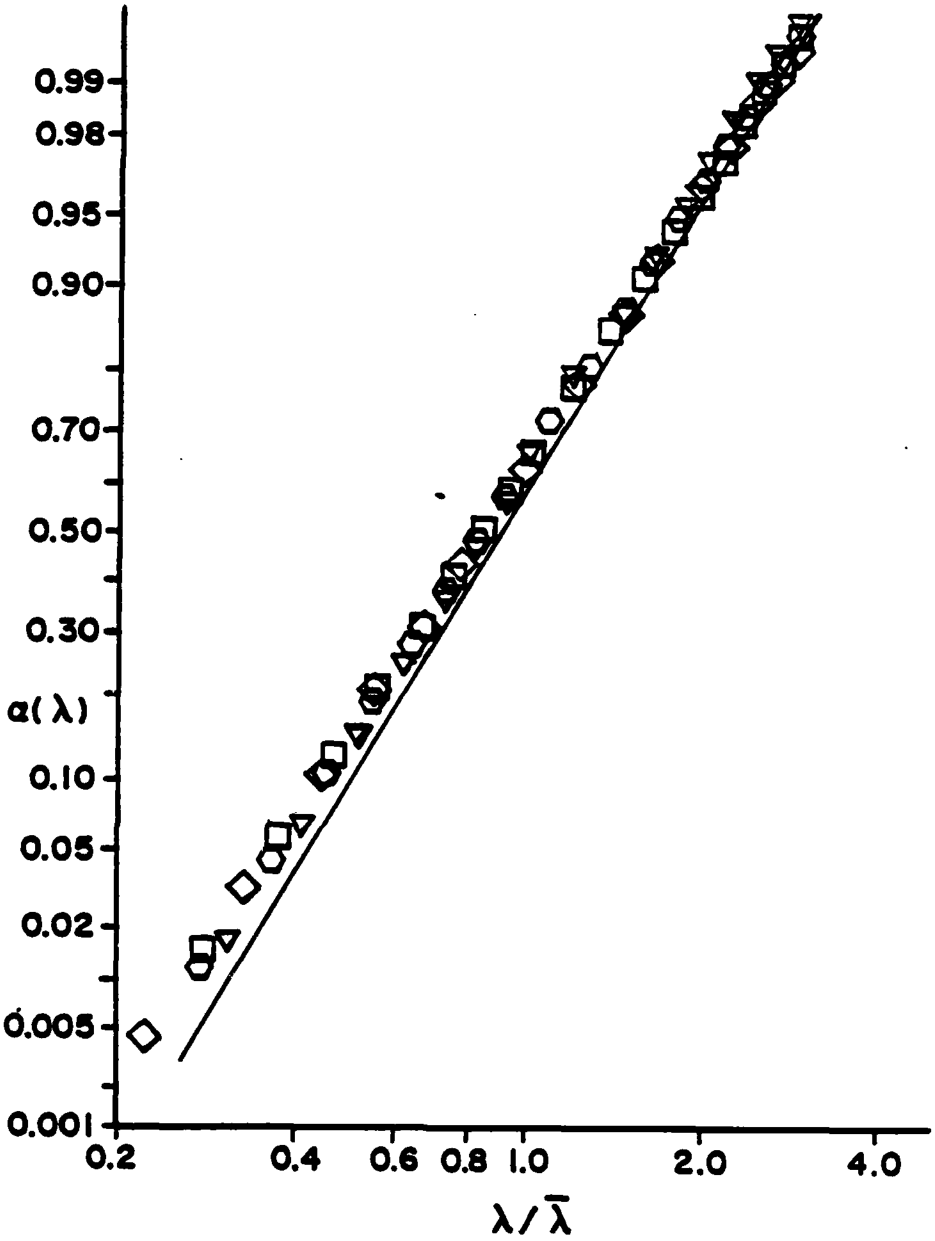

Figure 3.2.10. Lognormal probability graph, Flat plate. □, $Re_\Theta \approx 1150$, $y^+_{wire} = 5.2$, Run 4-063; ▽, $Re_\Theta \approx 1400$, $y^+_{wire} = 5.2$, Run 4-077; ○, $Re_\Theta \approx 1400$, $y^+_{wire} = 5.2$, Run 5-077; ◇, $Re_\Theta \approx 1400$, $y^+_{wire} = 5.5$, Run 5-084.

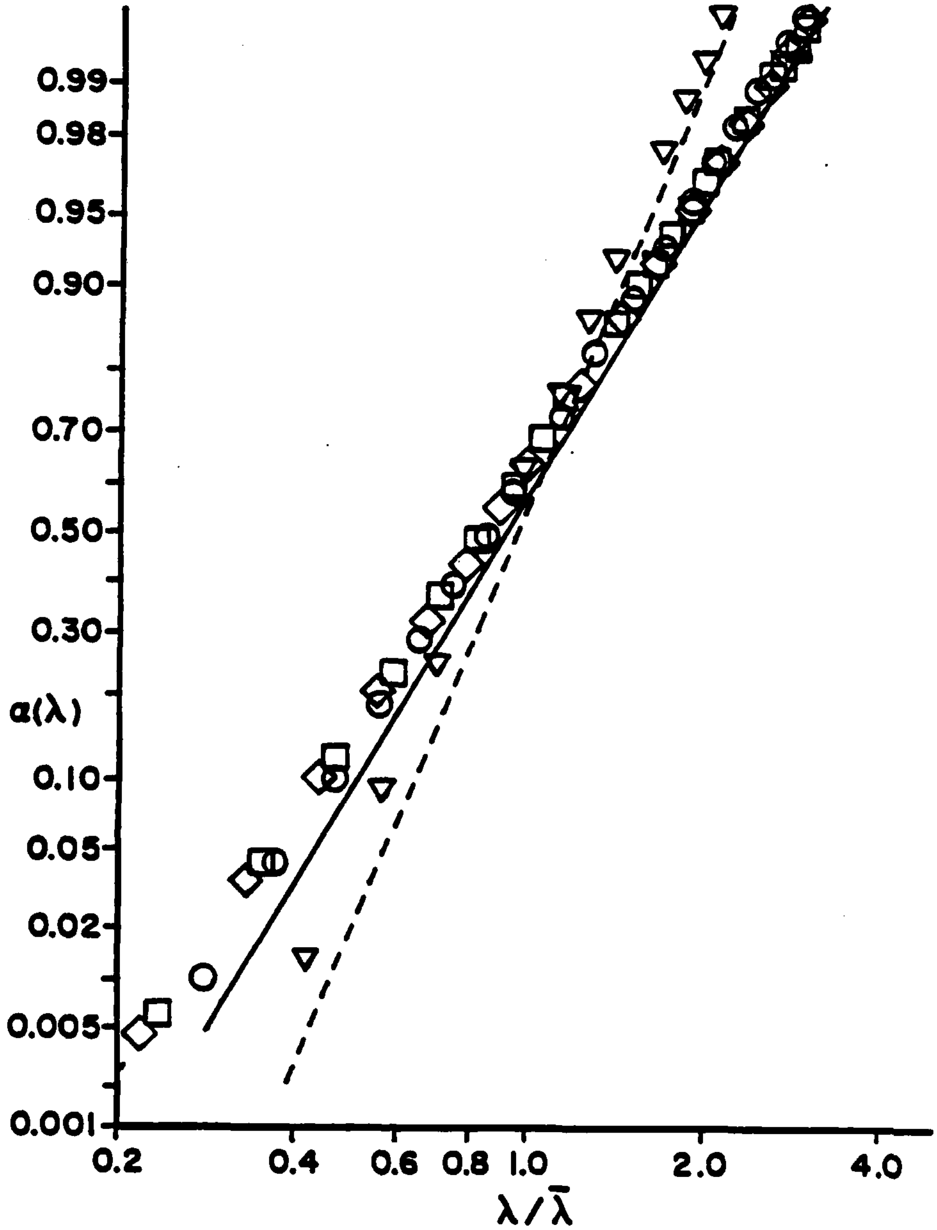

Figure 3.2.11. Lognormal probability graph comparing modified surfaces to a flat plate surface. $Re_\Theta \approx 1400$: ◇, Flat plate, $y^+_{wire} = 5.5$, Run 5-084; ▽, $y^+_{wire} = 4.5$, $s^+ = 71$, Run 5-079; □, $y^+_{wire} = 9.8$, $s^+ = 71$, Run 5-080; ○, $y^+_{wire} = 9.3$, $s^+ = 142$, Run 5-074; ——, True lognormal probability distribution for $\psi_\lambda = 0.479$; and ---, True lognormal probability distribution for $\psi_\lambda = 0.317$.

stability and organization of streaks for $y^+_{wire} = 5$, they do not totally change the behavior, but simply modify the "lognormal" behavior to be less dispersed.

3.2.4 STATISTICAL RESULTS

In order to statistically characterize the streak spacing distributions, the standard deviation, coefficient of variation, skewness, and flatness were determined using equations one through four as presented in section 3.2.2. The respective values for the data runs are tabulated in table-1 and indicated on each distribution shown in section 3.2.2 and 3.2.3 of this chapter.

First, consider the statistical characteristics determined for the flat plate studies. The mean streak spacing is in generally good agreement with the accepted value of $\overline{\lambda^+} \approx 100$. Positive skewness is suggested for all the flat plate profiles, $(0.87 < S_\lambda < 1.11)$ which is in good agreement with values obtained by Smith and Metzler (1983), as is the flatness range $3.51 < F_\lambda < 4.45$ for the present study. However, for all flat plate results the coefficient of variation ranged from 0.44 to 0.48, which is similar to values which were obtained by Smith and Metzler for $y^+_{wire} \cong 30$. Estimates for ψ_λ of 0.30-0.40 ($y^+ = 5$) by Schraub and Kline (1965), 0.40 ($y^+ = 2\text{-}7$) by Gupta et al. (1971), and the range of 0.34-0.40 ($y^+ = 5$) by Smith and Metzler (1983) are all less than the values of the present study. This apparent discrepancy is not understood, but may be a result of the use of a consistently wider field of view for the present study, which might have resulted in inclusion of wider streak spacings which were not detected in previous studies.

Table-1: Flow Parameters and Streak Spacing Statistics From Visualization Studies

Run	x(m)	y^+_{wire}	h^+	s^+	U(m/s)	$\nu(\frac{m^2}{s})(*10^{-6})$	$\overline{\lambda^+}$	σ_λ	ψ_λ	S_λ	F_λ	Plate
4-015	0.81	5.2	FP		0.23	0.932	106	50.8	0.48	1.11	4.43	2
4-023	0.81	5.2	FP		0.23	0.932	100	45.4	0.45	1.06	4.45	2
4-053	1.52	9.0	3.8	111	0.23	0.932	110	54.2	0.49	1.25	4.91	2
4-063	1.52	5.2	FP		0.23	0.932	105	51.1	0.48	1.10	4.08	2
4.077	2.03	5.2	FP		0.25	0.932	95	41.9	0.44	1.06	4.22	2
4.087	2.03	4.0	3.8	111	0.25	0.932	99	44.9	0.45	1.34	5.64	2
5-001	2.09	5.2	FP		0.25	0.932	103	47.3	0.46	0.94	3.60	2
5-074	2.06	9.3	4.3	142	0.26	0.875	106	49.5	0.47	1.38	6.61	1
5-077	2.06	5.2	FP		0.26	0.875	107	49.6	0.46	0.87	3.32	1
5-079	2.06	4.5	4.3	71	0.26	0.865	71	22.5	0.32	1.10	8.11	1
5-080	2.06	9.8	4.3	71	0.26	0.865	85	41.0	0.48	1.04	3.84	1
5-084	2.06	5.5	FP		0.26	0.865	92	40.6	0.44	0.90	3.51	1
							(90)	(44.0)	(0.48)	(1.62)	(7.22)	

Comparison of the modified surface statistics with flat plate statistics suggests that only the cases for $y^+_{wire} = 4.5$, $s^+ = 71$ and $y^+_{wire} = 10$, $s^+ = 71$ had a dramatic effect on the mean streak spacing. The standard deviation also suggests that the lines had a significant ordering effect on the streak spacing, which is further reflected by the reduced coefficient of variation for $y^+_{wire} = 4.5$ and $s^+ = 71$.

For $s^+ > 100$, the skewness values suggest that the distributions should be more positively skewed about the mean than for the flat plate distributions. Also, except for the case $s^+ = 71$, $y^+_{wire} = 9.8$ (which was observed to be less peaked in figure 3.2.5), there is a clear correlation between line spacing and an increased flatness value (more peaked distribution).

However, one must be careful when calculating higher moment statistics from limited sample length data. These moments are particularly sensitive to the contributions of high end values, only a few of which can severely bias the subsequent "averaged" statistics. To exemplify how a few large streak spacings can alter the statistics consider run 5-084 in table-1. The addition of one streak spacing ($\lambda^+ = 340$) to the streak spacing distribution ($n = 244$) has a drastic effect on the skewness and flatness values. The difference in statistical values caused by the addition of this one data point are shown in parentheses in table-1. The addition of this data point caused the skewness to jump from 0.90 to 1.62, the flatness to jump from 3.51 to 7.22, and the coefficient of variation from 0.44 to 0.48. Hence for a line spacing of $s^+ > 100$ a significant bias in the skewness and flatness calculations, and to some degree the coefficient of variation, can occur due to spurious large streak spacings.

The effect of all line spacings on mean streak spacing, including those data for which only mean streak spacing was evaluated, (see appendix G, Table G.1 for data) is shown in figure 3.2.12. Figure 3.2.12a, determined for $y^+_{wire} \cong 5$, demonstrates a positive relationship between line spacing and mean streak spacing, suggesting that the modifications do have a stabilizing and ordering influence on the mean streak spacing. Figure 3.2.12b demonstrates the lines still have a positive effect on observed streak spacing out to $y^+_{wire} \approx 10$,but the effect is diminished since the mean streak spacing is less regular and has relaxed back toward that for an unmodified flat plate.

3.3 HOT-FILM ANEMOMETRY RESULTS

The following section presents and discusses the results of the hot-film anemometer studies. This section is subdivided into four parts: 1) mean velocity profiles, 2) turbulence intensity profiles, 3) spanwise profiles, and 4) boundary layer parameters. The method of probe zero-referencing, discussed in appendix A, helped provide accuracy in measurements down to $y^+ \cong 5$, where wall effects on the probe become significant.

3.3.1 MEAN VELOCITY PROFILES

Data samples of 65 ± 5 points were taken to provide smooth boundary layer velocity profiles. The mean velocity data were first plotted on a Clauser-type cross-plot, (see Caluser 1956) as shown in figure 3.3.1, to estimate the skin friction coefficient (C_f). This method is based on the empirically accepted law-of-the-wall equation:

$$u/U_\tau = 2.44 \ln y^+ + 4.9. \qquad (9)$$

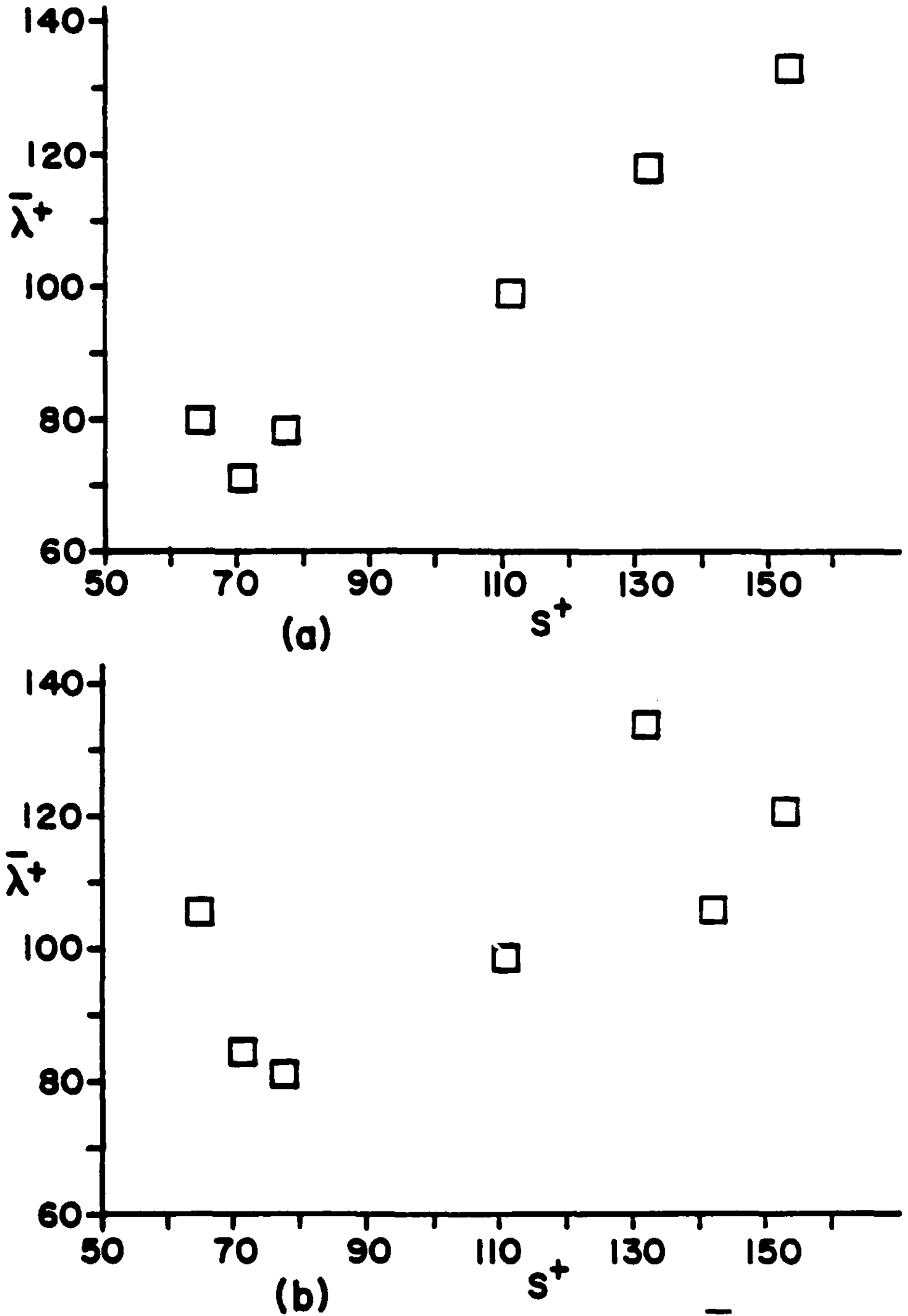

Figure 3.2.12. Graph of mean streak spacing ($\bar{\lambda}^+$) vs. rod spacing (s^+): (a) $y^+_{wire} \simeq 5$, (b) $y^+_{wire} \simeq 10$.

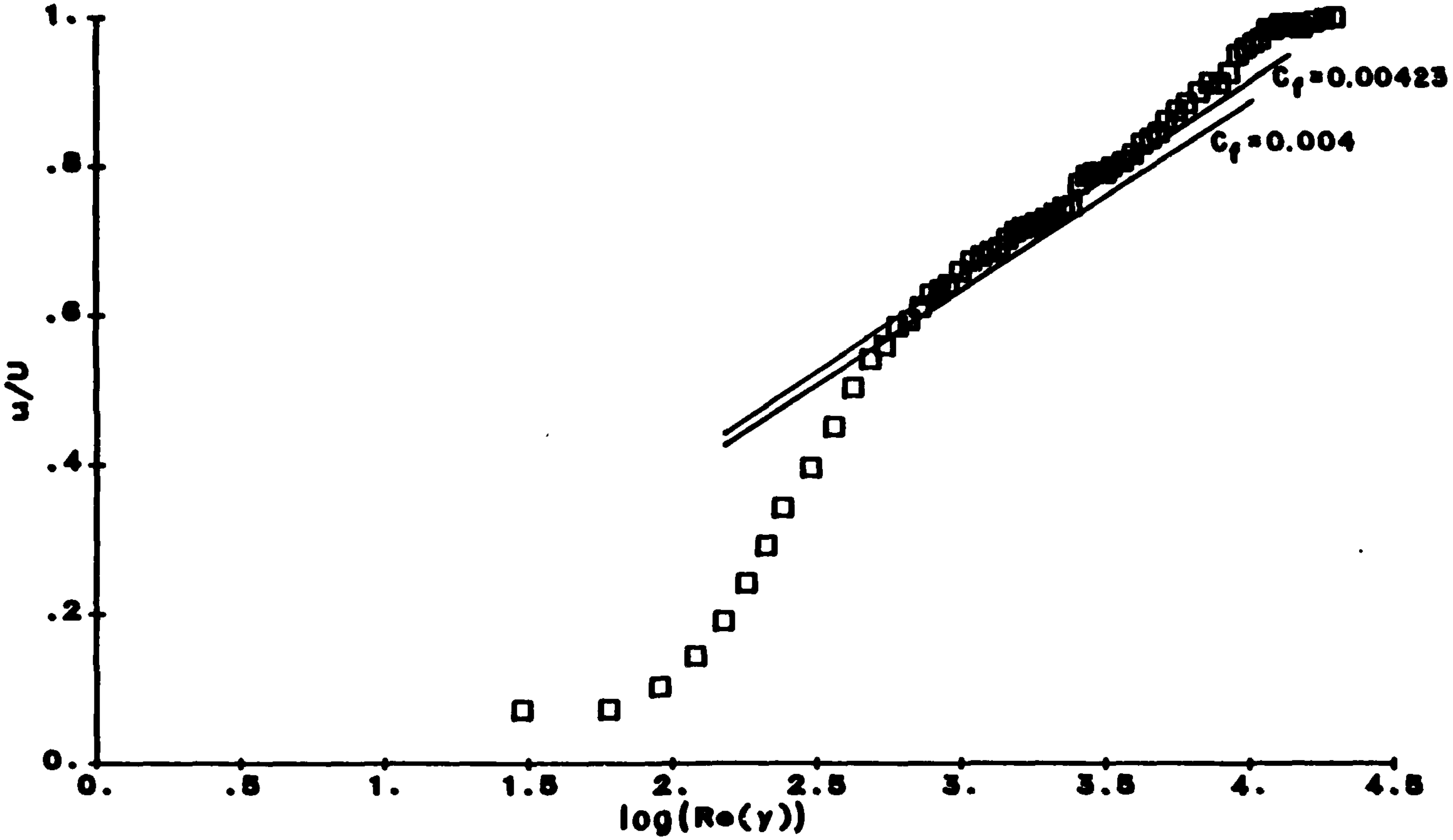

Figure 3.3.1. Law-of-the-wall Clauser cross-plot. Plate-1, Flat plate, Data file 20, $Re_{\Theta}=1297$.

Substituting $U_\tau/U = \sqrt{C_f/2}$ and rearranging equation (9) yields

$$u/U = C[2.44 \ln (yUC/\nu) + 4.9] \qquad (10)$$

where $C = \sqrt{C_f/2}$. To determine the appropriate value of C_f for a set of experimental data, the values of u/U are plotted vs. y, and compared with the result of equation (10) for various values of C_f. The proper C_f value for the data is that which makes equation (10) match the data in the logarithmic region.

Purtell et al. (1981) determined skin friction coefficients by calculation of $d\Theta/dx$ from measured velocity profiles, and compared these with the skin friction coefficients determined using the law-of-the-wall Clauser cross-plot method. He found general agreement between the two methods to within ±5%. This suggests that the Clauser cross-plot is an appropriate method for the estimation of the skin friction coefficient. White (1974) suggests that the following explicit equation for C_f, for turbulent flow over a flat plate, is accurate to ±2% for the entire turbulent range:

$$C_f = \frac{0.455}{\ln^2(0.06\, Re_x)} . \qquad (11)$$

Equation (11) yields $C_f = 0.00411$ for the data of figure 3.3.1*, which is within 2.8% of the value determined by the Clauser cross-plot ($C_f = 0.00423$). Other Clauser cross-plots are shown in appendix D.

---

*Additional flow parameters for hot-film data plots are indicated by data file in table-2.

Employing the established C_f values, the mean velocity data was normalized on inner variables and plotted in law-of-the-wall form. Plots were constructed for measurements 1) between two lines, and 2) above a line for the modified test section, and 3) above the juxtaposed section of flat plate. To provide further insight, plots of velocity profiles obtained above a modifying line were established using two different references: 1) with $y^+ = 0$ referenced to the top of the line (figures 3.3.2 and 3.3.4) and 2) with $y^+ = 0$ referenced to the plate surface (figures 3.3.3 and 3.3.5). Figure 3.3.2 ($s^+ = 142$, $h^+ = 4.3$) and figure 3.3.4 ($s^+ = 71$, $h^+ = 4.3$) might at first suggest the lines have little effect on the characteristic law-of-the-wall profile, as the data above and between modifying lines plot very closely to the flat plate profile. However, figures 3.3.3 and 3.3.5, which reference all the velocities relative to the flat plate, show that the lines do create a low-speed zone which appears to strongly influence the law-of-the-wall plot below $y^+ = 25$-30. This illustrates how the wakes of the lines can affect streak development in that region. Unlike three-dimensional surface roughness, which shifts the entire law-of-the-wall plot down and to the right (see White, p. 490), the law-of-the-wall plots for $y^+ > 30$ appear to be unchanged by the streamwise surface modifications. Also, if the modifications affected the regions of the boundary layer for $y^+ > 40$, the empirical flatplate law-of-the-wall equation (9) would not match the data in the linear region of the Clauser cross-plots. The Clauser cross-plots in Appendix D suggest that the characteristics of the outer boundary layer region have not been affected by the streamwise surface modifications.

In summary, the streamwise lines appear to present sites for low-speed streak formation, but they only appear to cause an alteration of the general boundary layer profile in the near wall region below $y^+ = 25$-30.

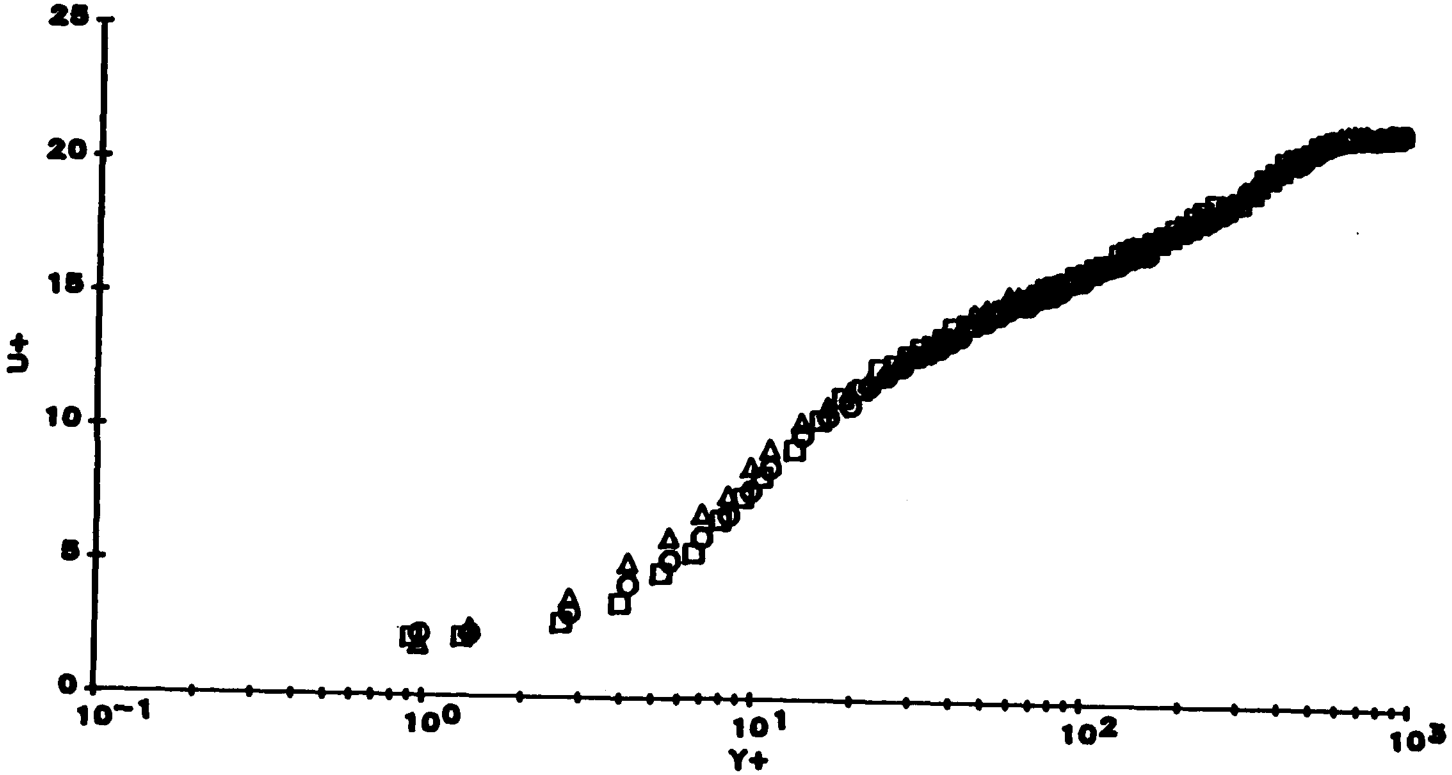

Figure 3.3.2. Law-of-the-wall plot, plate-1. $Re_\Theta \simeq 1350$, $h^+ = 4.3$, and $s^+ = 142$: □, Flat plate, Data file 20; ○, Between two lines, Data file 21; △, Above a line with $y^+ = 0$ referenced to the top of the line, Data file 22.

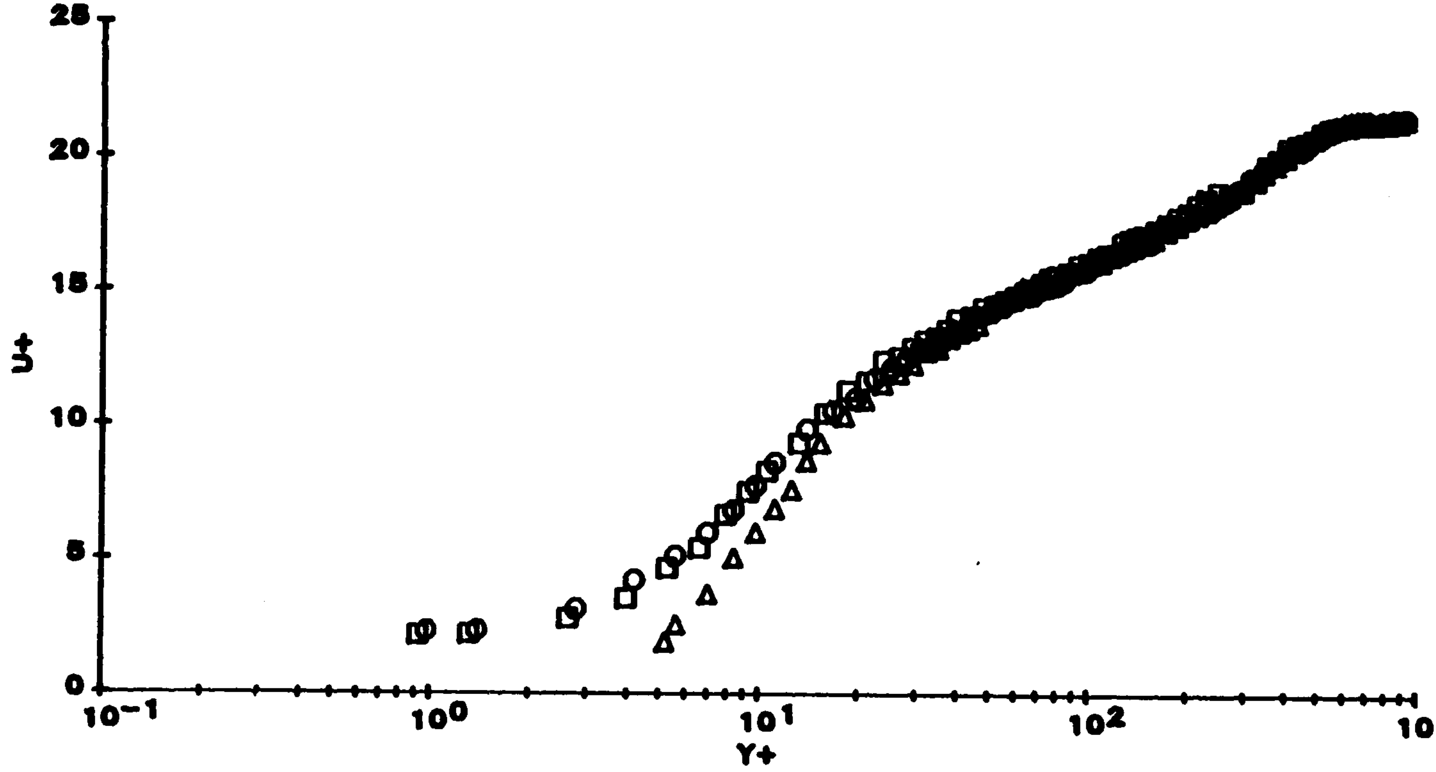

Figure 3.3.3. Law-of-the-wall plot, plate-1. $Re_\Theta \approx 1350$, $h^+ = 4.3$, and $s^+ = 142$: □, Flat plate, Date file 20; ○, Between two lines, Data file 21; △, Above a line with $y^+ = 0$ referenced to the flat plate, Data file 22.

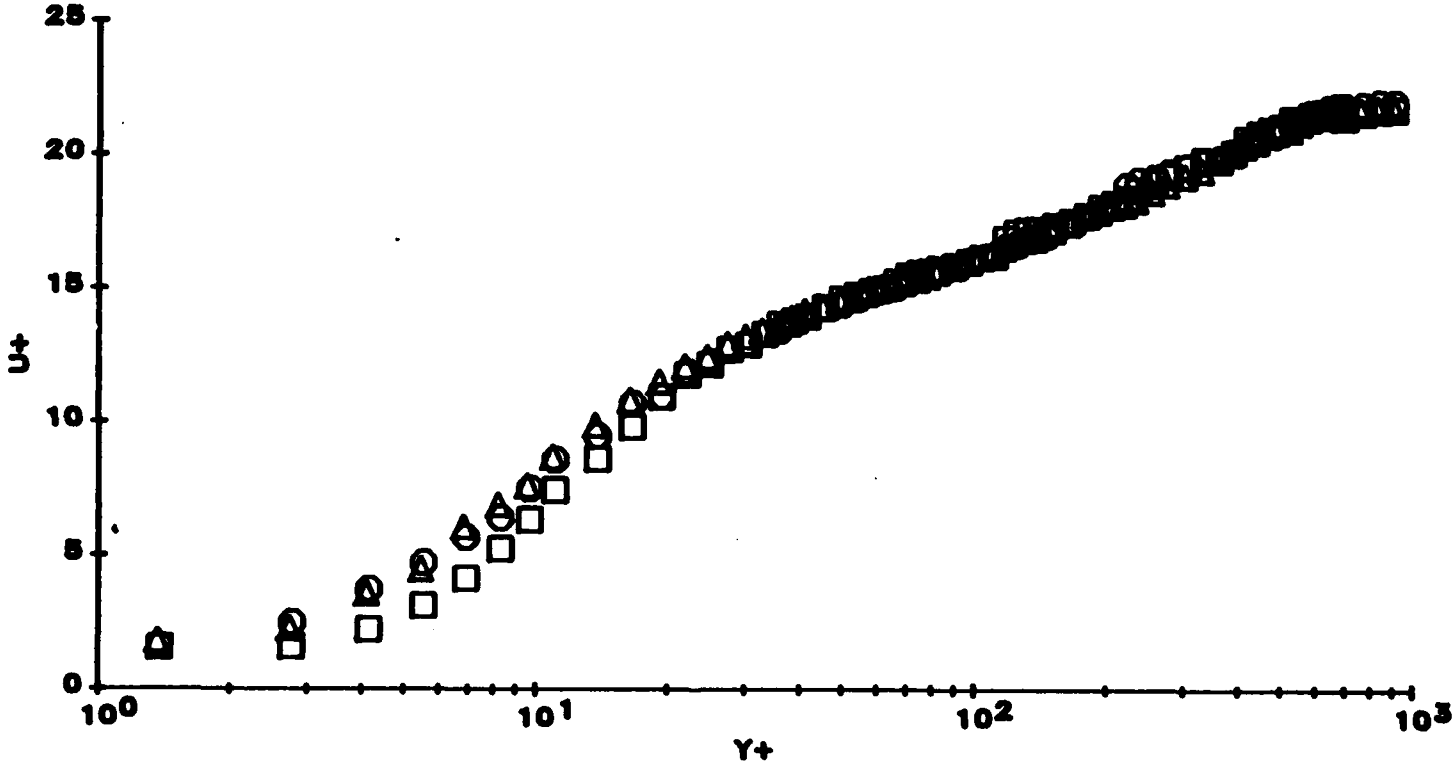

Figure 3.3.4. Law-of-the-wall plot, plate-1. $Re_{\theta} \approx 1450$, $h^+ = 4.3$, and $s^+ = 71$: □, Flat plate, Data file 23; ○, Between two lines, Data file 24; △, Above a line with $y^+ = 0$ referenced to the top of the line, Data file 25.

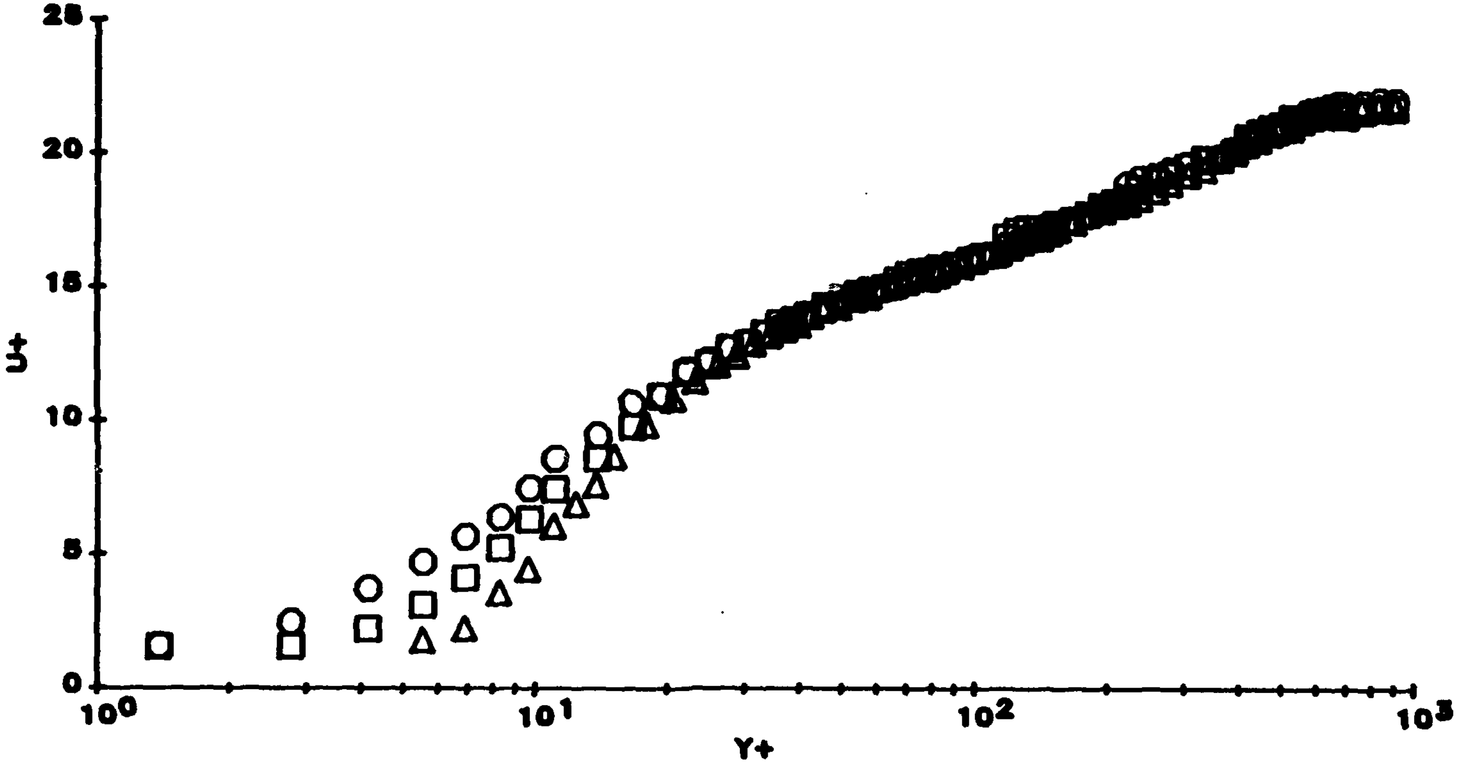

Figure 3.3.5. Law-of-the-wall plot, plate-1. $Re_\Theta \approx 1450$, $h^+ = 4.3$, and $s^+ = 71$: □, Flat plate, Data file 23; ○, Between two lines, Data file 24; △, Above a line with $y^+ = 0$ referenced to the flat plate, Data file 25.

AD-A136 296 THE EFFECTS OF CYLINDRICAL SURFACE MODIFICATIONS ON 2/2
TURBULENT BOUNDARY LA..(U) LEHIGH UNIV BETHLEHEM PA
DEPT OF MECHANICAL ENGINEERING AND M..
UNCLASSIFIED J B JOHANSEN ET AL. APR 83 AFOSR-TR-83-1217 F/G 20/4 NL

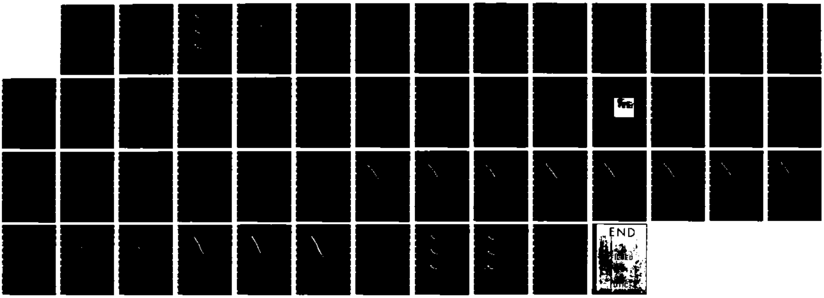

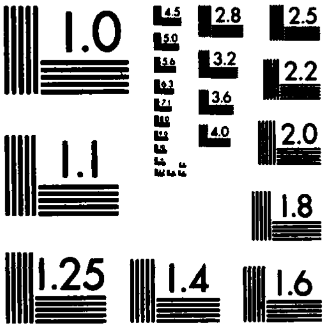
1.0
4.5
5.0
5.6
6.3
7.1
8.0
2.8
3.2
3.6
4.0
2.5
2.2
2.0
1.1
1.8
1.25
1.4
1.6

3.3.2 TURBULENCE INTENSITY PROFILES

Turbulence intensity profiles above a modifying line, between two lines, and above the flat plate were measured to determine if the presence of the lines has a damping or amplifying effect on turbulence intensity. Figure 3.3.6 suggests that the lines have little effect on the turbulence intensity profiles. Note that $y^+ = 0$ was referenced to the top of the line in the bottom plot of figure 3.3.6. All three (top, middle, and bottom) turbulence intensity plots have essentially the same characteristic shape suggested by the work of Klebanoff (1955). To emphasize the near-wall region, the data of figure 3.3.6, for $y/\delta \leq 0.1$, is replotted in figure 3.3.7. Note that when the data taken above the line is referenced to the flat plate, this shifts the region of maximum turbulence intensity from $y^+ \cong 12$ to $y^+ \cong 17$. Clearly, the presence of the line acts to essentially shift the turbulent behavior by the width of the line. Notice that although there are some small variations in behavior for $y^+ \leq 10$, any differences have relaxed back to flat plate behavior by $y^+ \simeq 35$, essentially consistent with the previous mean velocity profile results. Thus, the presence of the lines appears to have only a limited effect on turbulence intensity which is concentrated primarily in the near-wall region. Other turbulence intensity profiles are shown in appendix F.

3.3.3 SPANWISE PROFILES

To better understand the effects of the modifying lines on both the mean velocity and turbulence intensity, transverse profiles were measured at $y^+ = 5$ and $y^+ = 10$ (referenced to the flat plate) for $s^+ = 111$ and $h^+ = 3.8$. The center of the hot-film sensor was located above a line at

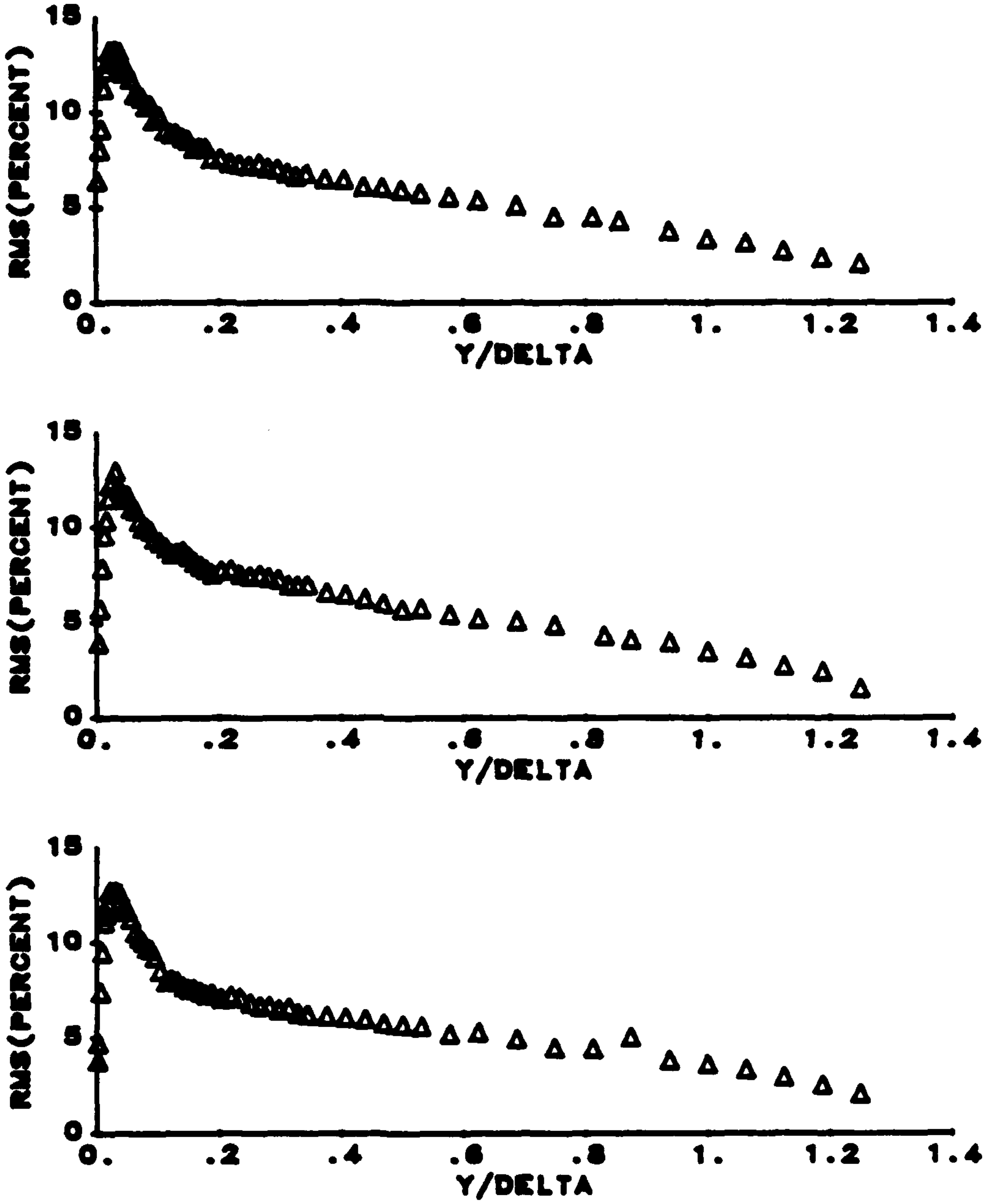

Figure 3.3.6. Plot of $\sqrt{\overline{u'^2}}/U$ vs. y/δ, plate-1. $Re_\Theta \simeq 1400$, $h^+ = 4.3$, $s^+ = 142$, $x = 2.06$m, and $\nu = 0.875*10^{-6}$ m^2/s: (TOP), Flat plate; (MIDDLE), Between two lines; (BOTTOM), Above a line with $y^+ = 0$ referenced to the top of the line.

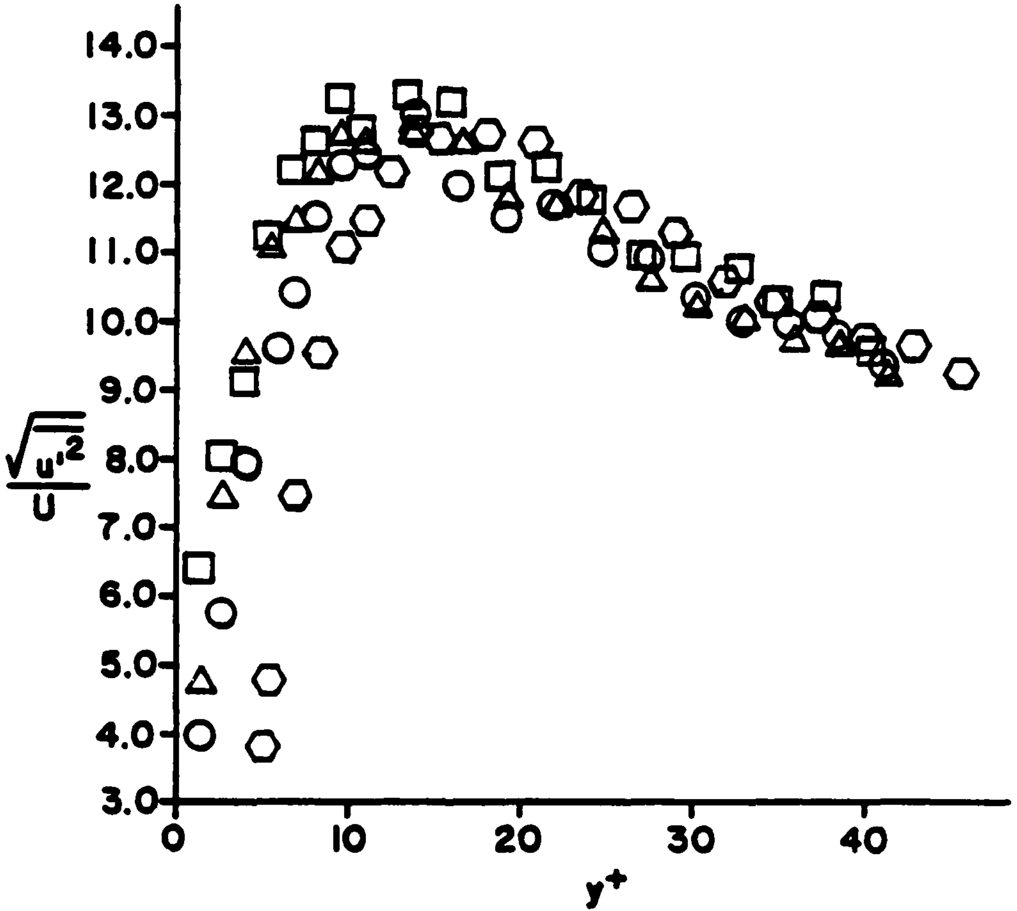

Figure 3.3.7. Plot of $\sqrt{\overline{u'^2}}/U$ vs. y/δ for $y/\delta < 0.1$, plate-1. $Re_\Theta \approx 1400$, $h^+ = 4.3$, $s^+ = 142$, $x = 2.06$m, and $\nu = 0.875 * 10^{-6}$ m^2/s: □, Flat plate; ○, Between two lines; △, Above a line with $y^+ = 0$ referenced to the top of the line; ⬡, Above a line with $y^+ = 0$ referenced to the flat plate.

the start of the profiles, and the probe was traversed in a spanwise direction for two line spaces. As might be expected, figure 3.3.8 demonstrates the presence of a mean velocity deficit above the lines for both $y^+ = 5$ and $y^+ = 10$, with the deficit rapidly diminishing with y^+, as would be expected from the results of section 3.2. The actual velocity deficit is probably greater than that which is indicated in figure 3.3.8, because the sensor size acts as a filter, creating a bias toward higher velocities above a line. This filtering effect is a result of the length of the hot-film sensing element being 4 times larger than the diameter of the modifying lines. Thus, the sensor in effect "filters" or averages out sharply varying velocity gradients.

Nakagawa et al. (1981), in a similar study ($k^+ = 51$, $h^+ = 51$, and $s^+ = 826$ & $k^+ = 45$, $h^+ = 90$, and $s^+ = 716$), also observed the mean velocity to be less above rectangular streamwise modifications than between the modifications. Their study also suggested turbulence intensity to be greater above than between modifications. At $y^+ = 5$, figure 3.3.9a suggests that the turbulence intensity is less above the lines than between them. Although this does not agree with the results of Nakagawa et al., one must keep in mind that their modifications extended through the buffer layer, and therefore were influencing the boundary layer outside the viscous sublayer where the dynamics of the flow are markedly different. Also, Walsh (1979, 1982) suggested geometric shape plays a major factor in drag reduction behavior, with rectangular modifications creating apparent increases in drag. Figure 3.3.9b suggests that at $y^+ = 10$ any effect of the lines on turbulence intensity is essentially undetectable.

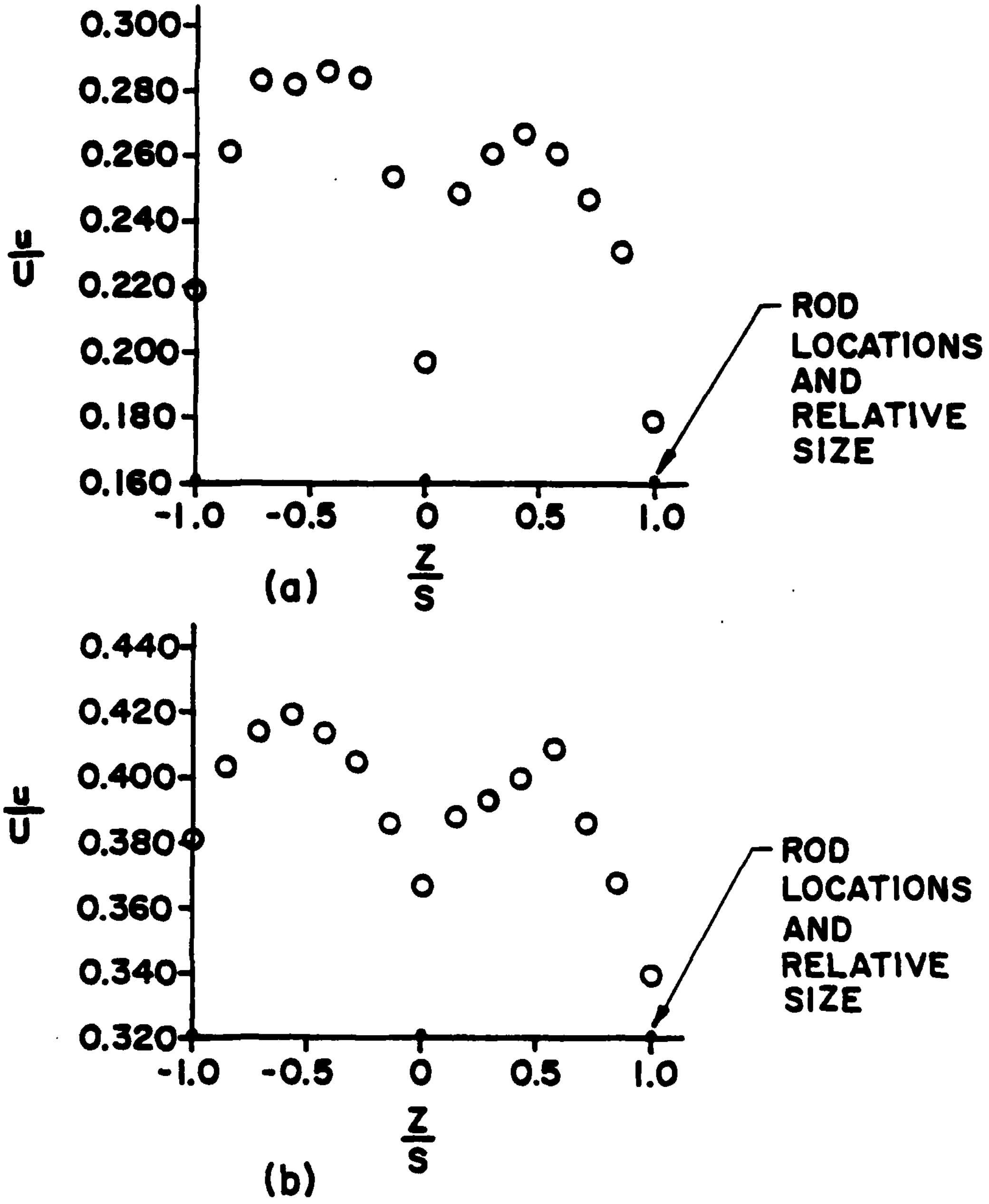

Figure 3.3.8. Transverse mean velocity profiles, plate-2. $Re_\theta \approx 1500$, $h^+ = 3.8$, $s^+ = 111$, $x = 2.06$m, and $\nu = 0.990*10^{-6}$ m^2/s. (a) $y^+ = 5$ referenced to flat plate, (b) $y^+ = 10$ referenced to flat plate.

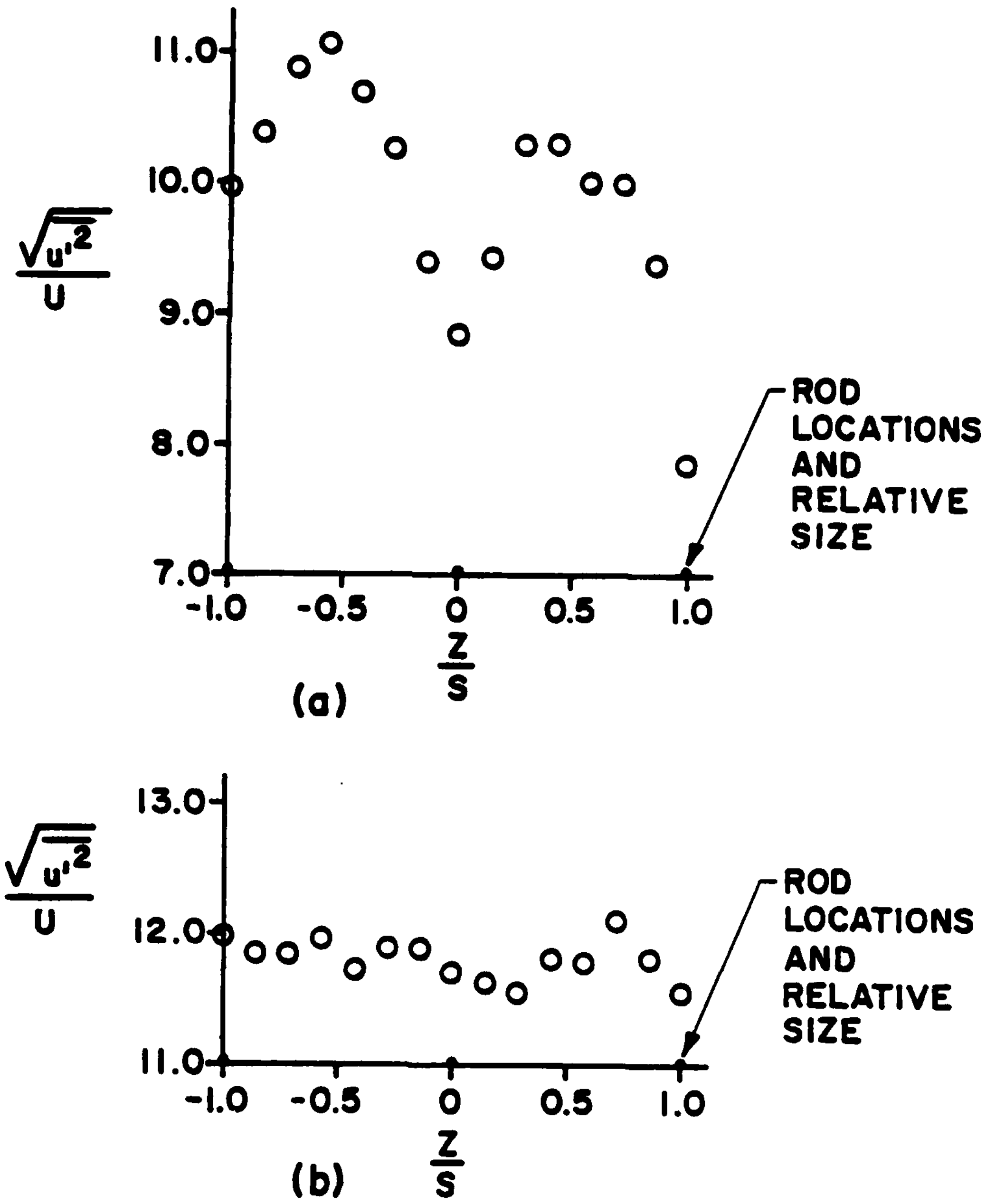

Figure 3.3.9. Transverse turbulence intensity profiles, plate-2. $Re_\theta \approx 1500$, $h^+ = 3.8$, $s^+ = 111$, $x = 2.06$m, and $\nu = 0.990 * 10^{-6}$ m^2/s. (a) $y^+ = 5$ referenced to flat plate, (b) $y^+ = 10$ referenced to flat plate.

To briefly summarize, it appears that the lines introduce a transverse velocity deficit in the near-wall region, in agreement with the visual results of section 3.1. Both mean velocity and turbulence intensity are suggested to be lower above lines than between them. However, the effects of the lines do not appear to extend beyond approximately $y^+ = 35$, with the overall characteristics of the turbulent boundary layer remaining unaffected.

3.3.4 BOUNDARY LAYER PARAMETERS

In order to establish the potential effect of the surface modifications on drag, the mean velocity data was integrated using the momentum thickness and displacement thickness equations:

$$\Theta = \frac{1}{U^2}\int_0^\delta u(U-u)dy \quad \text{momentum thickness} \qquad (12)$$

$$\delta_d = \frac{1}{U}\int_0^\delta (U-u)dy \quad \text{displacement thickness.} \qquad (13)$$

A trapizoidal integration scheme was employed using the 65 data point mean velocity profiles. Because of the large velocity gradients associated with the region $y^+ < 40$, 19-20 data points were taken in this region during the experimental measurements,which produced smooth curves for the entire integration process, thus minimizing the integration error. The integrated values of δ_d and Θ were then used to establish the shape factor (H), the momentum thickness Reynolds number (Re_Θ), and the ratio of modified surface to flat plate momentum thickness (Θ_{mod}/Θ_{fp}). The above parameters are listed in table-2 for the various data runs of the present study.

Table 2: Flow and Boundary Layer Parameters From Hot-Film Experiments

Data File	Plate Probe Location	x(m)	h^+	s^+	U(m/s)	$\nu(\frac{m^2}{s})(*10^{-6})$	δ_d(mm)	Θ(mm)	H	C_f	Re_Θ	$\frac{\Theta_{mod}}{\theta_{FP}}$
1	1-FP	1.83			.250	1.041	.536	.402	1.33	.0045	964	
2	1-BL	1.83	3.5	118	.244	1.000	.542	.415	1.30	.0045	1011	1.03
3	1-AL	1.83	3.5	118	.253	1.000	.522	.407	1.28	.0045	1030	
10	2-UM	0.84			.252	1.015	.506	.359	1.41	.0048	890	
11	2-FP	0.84			.252	0.987	.475	.333	1.43	.0048	847	
12	2-FP	1.52			.256	0.985	.595	.434	1.37	.0043	1127	
13	2-BL	1.52	3.8	111	.256	0.990	.607	.454	1.34	.0045	1175	
14	2-AL	1.52	3.8	111	.256	0.940	.556	.425	1.31	.0045	1158	
15	2-FP	2.06			.265	0.944	.694	.498	1.39	.00415	1399	
16	2-BL	2.06	3.8	111	.265	0.916	.743	.555	1.34	.00414	1606	
17	2-AL	2.06	3.8	111	.265	0.924	.680	.523	1.34	.0042	1500	
18	2-DM	2.16			.265	0.990	.739	.539	1.37	.00425	1445	1.08
19	2-FP	2.16			.265	0.972	.684	.499	1.37	.00430	1360	
20	1-FP	2.06			.256	0.900	.636	.456	1.40	.00435	1297	
21	1-BL	2.06	4.3	142	.262	0.870	.654	.469	1.39	.00430	1414	1.03
22	1-AL	2.06	4.3	142	.262	0.875	.632	.458	1.38	.00430	1371	
23	1-FP	2.06			.259	0.860	.652	.460	1.42	.00423	1386	
24	1-BL	2.06	4.3	71	.259	0.850	.691	.495	1.40	.00413	1508	1.08
25	1-AL	2.06	4.3	71	.259	0.867	.703	.509	1.38	.00418	1521	

The motivation for determining $(\Theta_{mod}/\Theta_{fp})$ is to provide an approximate indication of the drag reducing potential of the modified surfaces examined. The relationship of this parameter to surface drag can be shown by considering the well known von Karman integral equation in the form:

$$\tau_o = \rho \frac{d}{dx} (U^2\Theta) + \rho\delta_d U \frac{dU}{dx} . \qquad (14)$$

For an ideal flat plate flow (zero pressure gradient, constant free stream velocity) equation (14) reduces to:

$$\tau_o = \rho U^2 \frac{d\Theta}{dx} \qquad \text{or} \quad 2C_f = \frac{d\Theta}{dx} . \qquad (15)$$

For an incompressible flow the integration of equation (15) yields:

$$\text{FRICTION DRAG} = \int_{x_{initial}}^{x_{final}} \tau_o dx = \rho U^2 \int_{\Theta_{initial}}^{\Theta_{final}} d\Theta$$

$$\frac{\text{FRICTION DRAG}}{\rho U^2} = \Theta_{final} - \Theta_{initial} . \qquad (16)$$

Thus, for a constant free stream velocity the total frictional drag over a region is directly proportional to the change in the momentum thickness. However, during the present study a slight acceleration of the flow was experienced due to the boundary layer blockage effects. Accounting for the effects of this acceleration in the von Karman integral equation indicated that to within 1% (less than the uncertainty of the calculation), The motivation for determining $(\Theta_{mod}/\Theta_{fp})$ is to provide an approximate indication of the drag reducing potential of the modified surfaces examined. The relationship of this parameter to surface drag can be shown by considering the well known von Karman integral equation in the form:

$$\tau_o = \rho \frac{d}{dx} (U^2\Theta) + \rho\delta_d U \frac{dU}{dx} . \qquad (14)$$

For an ideal flat plate flow (zero pressure gradient, constant free stream velocity)equation (14) reduces to:

$$\tau_o = \rho U^2 \frac{d\Theta}{dx} \quad \text{or} \quad 2C_f = \frac{d\Theta}{dx} . \qquad (15)$$

For an incompressible flow the integration of equation (15) yields:

$$\text{FRICTION DRAG} = \int_{x_{initial}}^{x_{final}} \tau_o dx = \rho U^2 \int_{\Theta_{initial}}^{\Theta_{final}} d\Theta$$

$$\frac{\text{FRICTION DRAG}}{\rho U^2} = \Theta_{final} - \Theta_{initial} . \qquad (16)$$

Thus, for a constant free stream velocity the total frictional drag over a region is directly proportional to the change in the momentum thickness. However, during the present study a slight acceleration of the flow was experienced due to the boundary layer blockage effects. Accounting for the effects of this acceleration in the von Karman integral equation indicated that to within 1% (less than the uncertainty of the calculation), the ratio of the momentum thickness provides a sufficiently good indication of the relative change in total surface friction drag. Thus, Θ_{mod}/Θ_{fp} was employed in the present study as the parametric indication of changes in surface drag.

Since the modifications ran the entire length of plate-1, the ratio Θ_{mod}/Θ_{fp} was calculated from the actual momentum thicknesses obtained at the same streamwise extent, above both the modified surfaces ([illegible]ween two lines) and the flat plate (i.e., this assumes $\Theta_{init} = 0$ at x [illegible]). To establish Θ_{mod}/Θ_{fp} for test plate-2, the change in momentum thi[illegible] across the inserted modified test section ($\Delta\Theta/\Delta x$) was compared to the change in momentum thickness over the same streamwise extent on the adjacent flat plate section.

The momentum thickness ratios (Θ_{mod}/Θ_{fp}) for all the modification spacings tested are shown in figure 3.3.10; Although the data is limited, the four points shown suggest that the total friction drag for the modified test sections was always slightly greater than that of the adjacent flat plate test sections, with Θ_{mod}/Θ_{fp} apparently increasing with decreasing s^+. For comparison, $\overline{\lambda^+}$ vs. s^+ data obtained from the visual studies is also shown on figure 3.3.10. Since $\overline{\lambda^+}$ is observed to <u>decrease</u> with decreasing s^+, this suggests that a decrease in line spacing forces a decreased streak spacing, which in turn increases streak bursting per unit area, yielding an increase in surface momentum exchange which manifests itself as increased surface drag (i.e. an increased Θ_{mod}/Θ_{fp}). Thus the modified surfaces examined here do not appear to have the potential for reducing surface friction drag, but they clearly indicate an apparent relationship between the number of streaks present on a surface and the relative friction drag of that surface.

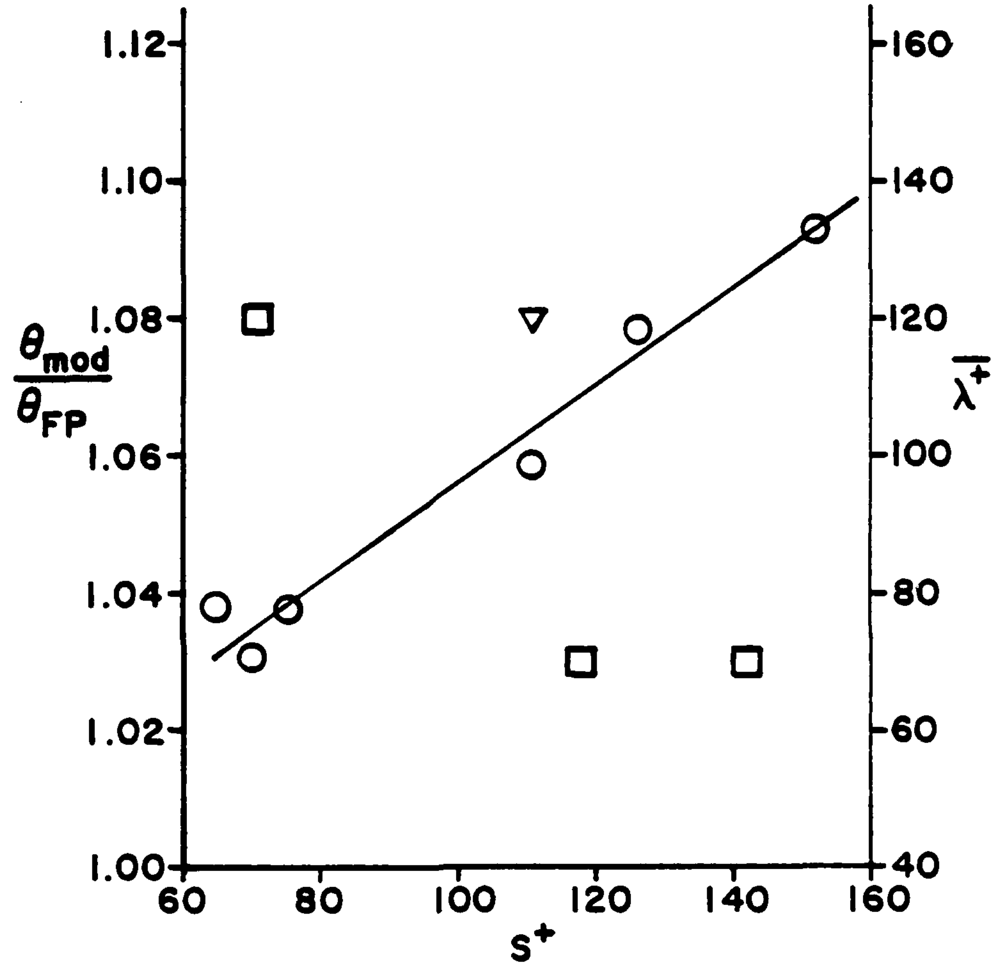

Figure 3.3.10. Plot of mean streak spacing ($\overline{\lambda^+}$) and Θ_{mod}/Θ_{fp} vs. line spacing (s^+); $Re_\Theta = 1300\text{-}1600$. ○, streak spacing data; □, Θ_{mod}/Θ_{fp} from plate-1; ▽, Θ_{mod}/Θ_{fp} from plate-2.

4 GENERAL DISCUSSION

The results of the studies presented in the previous chapter indicate that for $y^+ \leq 10$ the statistical characteristics of the spanwise spacing of low-speed streaks can be influenced by the presence of cylindrical streamwise surface modifications that scale on the order of the viscous sublayer. However, modifications which traversed the entire length of the test plate were observed to have a more substantive effect as organizing "sites" for the low-speed streaks than the modifications which began 0.91 m downstream from the leading edge. This suggests that the influence of the lines on streak location may be history dependent, i.e., dependent on the extent of the lines and probably the conditions present at transition to turbulence.

Both the transverse mean velocity profiles and the law-of-the-wall plots of section 3.3 indicate the presence of a velocity deficit above the lines for a distance out to about $y^+ \simeq 30$. The lines apparently act as an extension of the plate, causing spanwise perturbations in the vorticity sheet at the surface which gives rise to spanwise distributed "wakes" which act as nucleation sites for low-speed streak development.

Streak waviness and partial bursting were observed to occur more frequently above the lines than above the flat plate; this may be due to the greater persistence of the "wakes" which occur directly above each line. It is hypothesized that when these wakes interact with inflows of high speed fluid, the interaction process is less chaotic, resulting in more limited turbulence producing events rather than a few large breakdowns. Note that due to the visualization technique employed in this study, the observed streak head is generally visualized at a lower y^+, and thus closer to the line than the streak tail (due to streak lift-up). Thus, the observed streak head is stabilized by the presence of the line, whereas the tail is farther from the stabilizing effect of the line and will interact more strongly with other streaks and inflows, creating the appearance of waviness. Weak inflows above the lines probably result in streak waviness, while strong inflows probably result in the causation of the observed partial bursting which is predominant above the lines. In contrast, for a flat plate flow, fluid inflows and streak interactions primarily result in lateral movement of the whole streak. The predominance of lateral movement, rather than the waviness and partial bursting observed above the lines, is probably due to the lack of a stabilizing site on the flat plate and the occurrence of fewer, but more chaotic breakdowns as discussed above.

As was suggested by the transverse turbulence intensity profile of figure 3.3.10b, the influence of the lines on streak characteristics quickly diminishes for $y^+ \geq 10$. Since $y^+ \cong 12$ is generally accepted as the region of maximum turbulence intensity within a turbulent boundary layer, the decreasing influence of the modifications for $y^+ \geq 10$ may be a result of the process which causes the large velocity fluctuations which are present in this region. It is speculated that these intense velocity and vorticity fluctuations are the result of a complicated and intense process of streamwise vortex interaction and coalescence, which causes a rapid agglomeration of the smaller streamwise scales near the plate surface into larger scales farther removed from the surface. Under such a process, streak spacings and characteristics above the streamwise modifications could rapidly revert to those of a conventional flat plate flow, as was observed.

Perry and Chong (1982) have suggested a detailed loop or Λ vortex model as an explanation of the origin of low-speed streaks on a flat plate. After observation of 5-6 hours of video tape, the present authors propose that a similar loop vortex model, with the head of the vortex above a line and the vortex legs straddling the line, is a key element of the flow behavior which cause the low-speed streaks to be affected by the types of modified surfaces examined in the present study. Figure 4.1 is a schematic representation of the speculated loop vortex model. The streak formation results from the loop vortex legs, which appear as a pair of counter-rotating vortices ($\pm w_x$). These paired vortices interact with the low-speed fluid to pump fluid upward above the line where it combines with the fluid of the line wake. The counter rotating vorticity of adjacent legs of different vortex loops helps to induce high-speed fluid toward the plate (inflow), where the fluid interacts with the surface and is slowed through viscous dissipation. The resulting low-speed fluid, created by this interaction, is subsequently concentrated into a streak by the pumping action of the paired vortices, thus completing a path from high-speed outer flow to low-speed streak fluid. Once the streak grows to a minimum size or extent by accretion of fluid, it becomes unstable, breaking down into a series of loop vortices (caused by an inviscid-type instability) which both 1) eject low-speed fluid into the outer region, and 2) provide the vortex structure for reinforcement of the low-speed streaks. This is consistent with the model of streak formation suggested previously by Smith and Metzler (1982)

Walsh's results (1979 & 1982) indicated that riblet test surfaces with $h^+ = 10\text{-}20$ and $s^+ = 10\text{-}20$ result in net drag reductions, whereas all test cases examined in the present study resulted in slight net increases

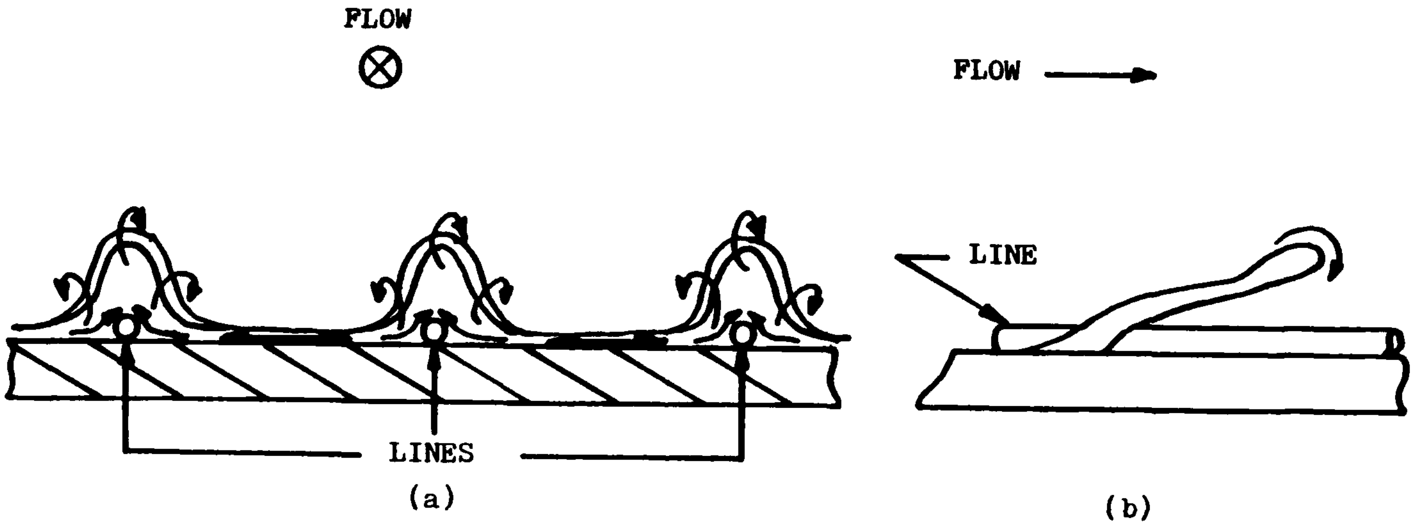

Figure 4.1. Suggested loop vortex model. (a) End-view (looking downstream), (b) Corresponding side-view.

in drag (see fig. 3.3.11). The loop vortex model of the present study suggests that the line spacings of the order of the flat plate mean streak spacing ($\overline{\lambda^+} = 100$) would tend to enhance streak formation by the lines acting as sites for the formation of the suggested loop vortex structures. However, since the effective drag reducing riblets of the studies by Walsh were of much smaller scale than the mean flat plate streak spacing, modification of the loop vortices by the riblets does not seem reasonable. The authors can only speculate that the drag reduction of riblet surfaces may be the result of the riblets inhibiting the lateral concentration of dissipated low-speed fluid near the surface. If such is the case, instead of the low-speed fluid being pumped into a low-speed streak, it would be channeled downstream, probably impeding streak development, bursting, and therefore, momentum exchange. Further studies are planned to examine this hypothesis.

5 CONCLUSIONS

The effect of streamwise cylindrical surface modifications, of the scale of the viscous sublayer ($h^+ \cong 5$), on the low-speed streak structure occurring in the near-wall region of turbulent boundary layers was examined using both hydrogen bubble flow visualization and hot-film anemometry techniques. The results of these studies lead to the following conclusions:

1) These types of streamwise surface modifications do influence the low-speed streak formation process near the surface, particularly for spacings of $s^+ < 100$.

2) The region of influence of these modifications is confined very close to the plate, with the organizing effects of the lines diminishing rapidly after $y^+ \cong 10$.

3) The influence of the lines appears to be history dependent with modifications which originate prior to transition appearing to have a greater influence on the streak patterns than those originating after the development of an established turbulent boundary layer.

4) The particular surface mofidications examined appear to result in a net drag increase of 3 percent or more compared to identical flat plate conditions.

5) Reductions of line spacings below the accepted mean streak spacing for a comparable flat plate flow caused the largest increases in relative drag; the suggested mechanism for this increase is the development of more "bursting" sites due to narrower streak spacing, resulting in elevated surface momentum exchange.

REFERENCES

Aitchison, J. and Brown, J.A.C. 1957. The Lognormal Distribution, Cambridge University Press, New York.

Clauser, F.H. 1956. "The Turbulent Boundary Layer," Advances in Applied Mechanics, 4, 1.

Grass, A.J. 1971. "Structural Features of Turbulent Flow Over Smooth and Rough Boundaries," J. Fluid Mech., 50, 233.

Gupta, A.K., Laufer, J., and Kaplan, R.E. 1971. "Spatial Structure in Viscous Sublayer," J.Fluid Mech., 50, part 3, 493.

Hastings, N.I.J. and Peacock, J.B. 1975. Statistical Distributions, Butterworth & Co., London, 84.

Kim, H.T., Kline, S.J., and Reynolds, W.C. 1971, "The Production of Turbulence Near a Smooth Wall in a Turbulent Boundary Layer," J. Fluid Mech., 50, part 1, 133.

Klebanoff, P.S. 1954. NACA-TN 3178.

Klebanoff, P.S. 1955. "Characteristics of Turbulence in a Boundary Layer with Zero Pressure Gradient," NACA-Rep. 1247.

Klebanoff, P.S., Schubauer, G.B., and Tidstrom, K.D. 1955. "Measurements of the Effect of Two-Diemnsional and Three-Dimensional Roughness Elements on Boundary-Layer Transition," J. Aeronautical Sciences, 22, no. 11, 803.

Kline, S.J., Reynolds, W.C., Schraub, F.A., and Runstadler, P.W. 1967. "The Structure of Turbulent Boundary Layers," J. Fluid Mech., 30, part 4, 741.

Liu, C.K., Kline, S.J., and Johnston, J.P. 1967. "An Experimental Study of Turbulent Boundary Layer on Rough Walls," Report MD-15, Stanford University.

Metzler, S.P. 1980. "Processes in the Wall Region of a Turbulent Boundary Layer," M.S. Thesis, Dept. of Mech. Engr. & Mech., Lehigh University.

Nakagawa, H. and Nezu, I. 1981. "Structure of Space-Time Correlations of Bursting Phenomena in an Open-Channel Flow," J.Fluid Mech., 104, 1.

Nakagawa, H., Nezu, I., and Tominaga, A. 1981. "Spanwise Streaky Structure and Macroturbulence in Open-Channel Flows," Memoirs of the Faculty of Engr. Kyoto University, 34.

Offen, G.R. and Kline, S.J. 1975. "A Proposed Model of the Bursting Process in Turbulent Boundary Layers," J. Fluid Mech., 70, part 2, 209.

Oldaker, D.K. and Tiederman, W.G. 1977. "Spatial Structure of the Viscous Sublayer in Drag Reducing Flows," Physics of Fluids, 20, no. 10, part II, S133.

Perry, A.E. and Chong, M.S. 1982. "On the Mechanism of Wall Turbulence," J. Fluid Mech., 119, 173.

Purtell, L.P., Klebanoff, P.S., and Buckley, F.T. 1981. "Turbulent Boundary Layer at Low Reynolds Number," Physics of Fluids, 24, no. 5, M802.

Schraub, F.A. and Kline, S.J. 1965. "A Study of the Structure of the Turbulent Boundary Layer With and Without Longitudinal Pressure Gradients," Report MD-12, Dept. of Mech. Engr., Stanford University.

Smith, C.R. 1978. "Visualization of Turbulent Boundary Layer Structure Using a Moving Hydrogen Bubble-Wire Probe," Coherent Structure of Turbulent Boundary Layers, C.R. Smith and D.E. Abbott, ed., AFOSR/Lehigh University Workshop, Dept. of Mech. Engr. & Mech., Bethlehem, PA, 50.

Smith, C.R. and Metzler, S.P. 1982. "A Visual Study of the Characteristics, Formation, and Regeneration of Turbulent Boundary Layer Streaks," Development in Theoretical and Applied Mechanics, Vol. XI, Chung, T.J. and Karr, G.R., ed., University of Alabama in Huntsville, 533.

Smith, C.R. and Metzler, S.P. 1983 "The Characteristics of Low-Speed Streaks in the Near-Wall Region of a Turbulent Boundary Layer," J. Fluid Mech., 129, 27.

Walsh, M.J. and Weinstein, L.M. 1978. "Drag and Heat Transfer on Surfaces With Small Longitudinal Fins," AIAA Paper 78-1161, AIAA 11th Fluid and Plasma Dynamics Conference, Seattle, Washington.

Walsh, M.J. 1979. "Drag Characteristics of V-Groove and Transverse Curvature Riblets," Symposium on Viscous Drag Reduction, Dallas, Texas, 168.

Walsh, M.J. 1982. "Turbulent Boundary Layer Drag Reduction Using Riblets," AIAA Paper 82-0169, AIAA 20th Aerospace Sciences Meeting, Orlando, Florida.

White, F.M. 1974. Viscous Fluid Flow, McGraw-Hill, Inc., New York.

APPENDIX A: HOT-FILM PROBE SUPPORT, TRAVERSING MECHANISM, AND PROBE ZERO-REFERENCING

To help eliminate breakage of the delicate quartz-coated hot-film probes during near-wall velocity readings, a special probe traversing mechanism was designed which mounted on the support platform discussed in chapter 2. What is unique about this traversing mechanism is that the main vertical traversing mechanism, a Disa 55E40 traversing mechanism, could itself be traversed in the vertical direction (up from the flat plate).

Two Starrett micrometers provided a maximum probe traverse of 50 mm, with a resolution of 0.01 mm, in both the streamwise and transverse flow directions. A ball bearing converted the rotational motion of the micrometers to linear motion. Brass bushings provided the tolerances (±0.013 mm) between the guide rods and slide blocks necessary to eliminate binding. The maximum vertical traverse of 100 mm, with a resolution of 0.1 mm, was provided by the Disa 55E40 traversing mechanism. However, the Disa 55E40 could be traversed vertically 50 mm, with a resolution of 0.01 mm, by means of a third Starrett micrometer traverse. This proved very useful in zero-referencing of the probe to the flat plate.

The probe was inserted into a Disa 6 mm diameter mounting tube (55H240) which was connected to a Disa 55H140 toothed guide tube. The guide tube was then mounted into the Disa 55E40 traversing mechanism; providing slipless drive once locked in place.

The 55E40 vernier was turned to zero and the probe support was lowered by hand, until it was located approximately 15 mm from the surface of the flat plate test section, and then it was locked in place. The entire 55E40 traversing mechanism was then slowly lowered by use of the micrometer traverse. Zero-reference was established when the image of the hot-film probe, in the plexiglas flat plate test section, was observed to touch the actual probe. A full zoom video side picture, with a vertical white mm scale in the immediate probe background, greatly aided this procedure (see figure A.1). Once zero-referencing of the probe was completed the micrometer was locked, thereby eliminating the possibility of moving the probe through "zero" and breaking it on the test plate.

Vertical traverses were accomplished by the 55E40. Occasionally, the very near-wall probe locations ($y \leq 0.2$mm) were attained by using the micrometer traverse, since it was more accurate than the 55E40.

Thus, the traversing mechanism provided boundary layer traverse capability, with a resolution to 0.01 mm, while eliminating probe breakage, once probe zero-reference was accomplished.

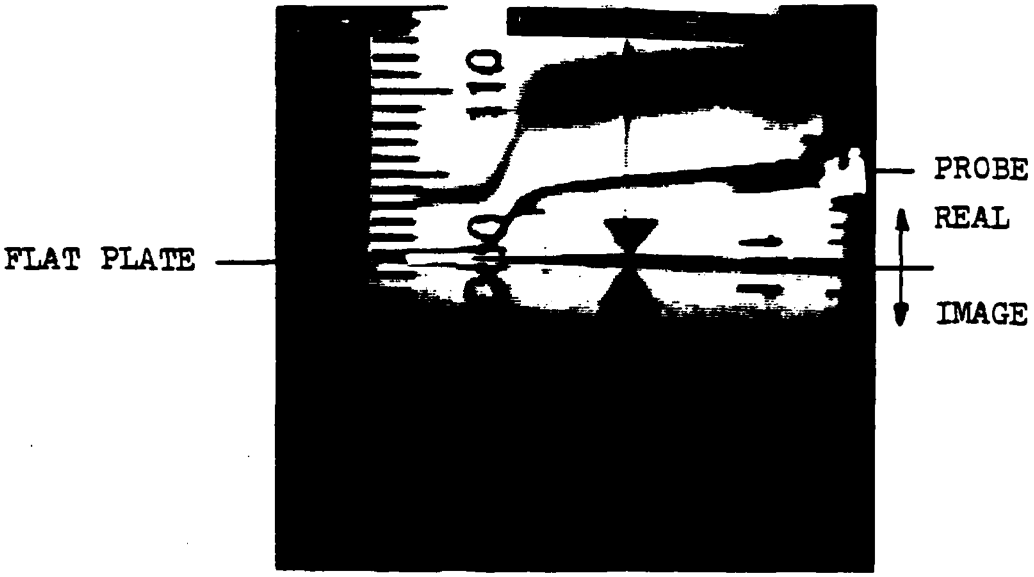

Figure A.1. Picture of properly zero-referenced hot-film probe.

APPENDIX B: OPERATION PROCEDURE OF DISA 55D01 ANEMOMETER AND DISA 55M25 LINEARIZER

In order to perform hot-film velocity and turbulence intensity measurements it is essential to have high quality water. Therefore, the water channel is drained and refilled prior to each series of hot-film anemometry studies. The water is filtered through one micron filters during the filling process and after each data taking session. Copper-sulfate is not added to the water, as it tends to create a thin plating of copper on the hot-film probe. Instead, chlorine is used to control the growth of micro-organisms.

After the channel is filled, the water is circulated for approximately five to seven days to allow the water to deaerate and reach room temperature. If this procedure is not followed, linearization is most difficult as oxygen bubbles form on the hot-film sensor, which results in inconsistent probe calibrations.

Two days prior to linearization and data acquisition, the anemometer, linearizer, and voltmeter are mounted on the support platform (discussed in chapter 2), and turned on to allow the electronics to reach steady state temperature.

One day prior to data acquisition, the rheostat governing the support platform traversing mechanism must be calibrated for six different velocities. This is accomplished by traversing the platform the entire length of the channel, but only timing the last 1.5 m of the traverse, thus allowing the mechanism time to reach a uniform steady speed. The calibration velocity is determined by the average of five traverses. The maximum calibration velocity (U_1) is chosen such that it is just slightly greater than the desired free-stream velocity of the tests to be conducted. Next it is essential to determine the rheostat setting that yields a platform velocity of $U_2 = \frac{1}{2} U_1$. Both U_1 and U_2 are the primary platform velocities used during the linearization process. After determining the calibration setting for U_1 and U_2, the rheostat must be calibrated for two support platform velocities less than U_1, but greater than U_2, and two velocities less than U_2.

The actual linearization process consists of adjustments to the linearizer that are determined from readings obtained at U_1 and U_2, but evaluation of the hot-film probe calibration at the other four velocities gives an indication of how accurate the linearization is over the entire velocity range of the boundary layer. The probe calibration for the two velocities less than U_2 is very important, since they are of the magnitude of the velocities in the boundary layer at $y^+ \leq 40$, where the largest velocity gradients occur.

The step-by-step linearization process of the Disa 55D01 anemometer and Disa 55M25 linearizer is listed below.

1) With the loop switch in standby and LF gain in the flat position, turn the power on and let the instruments warm up for a minimum of 4 hours.

2) To insure that the support platform traversing mechanism is functioning properly, check the rheostat calibration.

3) Determine the resistance of the wires and connectors.

   a) Insert the shorting probe into the probe support and connect to probe input to anemometer. Do not place shorting probe in the water.

   b) Leave loop switch in standby and LF gain in flat position. Set 0.10 ohms as a starting point to determine the resistance. Set meter switch to 10. Press toggle to resistance and observe meter deflection. If meter indicator moves left, increase the resistance; if it moves right, decrease the resistance. If no movement occurs then move the LF gain to high. In the high position use the input bias to center the meter indicator before depressing the resistance toggle. Repeat the above procedure with LF gain in the high position until no deflection occurs. The resistance set is R_s.

4) Determine the resistance of the hot-film probe.

   a) Insert probe into support.

   b) Check to see that ground wire is attached to probe support.

   c) Insert probe support into probe traversing mechanism and zero-reference as described in appendix A.

d) Set resistance to 7.90 ohms, as a starting point, and repeat the same procedure as in step 3. The resistance at the end is R_p.

5) Calculate the resistance to be set on the anemometer using an overheat ratio of 1.08, as follows:

$$R_{set} = 1.08(R_p - R_s) + R_s \ .$$

6) Dial in R_{set} on the anemometer and adjust input bias to mid-scale.

7) Turn anemometer to temperature mode as follows. With loop control in standby and LF gain in flat position, push toggle to temperature, and then loop control to internal. Switch LF gain to high as meter indicator starts to rise. When the meter indicator balances, switch the toggle to the neutral position (to turn anemometer from temperature mode to standby mode, flip loop control to standby and then move LF gain to flat).

8) Connect anemometer output to voltmeter and set time constant to 0.1 or 1 depending on time duration of traverse (see voltmeter manual).

9) Run platform traverse at U_1 and note voltage maximum (E_{max}).

10) Set the following on the linearizer:

a) The input range to the integer that is greater than $\frac{1}{2}E_{max}$ (i.e., $E_{max} = 10.5$, set input range to 6).

b) Set imput balance to 999.

c) Set exponent offset to 999.

d) Set exponent factor to 150 if input range is 6 and 130 if input range is 5.

e) Set gain low to 609.

f) Set gain high to 500.

g) Set common gain, var. exp., and var. exp. level to 0.

h) Set var. exp. sign to (+).

11) Connect anemometer output to voltmeter and determine voltage E_1 for velocity U_1 by means of a probe traverse.

12) Connect anemometer output to linearizer input, and linearizer output to voltmeter. Allow 2 minutes for traverse disturbances of step 11 to dissipate. Select DC, 10 volt scale, and 0.1 time constant on the voltmeter. Starting with the hundredths digit on the input balance of the linearizer, push and hold the balance button, and reduce the hundredths digit by one until the voltage switches from positive to negative. Return the hundredths digit to the last positive voltage position. Repeat the above for the tens and units digit on the input balance.

13) Disconnect the anemometer output and adjust the common offset until the voltage display reads ± 0.0.

14) Reconnect the anemometer output.

15) Set traverse speed to U_1 and run the traverse platform

the length of the water channel. If the voltage reading at the end of the channel traverse is less than E_1, raise the high gain. If the voltage reading is greater than E_1, lower the high gain. Continue running the platform traverse and adjusting the high gain until the voltage reading at the end of the channel traverse is equivalent to E_1. Now set the support platform traverse speed to that of U_2 and traverse the channel. If the voltage reading at the end of the channel traverse is $E_2 = \frac{1}{2} E_1$, go to step 16. If $E_2 < \frac{1}{2} E_1$, lower the exponent factor by 5. If $E_2 > \frac{1}{2} E_1$, then raise the exponent factor 5. Reset the high gain to obtain E_1 at U_1. Then check E_2 again. Continue procedure until $E_2 = \frac{1}{2} E_1$.

16) Make channel traverses at the four other calibrated velocities and record the voltages.

17) Plot voltage vs. velocity and check overall linearity of the plot. If the two lowest velocities do not plot on the linear line between (U_2, E_2) and (U_1, E_1), then adjust the low gain on the linearizer and repeat steps 15 through 17.

18) Set free-stream velocity based upon the linearization plot of step 17.

APPENDIX C: SAMPLE LOGNORMAL DISTRIBUTION AND PROBABILITY CALCULATIONS

Calculation procedures used for determination of both the lognormal distributions and the lognormal probability graphs, as presented in section 3.2, are discussed below.

a) CALCULATION OF LOGNORMAL PROBABILITY DISTRIBUTION

The streak spacing distribution was determined first. In the present study increments of $\Delta\lambda^+ = 10$ were used in determining the streak spacing distributions. The mean streak spacing was calculated and the standard deviation and coefficient of variation were determined using equations (1) and (2) in chapter 3.

Calculation of the lognormal probability distribution assumes that each bar ($\Delta\lambda^+ = 10$) in the streak spacing distribution is one unit. Therefore, λ and $\bar{\lambda}$ in equations (5) and (6), in chapter 3, must be non-dimensionalized by $\Delta\lambda^+$.

For example, in figure 3.2.8a $\overline{\lambda^+} = 92$ and $\psi_\lambda = 0.44$.

1) Substitution of ψ_λ into equation (7) yields ψ_o.

2) Substitution of $\bar{\lambda} = \overline{\lambda^+}/\Delta\lambda^+ = 92/10 = 9.2$ into equation (6) yields λ_o.

3) Substitution of λ_o and ψ_o into equation (5) for each increment on the streak spacing distribution yields $P(\lambda)$. i.e., For $\lambda_{actual} = 10$, $\lambda = 1$ is substituted to yield $P(1)$, etc.... The probability obtained was plotted at the center of each bar on the streak distribution histogram.

4) A smooth curve was fit through the plotted points.

b) CALCULATION OF LOGNORMAL PROBABILITY GRAPHS

1) The probability values from part (a) were substituted into equation (8) to yield $\alpha(\lambda)$.

2) $\alpha(\lambda)$ vs. $\lambda/\bar{\lambda}$ was plotted on probability paper.

3) To determine the true lognormal probability for a given ψ_λ the following was conducted.

3a) λ_o and ψ_o were calculated with $\bar{\lambda}$ as an unknown.

3b) A fractile was defined as $\lambda/\bar{\lambda}$.

3c) From Hastings and Peacock (1975):

1) $\dfrac{m\ \exp(+\sigma)}{\bar{\lambda}} = \dfrac{\lambda_o\ \exp(+\psi_o)}{\bar{\lambda}}$ and yields the fractile corresponding to $\alpha(\lambda) = 84.1\%$.

2) $\dfrac{m\ \exp(-\sigma)}{\bar{\lambda}} = \dfrac{\lambda_o\ \exp(-\psi_o)}{\bar{\lambda}}$ and yields the fractile corresponding to $\alpha(\lambda) = 15.9\%$.

3d) The coordinates $\left[\dfrac{\lambda_o\ \exp(+\psi_o)}{\bar{\lambda}},\ \alpha(\lambda) = 84.1\%\right]$ and $\left[\dfrac{\lambda_o\ \exp(-\psi_o)}{\bar{\lambda}},\ \alpha(\lambda) = 15.9\%\right]$ were plotted.

3e) The line through the two points of step 3d represents the true lognormal probability distribution of the given ψ_λ.

APPENDIX D: CLAUSER CROSS-PLOTS

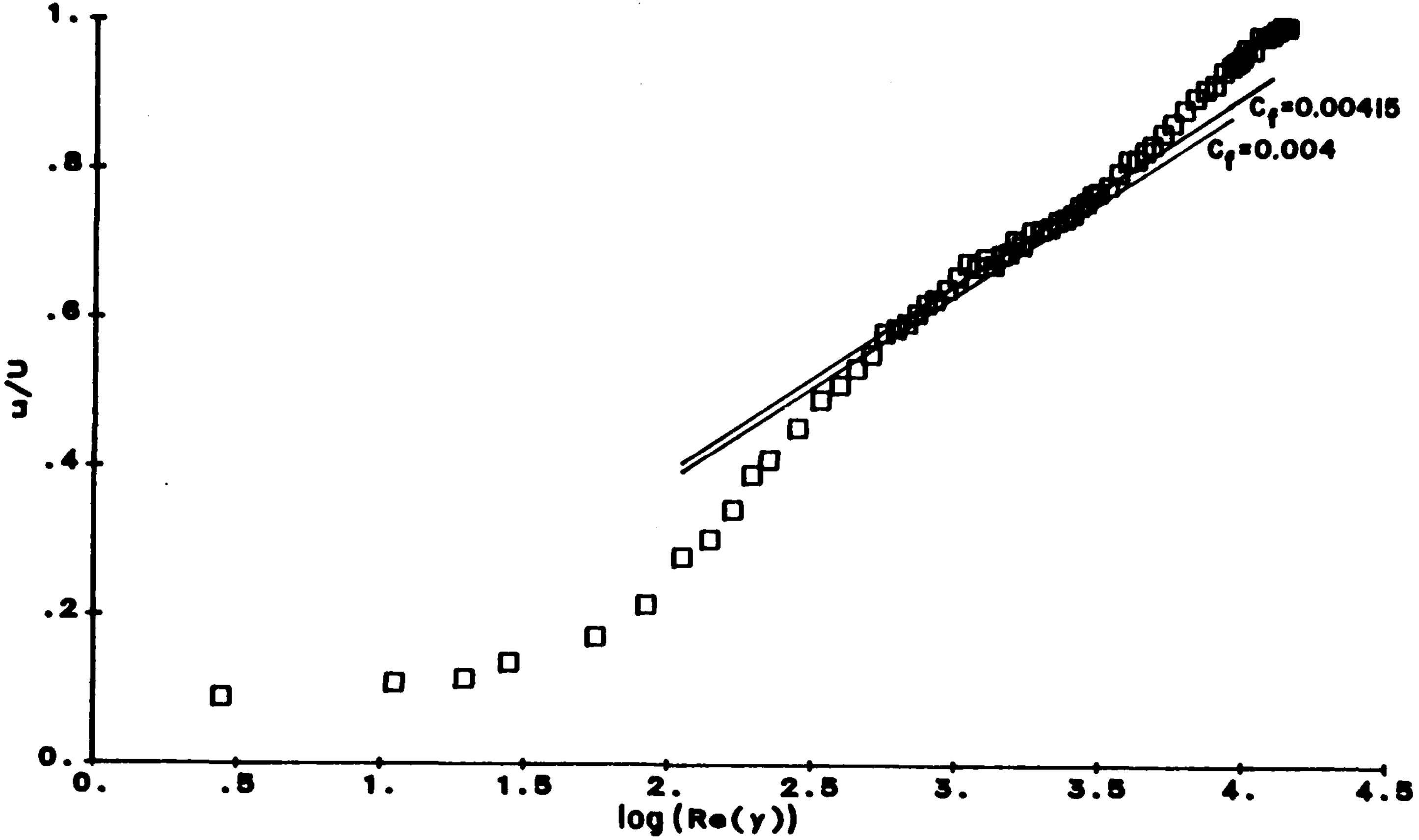

Figure D.1. Law-of-the-wall Clauser cross-plot. Plate-2, Flat plate, Data file 15, and $Re_{\Theta} = 1399$.

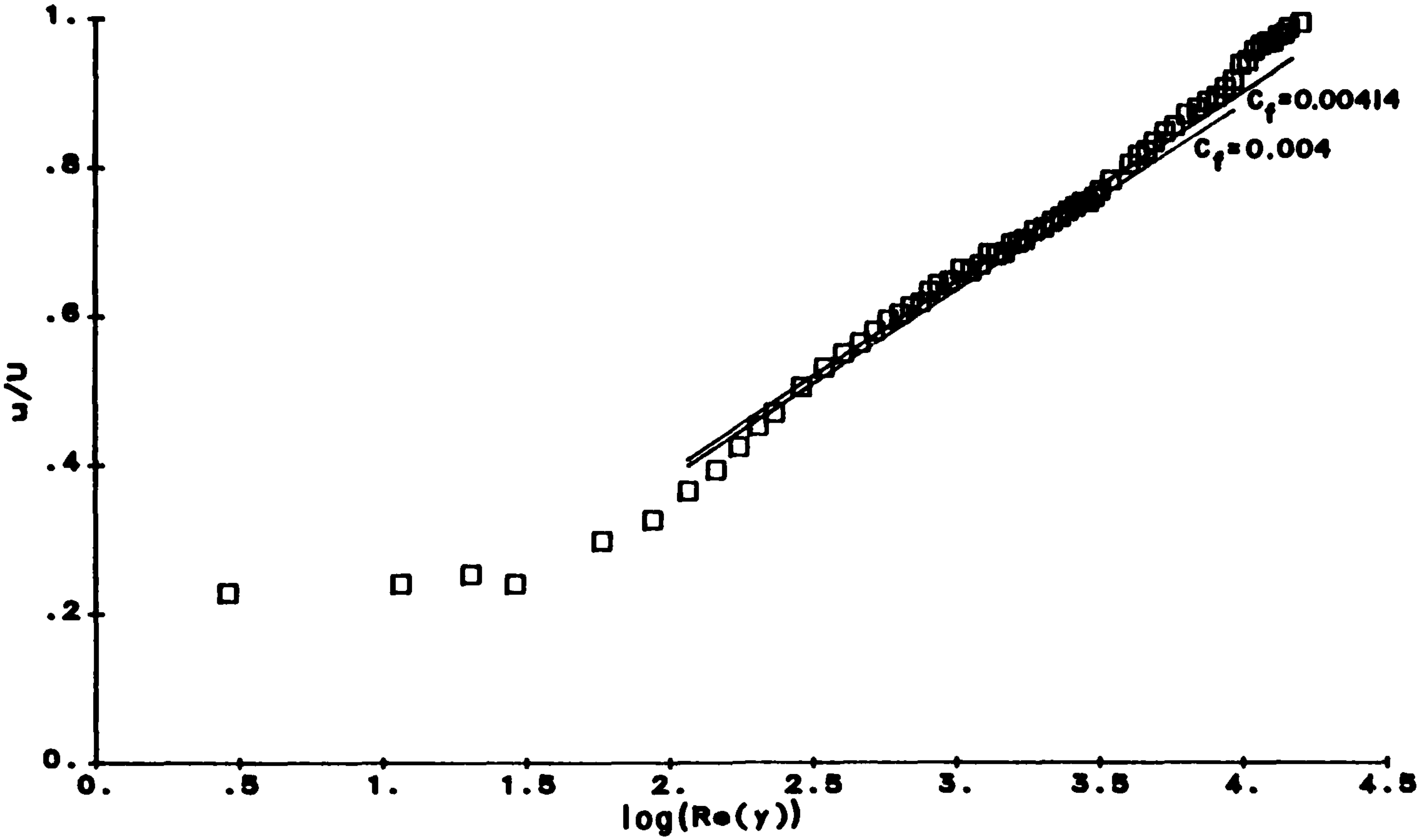

Figure D.2. Law-of-the-wall Clauser cross-plot. Plate-2, Between two lines, $h^+ = 3.8$, $s^+ = 111$, Data file 16, and $Re_\Theta = 1606$.

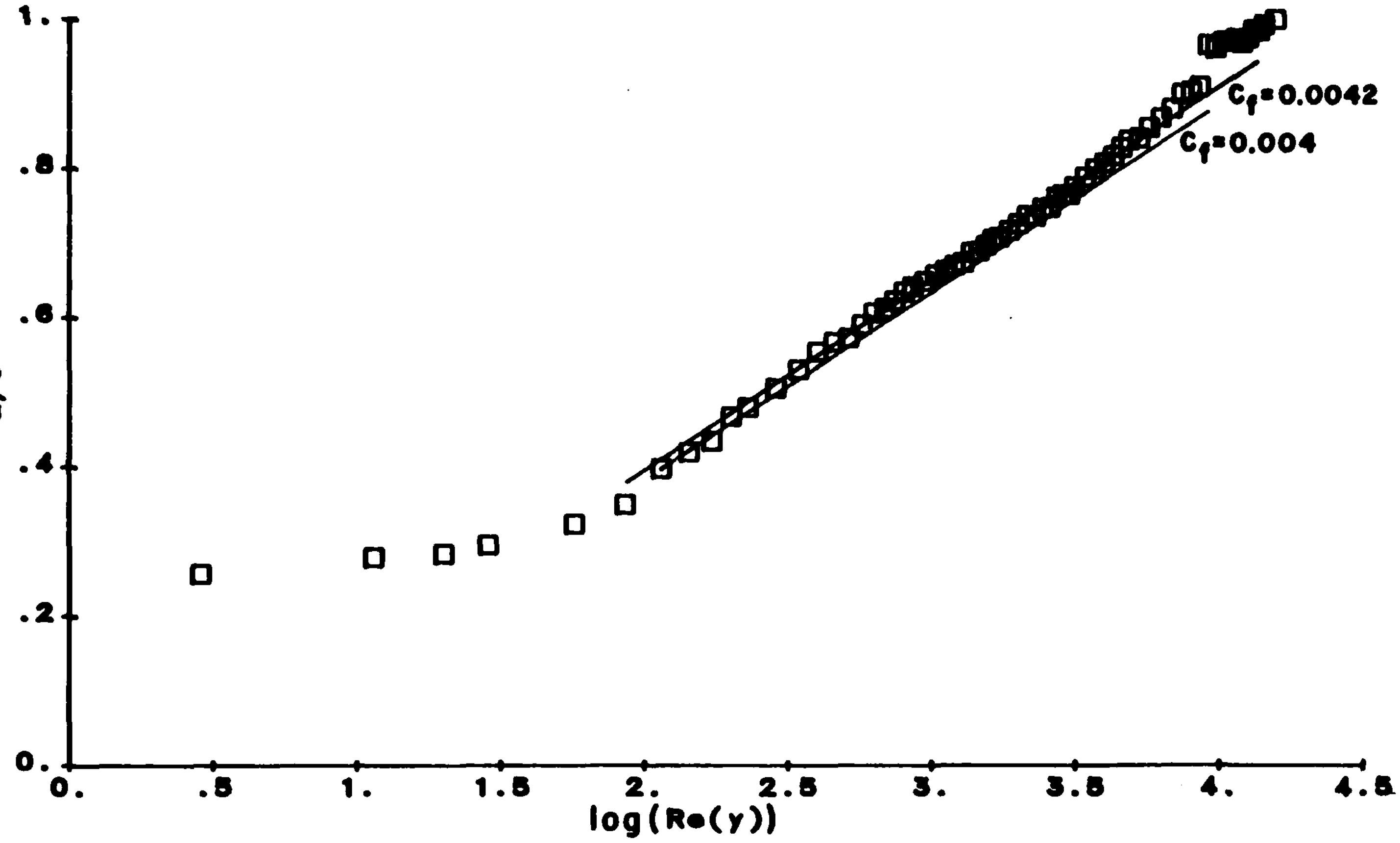

Figure D.3. Law-of-the-wall Clauser cross-plot. Plate-2, Above a line with $y^+ = 0$ referenced to the top of the line, $h^+ = 3.8$, $s^+ = 111$, Data file 17, and $Re_\Theta = 1500$.

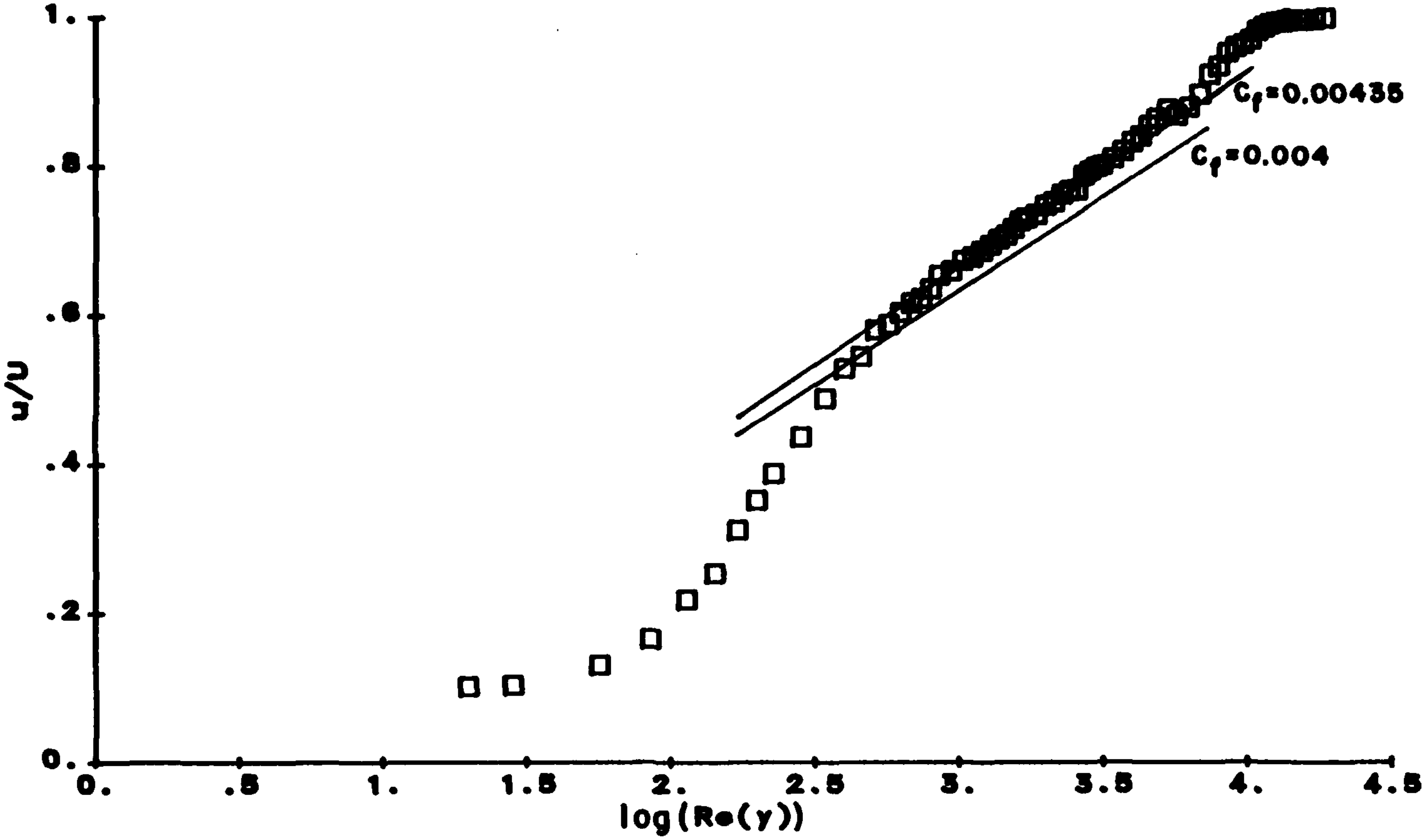

Figure D.4. Law-of-the-wall Clauser cross-plot. Plate-1, Flat plate, Data file 20, and $Re_\Theta = 1297$.

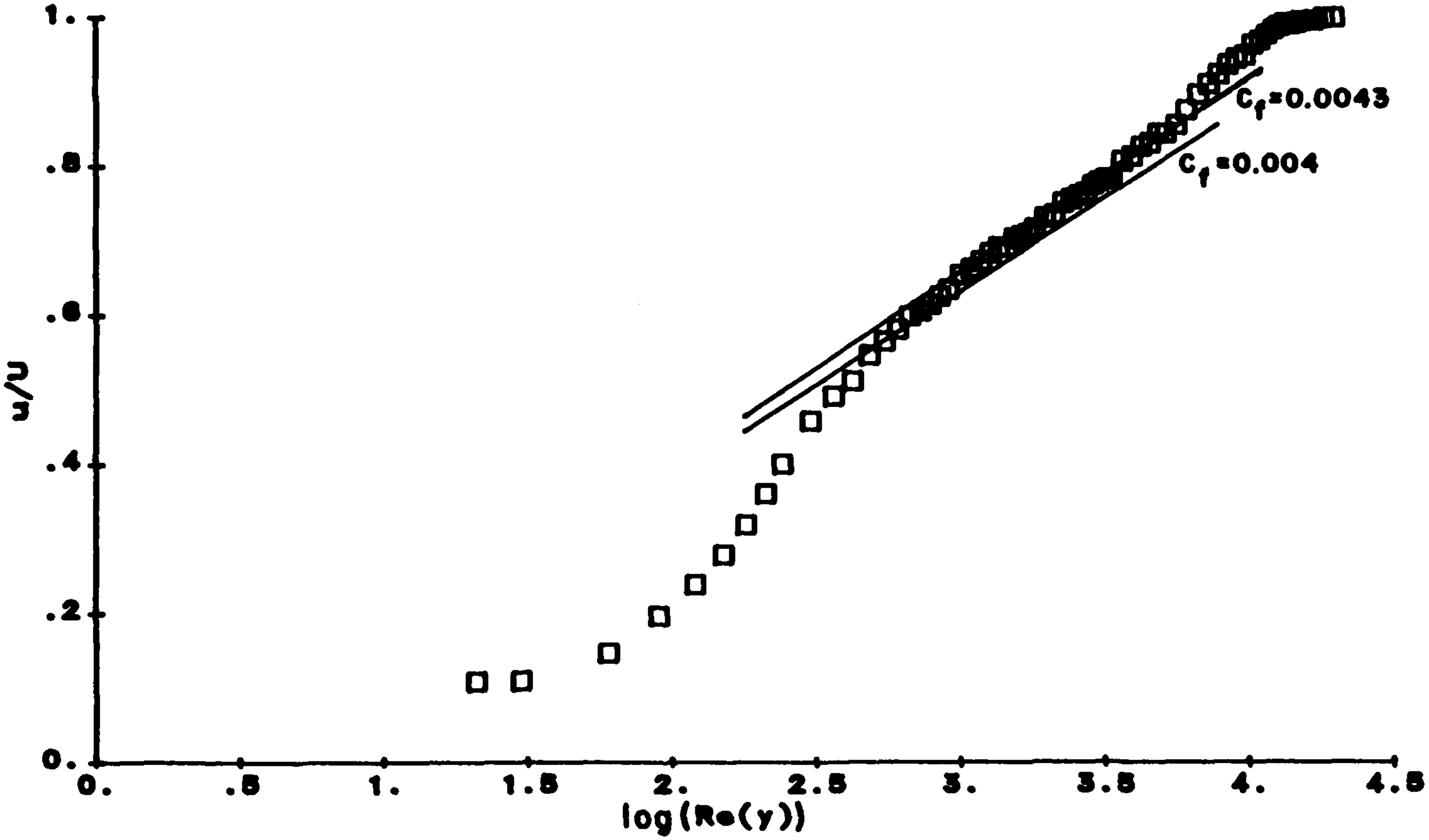

Figure D.5. Law-of-the-wall Clauser cross-plot. Plate-1, Between two lines, $h^+ = 4.3$, $s^+ = 142$, Data file 21, and $Re_\Theta = 1414$.

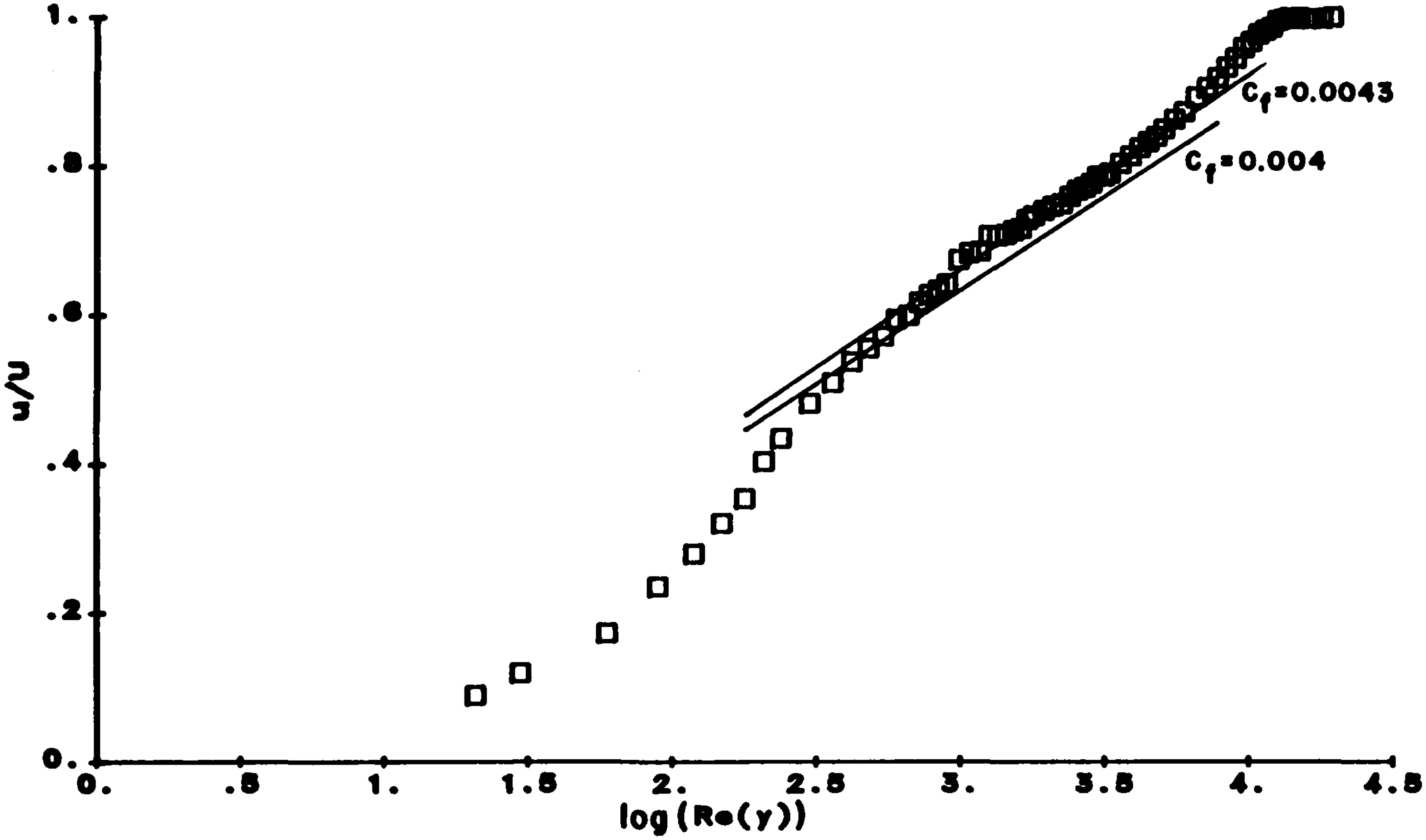

Figure D.6. Law-of-the-wall Clauser cross-plot. Plate-1, Above a line with $y^+ = 0$ referenced to the top of the line, $h^+ = 4.3$, $s^+ = 142$, Data file 22, and $Re_\Theta = 1371$.

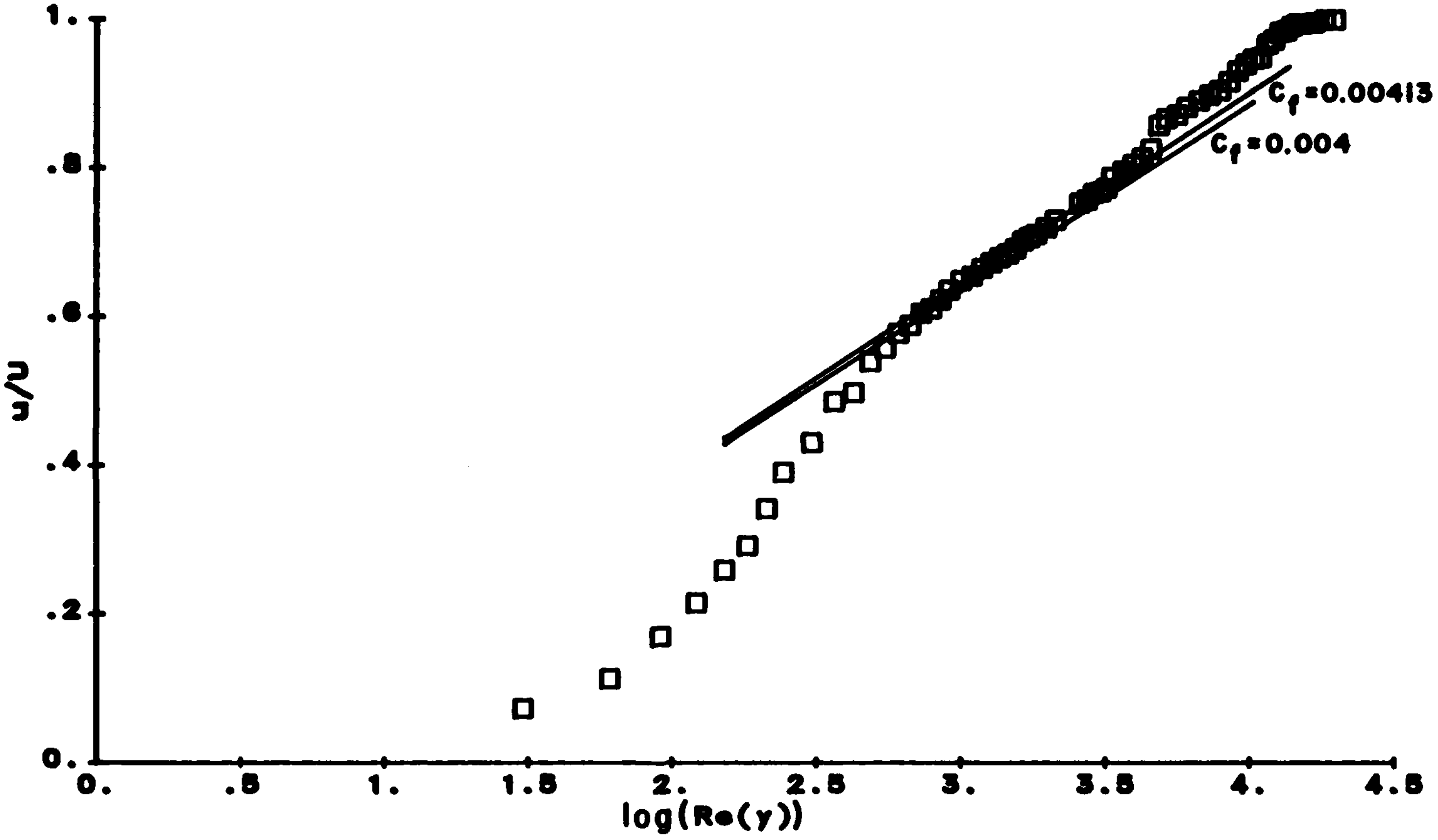

Figure D.7. Law-of-the-wall Clauser cross-plot. Plate-1, Between two lines, $h^+ = 4.3$, $s^+ = 71$, Data file 24, and $Re_\Theta = 1508$.

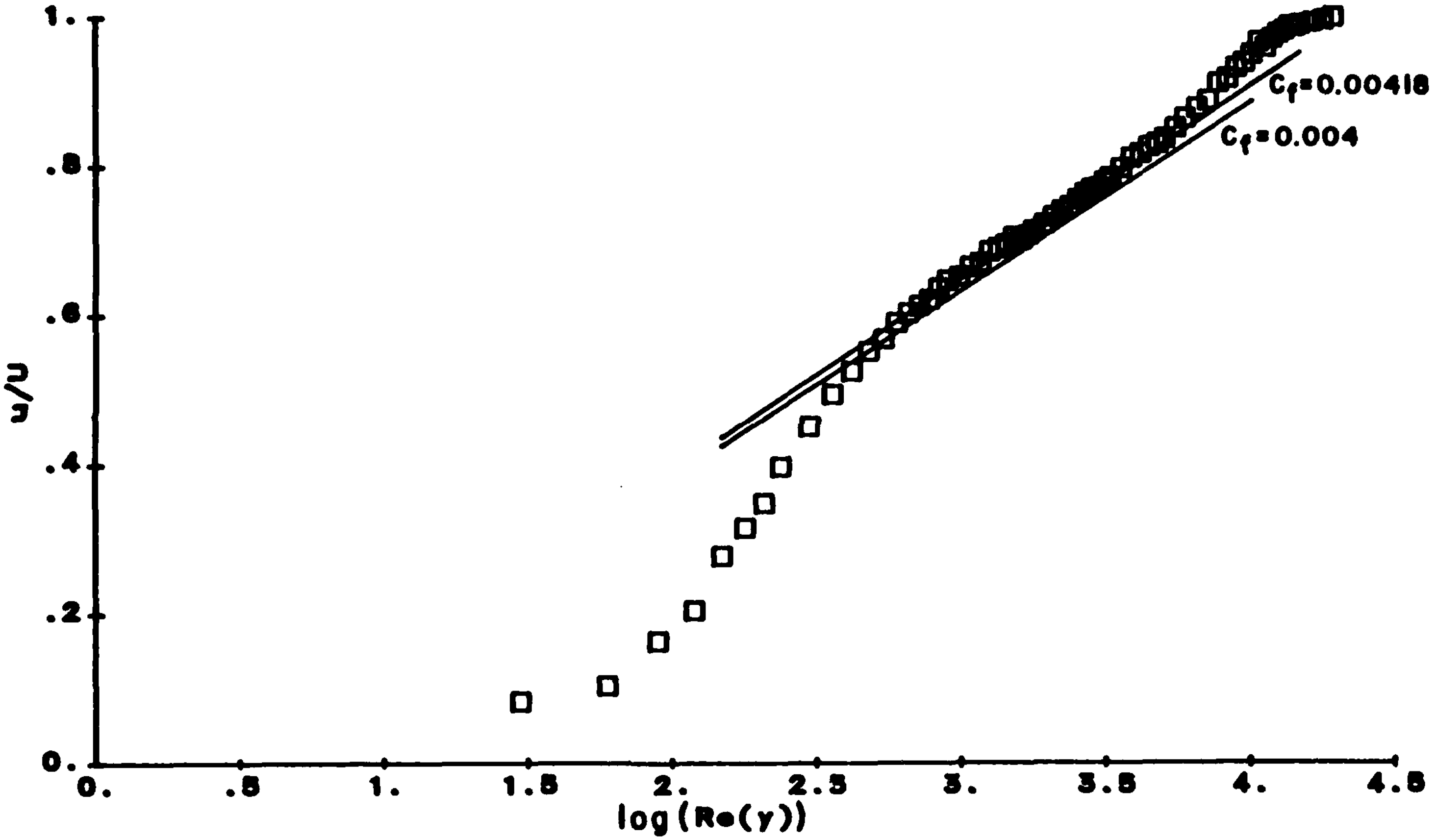

Figure D.8. Law-of-the-wall Clauser cross-plot. Plate-1, Above a line with $y^+ = 0$ referenced to the top of the line, $h^+ = 4.3$, $s^+ = 71$, Data file 25, and $Re_\Theta = 1521$.

APPENDIX E: LAW-OF-THE-WALL PLOTS

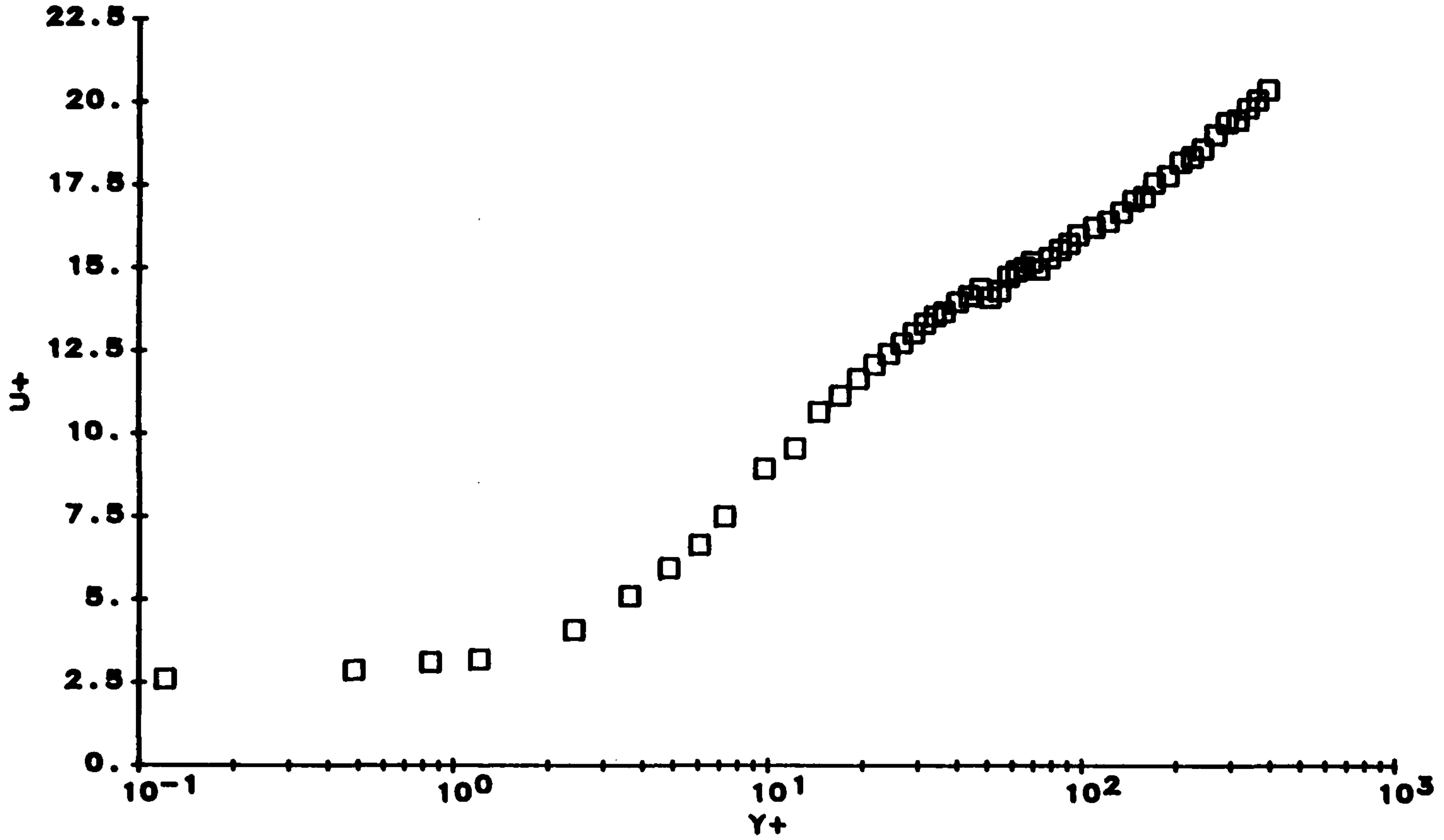

Figure E.1. Law-of-the-wall plot, plate-2. Flat plate upstream of the modified test section. Data file 10, $Re_{\Theta} = 890$.

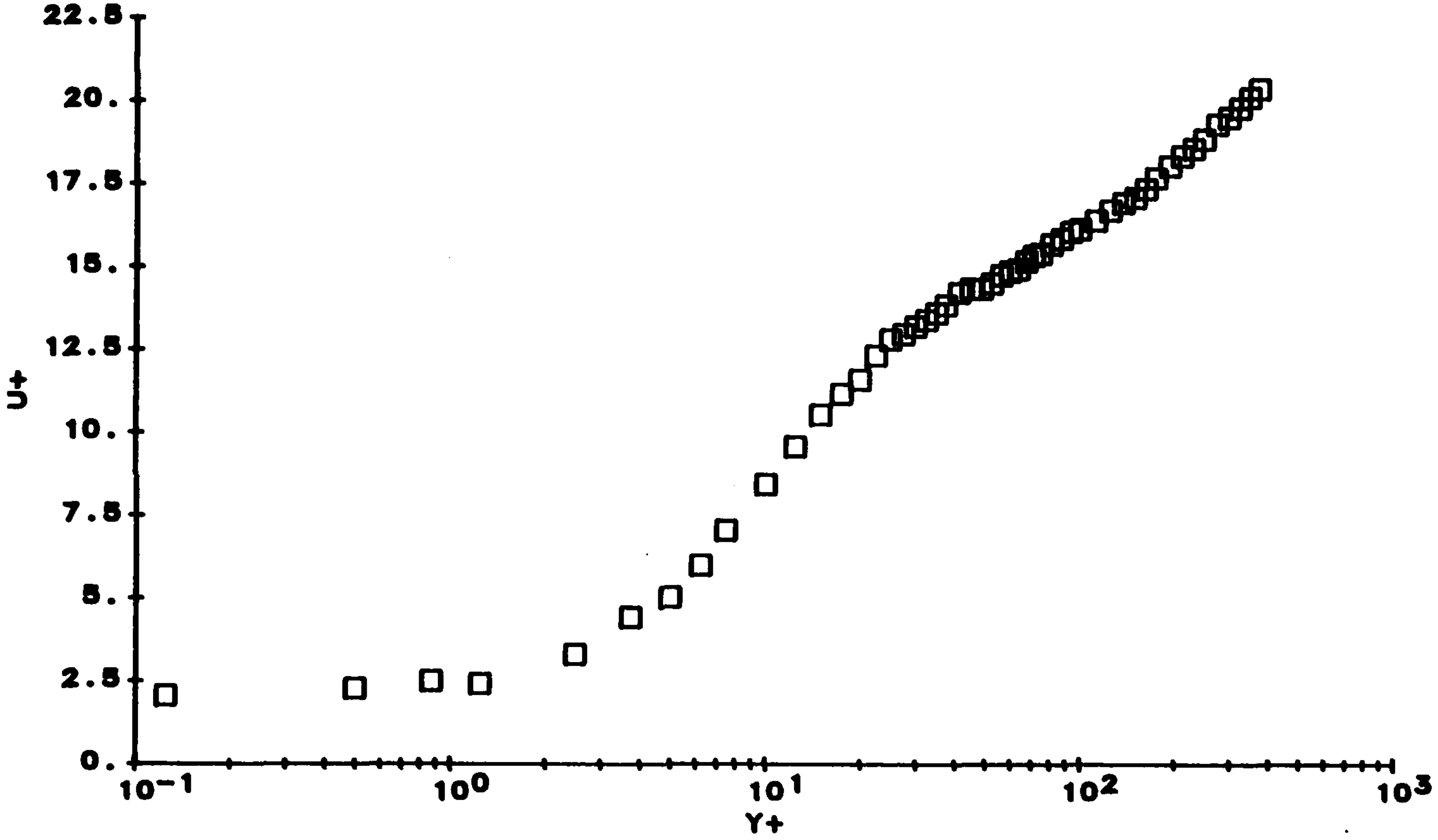

Figure E.2. Law-of-the-wall plot, plate-2. Flat plate, Data file 11, $Re_{\Theta} = 847$.

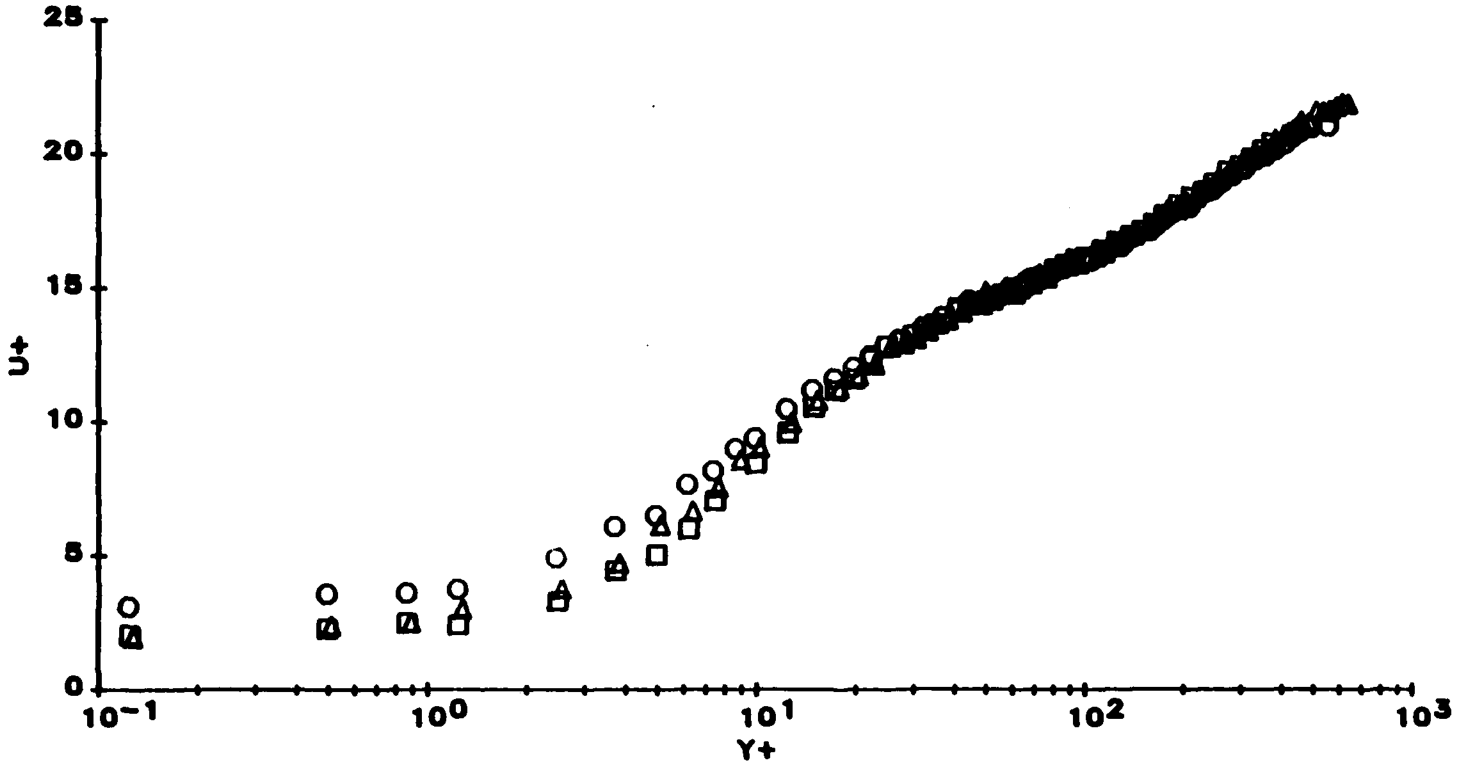

Figure E.3. Law-of-the-wall plot. Plate-2, Flat Plate: □, Data file 11, $Re_\Theta = 847$; ○, Data file 12, $Re_\Theta = 1127$; △, Data file 15, $Re_\Theta = 1399$.

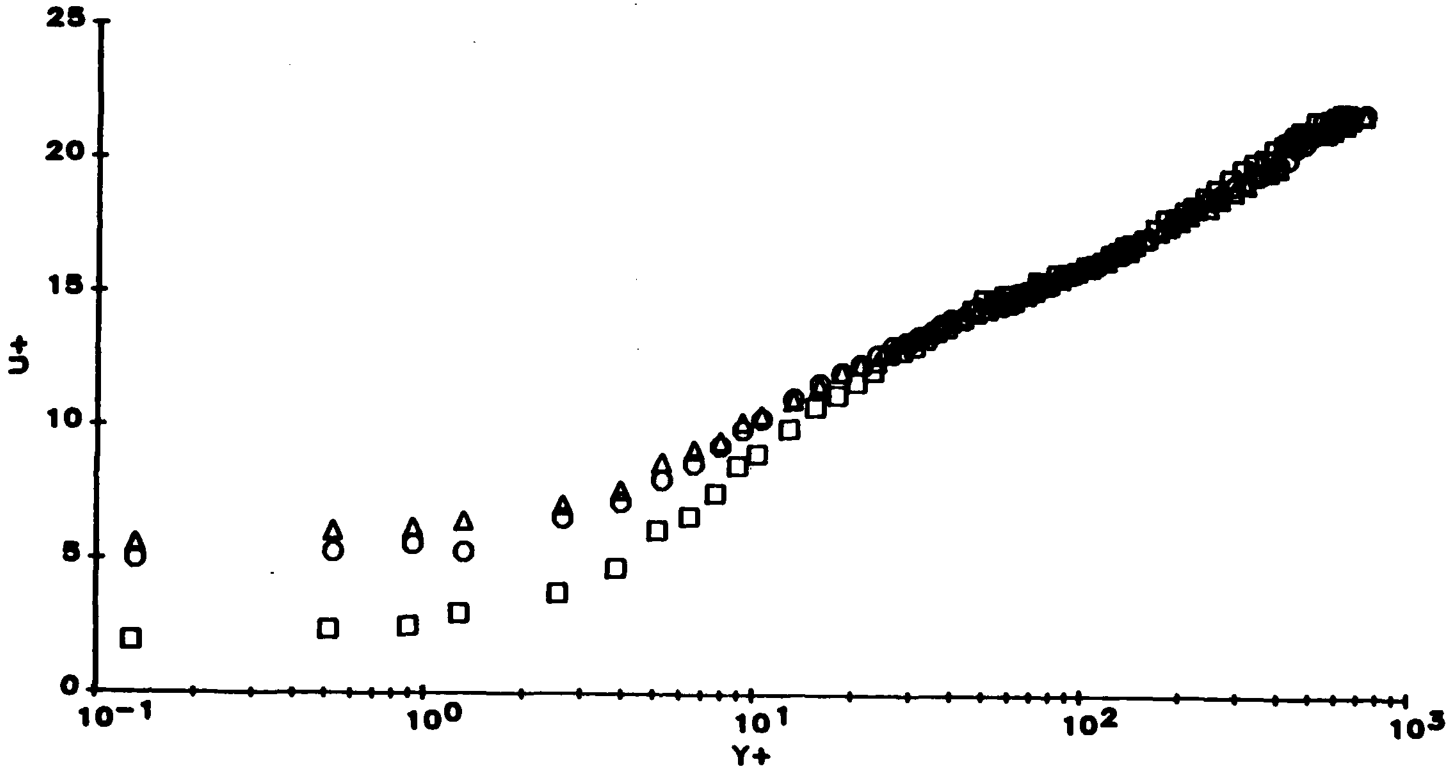

Figure E.4. Law-of-the-wall plot. Plate-2, $h^+ = 3.8$, and $s^+ = 111$: □, Flat plate, Data file 15, $Re_\Theta = 1399$; ○ , Between two lines, Data file 16, $Re_\Theta = 1606$; △ , Above a line with $y^+ = 0$ referenced to the top of the line, Data file 17, $Re_\Theta = 1500$.

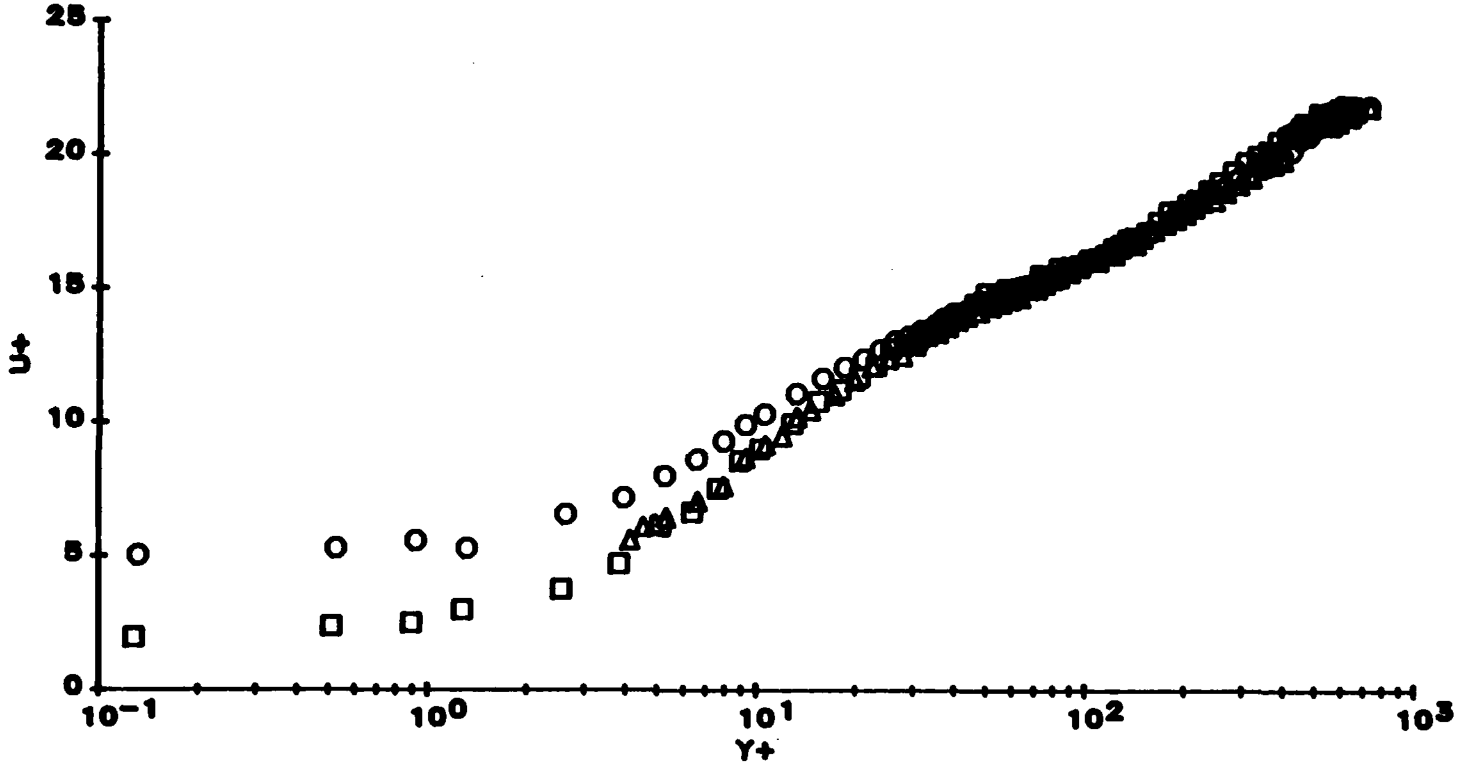

Figure E.5. Law-of-the-wall plot. Plate-2, $h^+ = 3.8$, and $s^+ = 111$: □, Flat plate, Data file 15, $Re_\Theta = 1399$; ○, Between two lines, Data file 16, $Re_\Theta = 1606$; △, Above a line with $y^+ = 0$ referenced to the flat plate, Data file 17, $Re_\Theta = 1500$.

APPENDIX F: TURBULENCE INTENSITY PLOTS

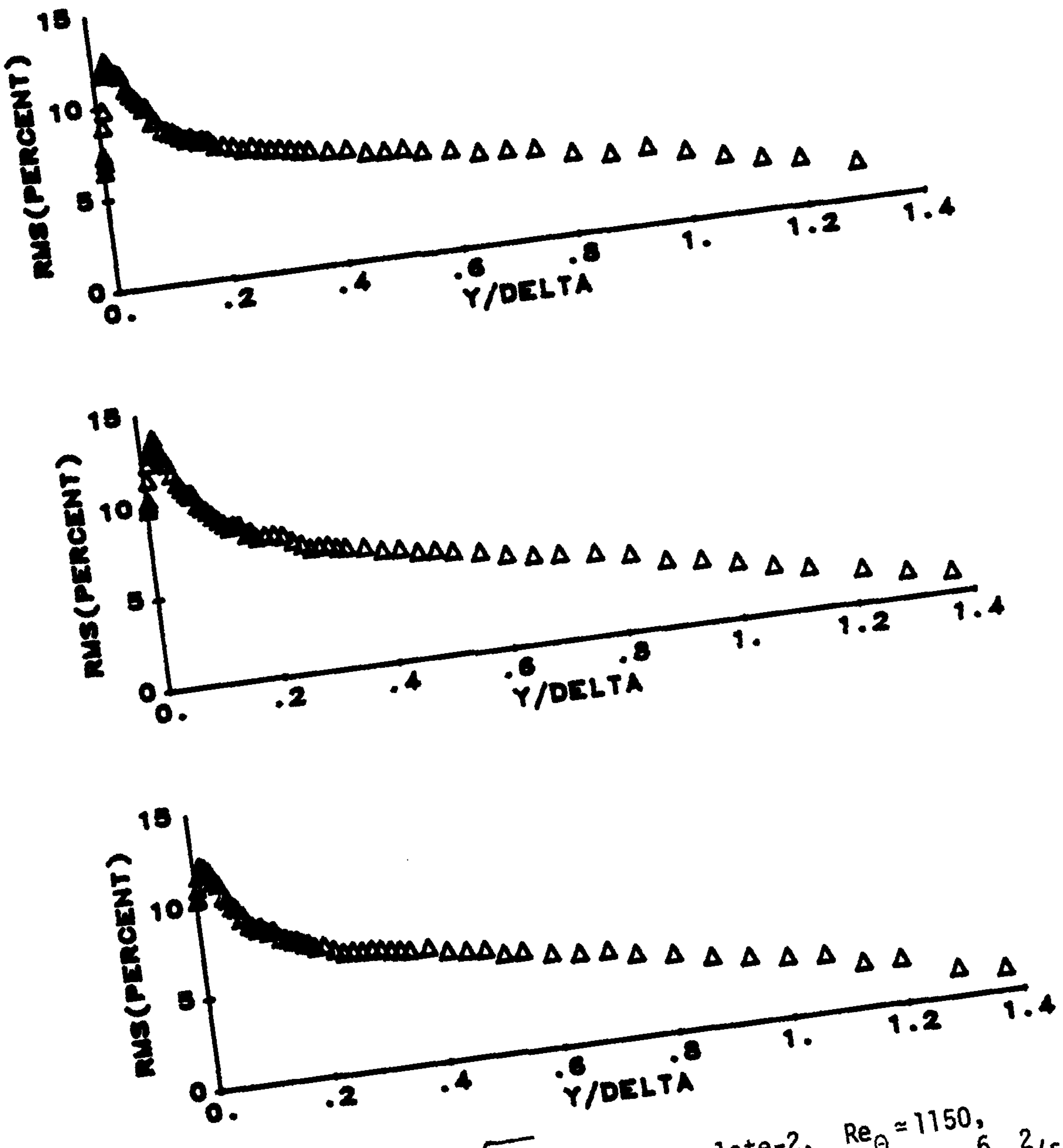

Figure F.1. Plot of $\sqrt{\overline{u'^2}}/U$ vs. y/δ, plate-2. $Re_\Theta \simeq 1150$, $h^+ = 3.8$, $s^+ = 111$, $x = 1.52$m, and $\nu = 0.964 * 10^{-6}$ m^2/s: (TOP), Flat plate; (MIDDLE), Between two lines; (BOTTOM), Above a line with $y^+ = 0$ referenced to the top of the line.

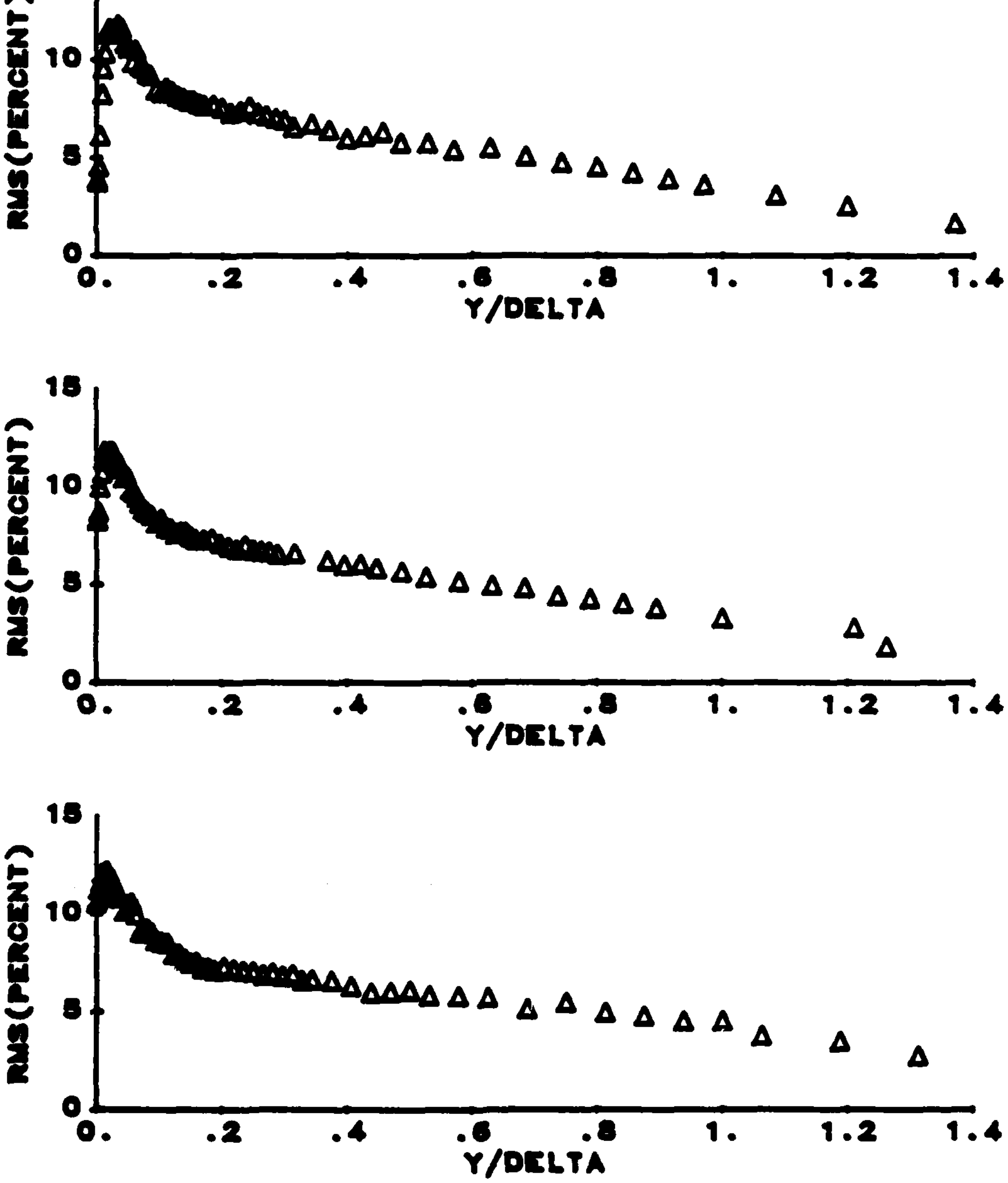

Figure F.2. Plot of $\sqrt{\overline{U'^2}}/U$ vs. y/δ, plate-2, $Re_\Theta \simeq 1550$, $h^+ = 3.8$, $s^+ = 111$, $x = 2.06$m, and $\nu = 0.932*10^{-6}$ m^2/s: (TOP), Flat plate; (MIDDLE), Between two lines; (BOTTOM), Above a line with $y^+ = 0$ referenced to the top of the line.

APPENDIX G: FLOW PARAMETERS AND MEAN STREAK SPACING DATA

Table G.1: Flow Parameters and Mean Streak Spacing From Visualization Studies

Run	x(m)	y^+	h^+	s^+	U(m/s)	$\nu(\frac{m^2}{s})(10^{-6})$	$\overline{\lambda}^+$	Plate
1-101	1.83	4.1	3.9	65	0.24	0.865	80	1
1-102	1.83	10.2	3.9	65	0.24	0.865	106	1
2-015	1.83	5.0	4.7	78	0.30	0.845	78	1
2-016	1.83	10.7	4.7	78	0.30	0.845	81	1
2-064	1.83	4.2	4.0	131	0.26	0.924	118	1
2-065	1.83	10.4	4.0	131	0.26	0.924	134	1
2-086	1.83	4.8	4.6	153	0.30	0.911	133	1
2-087	1.83	10.6	4.6	153	0.30	0.911	121	1

ILME

2 -84